MASTER'S THESIS

DIPLOMARBEIT

Investigation of fluid flow-induced stimulation of osteocytes by means of micromechanics-inspired multiscale modeling

Untersuchung der Stimulation von Osteozyten durch Flüssigkeitsströmung durch Multiskalenmodellierung, basierend auf Prinzipien der Mikromechanik

submitted in satisfaction of the requirements for the degree of
Master of Science
of the Vienna University of Technology – TU Wien, Faculty of Civil Engineering

by

Sarah-Jane ESTERMANN B.Sc.

matriculation number: 1025629

Biomedical Engineering, E 066 453

under the supervision of

Univ. Prof. Dr. techn. Dipl.-Ing. Christian HELLMICH

and

Assistant Prof. Dr. techn. Dipl.-Ing. Stefan SCHEINER

Institute for Mechanics of Materials and Structures (E202)
Karlsplatz 13/202, A-1040 Vienna

Vienna, _____

Abstract

Of all the theories related to the mechanical excitation of cellular activities, the alleged effect of the fluid flow occurring in the lacunar-canalicular pore network on osteocytes is probably the most widely accepted. However, direct experimental verification of the actual occurrence of fluid flow (in response to macroscopically applied mechanical loading of physiologically reasonable magnitude) in these pores has never been obtained.

In this work, a multiscale modeling strategy is presented, inspired by the well-established concept of continuum micromechanics, allowing for upscaling (or homogenization) of the fluid flow contributions in the canalicular, lacunar, and vascular pores in terms of a corresponding macroscopic permeability of bone tissue. The same model also allows for proceeding the opposite way, namely for downscaling macroscopically acting pressure gradients to the pore levels. Thus, physiologically relevant, macroscopic pressure gradients can be related straightforwardly to the correspondingly arising canalicular pressure gradients, and, through considering the resulting pressure gradients in suitable transport laws (as for instance the classical Poiseuille law on the canalicular level), also to related fluid velocities.

When comparing the such computed fluid velocities (for cortical bone) with the fluid velocities that were shown to efficiently excite bone cells *in vitro*, it turns out that the fluid velocities according to the here presented computations are actually much lower. This implies that, based on the multiscale model, pressure-driven fluid flow in the canalicular pores is not likely to be a potent mechanical stimulus for osteocytes (whereas fluid flow in the vascular pores may indeed reach the required fluid velocities and hence excite the therein residing cells). In conclusion, the work presented in this thesis provides important, unprecedented insights as to the observation scale-specific cellular mechanosensation in bone.

Kurzfassung

Unter all den Theorien, die die mechanische Zellstimulation betreffen, ist der vermeintliche Effekt der Flüssigkeitsströmung im Porennetzwerk aus Lakunen und Canaliculi hinsichtlich der Anregung von Osteozyten der in Wissenschaftskreisen oftmals anerkannteste. Es war bisher allerdings nicht möglich, diese Strömungen *in vivo* zu messen und derart die zugrundeliegenden Hypothese zu bestätigen.

In dieser Diplomarbeit wird eine Modellierungsmethode vorgestellt, die dem Multiskalen-Paradigma folgt und auf den Prinzipien der Kontinuumsmikromechanik aufgebaut ist. Dieses Modell erlaubt einerseits die Berechnung (bzw. die Homogenisierung) der entsprechenden makroskopischen Permeabiliät von Knochengewebe, ausgehend von den Beiträgen (die Flüssigkeitsströmung betreffend) der canaliculären, lakunaren und vaskulären Porenräume. Andererseits ermöglicht das Model auch eine umgekehrte Vorgehensweise, d.h. das "Runterskalieren" (oder "Downscaling"), bei dem die Druckgradienten in den Porenräumen berechnet werden, ausgehend von den makroskopisch aufgebrachte Druckgradienten. In weiterer Folge können durch die Berücksichtigung der so ermittelten lokalen Druckgradienten in geeigneten Transportgesetzen (wie z.B. im Flussgesetz nach Poiseuille) die Geschwindigkeiten von Flüssigkeitsströmen in den canaliculären Poren berechnet werden.

Der Vergleich zwischen den so berechneten Flussgeschwindigkeiten (für kortikalen Knochen) und den Geschwindigkeiten, die Knochenzellen *in vitro* stimulieren, zeigt, dass die hier gefundenen Geschwindigkeiten viel zu niedrig sind um Zellen ausreichend zu stimulieren. Daraus folgt, dass, laut dem hier vorgestellten Modell, die Stimulation von Osteozyten durch Flüssigkeitsströmung vermutlich kein effektiver Mechanismus in der Mechanobiologie von Knochengewebe ist (wohingegen die Zellen, welche sich im vaskulären Porenraum befinden, sehr wohl ausreichend schnellen Flüssigkeitsströmen ausgesetzt sind). Folglich liefert die hier präsentierte Arbeit einen entscheidenden Beitrag zur Beleuchtung der zellulären Mechnostimulation auf unterschiedlichen Größenskalen in Knochen.

Acknowledgements

Foremost, I would like to thank my advisor, Stefan, for his dedicated academic guidance and for all the helpful meetings we had, which enabled the realization of this thesis.

I would like to thank all my friends, who accompanied me during the years of studying, for all the fun times we had together and will have in the future. Especially, I would like to thank Johanna and Chrissi for their never-ending friendship and for always believing in me, and also many thanks to Rubén for all his support.

Most of all, I would like to thank my parents, Sally and Rudolf, and my sister, Amy, for their endless encouragement and love throughout my whole life. Without their support this accomplishment would never have been possible. I am so grateful for having you as my family.

Contents

1. Background and motivation

1.1. Bone growth, metabolism, and adaptation

Bones are composed of a constantly evolving tissue, undergoing continuous renewal, or even geometrical change. The underlying processes occur at specific sites selectively, the most important of which are growth, metabolism, and adaptation:

- Bone growth is the process leading to lengthening and widening of bones, predominantly during adolescence. Lengthening is achieved by ossification of hyaline cartilage at the epiphyseal plate, while increase of diameter is caused by appositional growth; notably, the latter mechanism can continue after the lengthening is already completed (Kronenberg, 2003). The thickening of a bone organ entails a reduction of tissue adjacent to the medullary cavity, combined with a material increase beneath the periosteum (Parfitt et al., 2000).

- Bone remodeling, comprising the removal (or resorption) of bone tissue and the subsequent deposition of new tissue (often referred to as bone formation) to "refill" the cavities resulting from resorption, allows for the compositional optimization in response to the prescribed mechanical loading (in terms of microstructural adaptations), calcium homeostasis, and the repair of microscopically sized cracks that are caused by local overloading (Clarke, 2008; Bilezikian et al., 2002). The well-coordinated sequence of resorption and formation is organized in form of so-called basic multicellular units (BMUs), as was first suggested by Frost and Thomas (1963). In healthy bone, the net balance between resorption and formation is in equilibrium for each BMU, but can be positive or negative in case of metabolic diseases, such as osteoporosis (Raisz, 2005), osteomalacia (Frame and Parfitt, 1978), or hyperparathyroidism (Fraser, 2009). Also atypical mechanical loading conditions are known to steer bone remodeling towards bone gain or loss. For example, during prolonged phases of disuse loading, as it may occur due to bedrest or microgravity conditions during spaceflight (Mack and Lachance, 1967; LeBlanc et al.,

2007), resorption is increased and formation remains unchanged or decreases leading to a loss of bone mass (Robling et al., 2006), accompanied by a decrease of calcium absorption in the bone and thus higher urinary calcium excretion values (Smith et al., 2005).

- Bone modeling (not to be confused with *re*modeling) is the process leading to adaptation of the actual shape, and of the distribution of cortical and trabecular compartments of bony organs, caused by certain diseases, such as Paget's disease of the bone (Roodman and Windle, 2005), or long-ranging changes of the mechanical loading; the latter may be related to changes of physical activities, weight gain, or growth during adolescence (Robling et al., 2006). Modeling is based on formation and resorption processes, occurring isolated from each other (unlike bone remodeling). The involved biochemical and biomechanical regulatory pathways are believed to be very similar between bone modeling and remodeling, while revealing the exact differences between the two mechanisms is thus far an unresolved scientific question (Dunlop et al., 2009).

Osteoclasts, osteoblasts and osteocytes are the cells which are essentially responsible for all of these processes. Osteoclasts (deriving from hematopoietic stem cells) resorb bone,[1] while osteoblasts (deriving from mesenchymal stem cells) produce bone matrix.[2] The differentiation behaviors of osteoclasts and osteoblasts are closely linked with each other: The maturation (along various steps of differentiation) of osteoclasts from their precursor cells requires the binding of the receptor activator of nuclear factor kappa-light-chain-enhancer of activated B cells (RANK), which is a surface-bound receptor on osteoclasts, to the RANK ligand (RANKL), which is expressed by cells of the osteoblastic linage (Takahashi et al., 1988). Furthermore, osteoprotegerin (OPG), also expressed by osteoblasts, acts as a decoy receptor, occupying RANKL and thus inhibiting osteoclastogenesis (Wan et al., 2001). The presence of the parathyroid hormone (PTH) has been shown to increase bone turnover (Parfitt, 1976), by modulating the expression of both RANKL and OPG (Huang et al., 2004). Additionally, the resorptive activity of osteoclasts leads

[1] First, osteoclasts firmly attach to the bone surface, forming a sealed interface between the cell and the bone material. Then, the *p*H at the interface is strongly reduced by activation of proton pumps in the cell membrane, which transport protons into the bone surface area. Thus, the bone mineral becomes soluable due to the acidic environment. Furthermore, the organic matrix is degraded through secretion of acid proteases by the osteoclasts (Buckwalter et al., 1995).

[2] In more detail, osteoblasts excrete osteoid, consisting mainly of collagen type I, which gets increasingly mineralized over time, with the compound of soft collagen, hard (hydroxyapatite-type) mineral, as well as pore spaces in-between, denoted as bone matrix. Since this mineralization process occurs very fast initially, osteoblasts are, for simplicity, often referred to as bone-forming cells, thus withholding the intermediate step of osteoid formation (Marie, 1998).

to the release of transforming growth factor beta (TGFβ), which is otherwise stored in the bone matrix, in turn regulating the differentiation behavior of osteoblasts (Bonewald and Mundy, 1990). The most abundant cells in bone are the mechanosensitive and signal-transmitting osteocytes (Bonewald, 2011), evolving from osteoblasts that become trapped in the bone matrix during the bone formation process (Robling et al., 2006). They reside in the lacunar pores and their cell processes extend into the canalicular tunnels that are interconnected and protrude from the lacunar pores in vast numbers. Estimates based on focused ion beam and scanning electron microscopy (Schneider et al., 2011), light microscopy (Beno et al., 2006), and confocal laser scanning microscopy (Sugawara et al., 2011, 2005; Sharma et al., 2012) conclude that there might be 50 to 85 canaliculi per lacuna. The osteocytic cell processes have been suggested to be the most mechanosensitive parts of the osteocyte, based on calcium fluorescence imaging, which allows for identifying the location within the cell of the highest intracellular Ca^{2+} response (Thi et al., 2013).

In addition to the aforementioned three kinds of cells (i.e. osteoblasts, osteoclasts and osteocytes), the so-called bone lining cells cover quiescent (non-remodeling) surfaces of the bone, and communicate with each other via gap junctions (Miller et al., 1989), while also being connected to the osteocytic network through processes extending into the canaliculi. Bone lining cells serve as a barrier between blood and bone, regulating the mineral ion uptake and discharge into and out of the bone extracellular fluid (Clarke, 2008). They evolve from osteoblasts, deposited at the surface during remodeling processes, and can return to their osteoblastic state, due to mechanical forces or PTH exposure (Dobnig and Turner, 1995).

1.2. Mechanosensitivity of the osteocyte

In the following, the exact response of osteocytes to mechanical loading is reviewed. The elevation of the intracellular calcium concentration is one of the indicators of cell activity upon stimulation by mechanical loading. In the cell's unloaded state, the intracellular calcium concentration is lower than the concentration in the extracellular environment, enabled by active ion pumps that expel calcium-ions from the cell. When a cell is mechanically stimulated, Ca^{2+}-ions enter the cell's cytoplasm through channels that are supposedly activated by loading, as well as being released from reservoirs within the cell. *In vitro* fluid flow stimulates the production of inositol triphosphate, which triggers the release of Ca^{2+} from intracellular stores (Ajubi et al., 1999; Nollert et al., 1990). This elevation of the intracellular calcium concentration allows the production of prostaglandins, especially

prostaglandin E_2 (PGE_2), due to the increased expression of the cyclooxygenase, COX-2, an enzyme crucial for the PGE_2 production. There are many factors that increase the expression of COX-2 in bone cells, including mechanical loading and calcium (Ajubi et al., 1999; Pilbeam et al., 2008). PGE_2 plays an important role in bone remodeling, acting as a promoter as well as an inhibitor of bone formation (Pilbeam et al., 2008). Due to PGE_2's influence on RANK/OPG-signaling it acts as an osteoclastogenesis-promoting agent: Influenced by PGE_2, the expression of RANKL on osteoblasts and osteoblastic precursor cells is increased, hence promoting the binding of RANKL to its receptor RANK, located on osteoclast precursors, which is a prerequisite for osteoclast maturation (Robling et al., 2006; Pilbeam et al., 2008). Furthermore, PGE_2 may also suppress the expression of OPG (Suda et al., 2004). In this context, PGE_2 may be seen as a bone resorption inducing agent, through the positive influence it has on the differentiation of osteoclasts. On the other hand, PGE_2 signaling plays a role in the Wnt/β-catenin pathway, also called the canonical pathway, through crosstalk (Kamel et al., 2006), which ultimately promotes bone formation (Pilbeam et al., 2008). The wingless gene, standardly referred to as Wnt, is a glycoprotein modified with a lipid, and is also secreted from the cells as a response to mechanical loading, which initiates the Wnt/β-catenin pathway by binding to transmembrane proteins of osteocytes and osteoblasts and causing β-catenin accumulation in the cytoplasm, which subsequently translocates to the nucleus to affect gene transcription there, encouraging new bone formation (Bonewald and Johnson, 2008). Another marker of the osteocytes' anabolic response to mechanical loading is the release of nitric oxide (NO) by osteocytes, but also osteoblasts, within seconds after loading (Bakker et al., 2001). NO is a free radical that has many functions in cell biology, for example acting as a neurotransmitter and a vasodilator (Turner et al., 1997). *In vivo* studies on bone cells show that NO behaves as an osteoblast activity-encouraging agent; blocking the production of NO subsequently leads to a drastic decrease in new bone formation (Turner et al., 1997; Fox and Chow, 1998).

While there is ample evidence for the mechanosensitivity of the osteocyte (as briefly summarized in the previous paragraph), the exact nature of the triggering mechanical stimuli is not clear to date. Proposed types of loading, sensed and translated into chemical signals by osteocytes, in order to control osteoblast and osteoclast activities, include fluid pressures acting onto osteocytes[3] (Liu et al., 2010; Klein–Nulend et al., 1995b; Nagatomi et al., 2001, 2003), direct deformation of the cell body through bone matrix strains (Nicolella et al., 2005), microdamage (Hazenberg et al., 2006), piezoelectric effects (Bas-

[3]Not only osteocytes, but apparently any type of biological cells change their behavior when sensing pressure variations (Imamura et al., 1990; Nagatomi et al., 2002; Kaarniranta et al., 2003).

sett, 1968), streaming potentials (Pienkowski and Pollack, 1983), and fluid flow-induced shear forces acting on the cell membrane (Klein–Nulend et al., 1995c; Riddle and Donahue, 2009). Remarkably, ever since the latter mechanism has been suggested in the late 1980s (Frangos et al., 1988; Klein–Nulend et al., 1995c; Frangos and Johnson, 1995), the scientific community has readily embraced this idea; fluid flow has been used as the preferred stimulus for studying the mechanosensitivity of osteocytes *in vitro* (You et al., 2000; Bonewald, 2006; Fritton and Weinbaum, 2009), leading to a substantial amount of respective experimental data.

1.3. Experimental difficulties

Direct experimental confirmation of the aforementioned "fluid flow-hypothesis" is still missing, despite the enormous efforts that have been undertaken in this respect. The reasons for this deficit are related to the various length scale-related intricacies of the processes under scrutiny. In particular, with the nowadays available experimental methods it is impossible to directly measure the flow of the fluid contained in the lacunar and canalicular pores in response to physiological macroscopic loading. As a remedy, the following types of experiments have been carried out:

- ***In vitro* tests:**

  Cells are exposed to a linear flow in a parallel plate flow channel (Genetos et al., 2005; Bakker et al., 2003; Klein–Nulend et al., 1995a; Haut Donahue et al., 2003; Kreke et al., 2005; Jacobs et al., 1998). This setup was first described by Frangos et al. (1988), for exposing all kinds of mammalian cells to steady and pulsatile shear stresses, in order to quantify their metabolic response. The cells are cultured on a rectangular glass slide, and exposed to a laminar flow after making sure that the cells are well attached to the surface, and can be observed throughout the experiment with microscopic methods, predominantly utilizing fluorescence microscopy combined with calcium imaging(Klein–Nulend et al., 1995b; Frangos et al., 1988). However, the osteocytes are placed in a very artificial environment in these tests, which is actually quite different to the small pore spaces they would natively inhabit. It is also questionable whether the flow conditions that are applied in the chambers actually resemble the conditions *in vivo*.

- **Bioreactor tests:**

  Efforts to more realistically replicate the cell's environment have led to the development of perfusion bioreactors, where the cells are cultured in 3D scaffolds (e.g. titanium mesh, or scaffolds made out of ceramic, silk fibroin, gelatin, or hydroxyapatite), thus experiencing a fluid flow within the pore spaces of the scaffold due to the applied pressure gradients (Bancroft et al., 2002; Li et al., 2009; Sinlapabodin et al., 2016). However, it is impossible to properly separate the various stimuli that may occur; cells supposedly react to fluid shear stress, to hydraulic pressures, to matrix strains, or to combinations thereof.

- **Tracer tests:**

  Knothe Tate and Knothe (2000) were the first to propose an experiment where fluorescent tracer molecules are first injected into a bone specimen and then bone cross-sections of the latter are histologically evaluated, predominantly utilizing fluorescence recovery after photobleaching (FRAP) microscopy, while the bone specimens can optionally be subjected to mechanical loading. Modeling approaches, based on the FRAP results, have been implemented in order to estimate the matrix permeability and the fluid velocity caused by loading. While this semi-experimental modality has been repeated many times, see e.g. (Wang et al., 2005; Price et al., 2011; Zhou et al., 2008; Kwon and Frangos, 2010; Kwon et al., 2012), it is however not clear if and how tracer transport by convection can be separated from diffusional transport.

1.4. Objectives and structure of this thesis

The main objective of this work is to develop a mathematical model capable of establishing the (experimentally not available) bridge between two kinds of data, namely the physiological macroscopic loading to which bone is exposed, on the one hand, and the corresponding fluid flow velocities that can be expected to occur in the canalicular pores of bone, on the other hand. The concept of continuum micromechanics is utilized, which has proven to be an adequate modeling concept for hierarchically organized materials. The such computed fluid velocities are then compared to fluid velocities that have been shown to stimulate osteocytes *in vitro*. Thus, the plausibility of the fluid flow-hypothesis can be assessed in quantitative terms, for the first time based on a modeling approach rigorously considering the multiscale paradigm.

Accordingly, the structure of this thesis is as follows: First, the hierarchical organization of bone is thoroughly elucidated (see Section 2.1), based on which a suitable model representation of bone tissue is deduced (see Sections 2.2 and 2.3). Then, a continuum micromechanics-inspired model is developed, allowing for estimating the upscaled permeability of bone tissue from the local permeabilities related to the representative fluid flow conditions in the pore spaces of bone, on the one hand, and for downscaling of pressure gradients from the macro- to the microscale, on the other hand (see Section 3). Numerical studies demonstrate how the aforementioned local permeabilities translate into corresponding macroscopic ones (see Section 4.1), as well as to which extent macroscopic pressure gradients are "felt" in the canalicular pores (see Section 4.2). Based on considering typical macroscopic loading to which long bones are subjected (see Section 5.1), the model is employed to estimate the corresponding pore-scale fluid velocities (see Section 5.2). The results are subsequently compared to the related experimental data (see Section 5.3), and respective conclusions are drawn (see Section 6).

2. Multiscale modeling of bone tissue

2.1. Hierachical organization of bone

Bone is a hierarchically built-up material, made largely out of collagen, hydroxyapatite matrix, and water, and also contains bone marrow, cells, and non-collagenous proteins. Two different types of bony structures can be identified in bone organs: The dense and compact cortical bone often forming the shell of bone organs, and the more loosely packed and highly porous trabecular or cancellous bone (Gray, 1918), as seen in Figure 2.1a. Cancellous bone lines the walls of the medullary cavity, where the bone marrow is stored, and has a high surface area due to its inter-trabecular porosity of about 50 – 90% (Padilla et al., 2008). Cortical bone, on the other hand, is less porous, with a vascular porosity of a few percent in young adults (Feik et al., 1997; Stein et al., 1999; Bousson et al., 2000), see Table 2.1, potentially increasing up to 35% in old age (Cooper et al., 2007). Figure 2.1b shows the bone cortex shell and the loosely packed trabecular bone on the inside, with their microstructures clearly visible with higher magnifications in Figures 2.1c and 2.1d. Vascular pores, as the name already implies, host blood vessels in a branched structure, the main larger branches being aligned along the bone axis called Haversian canals and the smaller Volkmann canals, being more or less perpendicular to the Haversian canals (Cooper et al., 2003) (experimentally obtained vascular diameters can be seen in Table 2.2). The next smaller porosity is the lacunar porosity (as seen in Figures 2.1e and 2.1f), hosting the osteocytic cell bodies which are depicted in Figures 2.1g and 2.1h, also showing their cell processes. The lacunar porosity lies within a range of 1.5 – 10% (Schneider et al., 2007; Tommasini et al., 2012; Tai et al., 2008; Benalla et al., 2013), see Table 2.3, and the diameter of these ellipsoidal lacunar pores amounts to a few microns[4] (Palacio–Mancheno et al., 2014; Sugawara et al., 2005), see Table 2.4, and The even smaller, cylindrically shaped canaliculi, forming an extensive network, hence connecting the la-

[4] "Microns" is a length measurement frequently used in bone-related literature; with one micron being equal to 10^{-6} m.

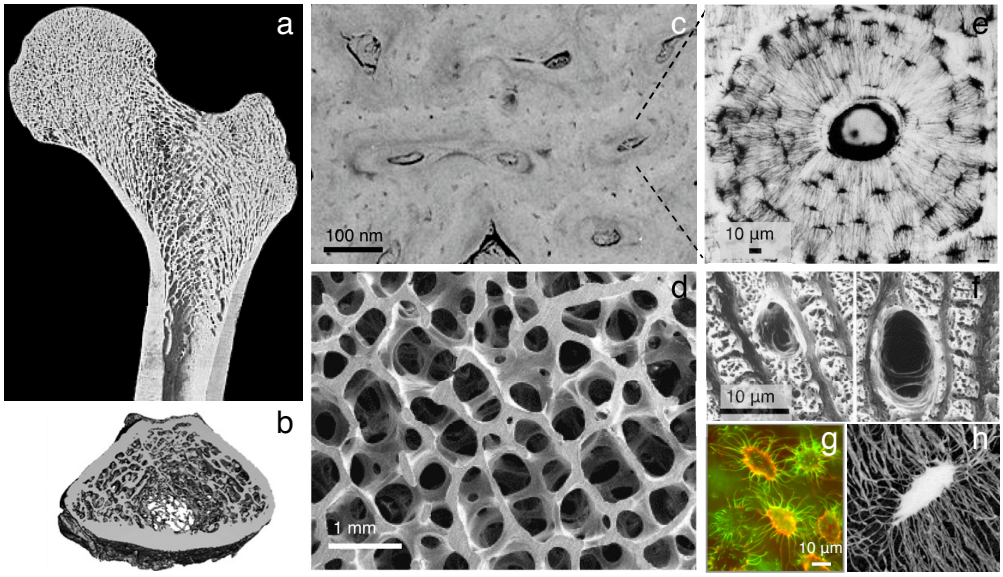

Figure 2.1.: Hierarchical structure of bone: **a** Longitudinal section of a human femur, showing dense and loosely packed bone (Daxner et al., 2000); **b** Transverse section of a distal rat femur, reconstructed from µ-CT images with trabecular bone in the center and cortical bone at the edges (Campbell and Sophocleous, 2014); **c** SEM image of a cross-section of cortical bone, showing single osteons with Haversian canals and lacunar pores (small black dots) (Ambekar et al., 2012); **d** SEM image of trabecular structure with single trabeculae and bone-marrow filled cavities in between (Fantner et al., 2006); **e** Light microscopy of a single osteon with its central Haversian canal, and lacuanae, connected via canaliculi, arranged in lamellae around the Haversian canal (Ardizzoni, 2001); **f** SEM image of single lacunar pores, wedged in the lamellae (Ardizzoni, 2001); **g** Fluorescence image of an osteocyte network with dendritic processes (Kamel–ElSayed et al., 2015); **h** Single osteocyte with processes, taken (Hesse et al., 2015)

cunae with each other, are a few hundred nanometers (i.e. 10^{-9} m) in diameter (Marotti, 1990; You et al., 2004; Lin and Xu, 2011), see Table 2.5, and exhibit a volume fraction of around 1 – 3% (Schneider et al., 2011; Hesse et al., 2015; Benalla et al., 2013), see Table 2.6.

At even lower observation scales, further types of pore spaces can be discerned, namely the space between the hydroxyapatite crystals (together forming the so-called extrafibrillar space), and the intramolecular pore space found between collagen molecules, see e.g. (Weiner and Wagner, 1998; Katz et al., 1984; Fritsch and Hellmich, 2007; Fritsch et al., 2009). Both intercrystalline and intermolecular pore spaces are however irrelevant for the work presented in this thesis, and are hence neglected subsequently.

Table 2.1.: Overview of the experimentally obtained vascular porosities f_{vas}; VM standing for virtual microscopy, CT+μRG standing for computed tomography and micro-radiography, SR-μCT standing for synchrotron radiation micro-computed tomography, and μCT standing for micro-computed tomography

Reference	f_{vas} [-]	Tissue	Method
Feik et al. (1997)	0.07	Human femur, male/female	Digitalized VM
Stein et al. (1999)	0.059	Human femur	Digitalized VM
Bousson et al. (2000)	0.09	Human mid-diaphysis femur, female	CT+μRG
Bousson et al. (2000)	0.08	Human mid-diaphysis femur, male	CT+μRG
Bousson et al. (2001)	0.09	Human mid-diaphysis femur, female	CT+μRG
Bousson et al. (2001)	0.08	Human mid-diaphysis femur, male	CT+μRG
Palacio–Mancheno et al. (2014)	0.048 0.013–0.023	Rat tibial mid-diaphysis Rat tibial mid-diaphysis	μCT μCT
Schneider et al. (2009)	0.0122±0.0026	Mouse (B6) mid-diaphysis	SR-μCT
Schneider et al. (2007)	0.048±0.015	Mouse (C3/B6) femoral mid-diaphysis	SR-μCT
Schneider et al. (2007)	0.018±0.006	Mouse (B6) femoral mid-diaphysis	SR-μCT
Cooper et al. (2007)	0.0729±0.069	Human femur	μCT
Cooper et al. (2003)	0.06	Human femur	μCT+μRG
Renders et al. (2007)	0.0353±0.012	Human mandibular condyle	μCT

Table 2.2.: Overview of the experimentally obtained vascular pore diameters d_{vas}; µCT standing for micro-computed tomography, applied at different resolutions, and pQCT standing for peripheral quantitative computed tomography

Reference	d_{vas} [µm]	Tissue	Method
Palacio–Mancheno et al. (2014)	14.7	Rat tibia mid-diaphysis	µCT (res. 1 µm)
Palacio–Mancheno et al. (2014)	9.38±0.35	Rat tibia mid-diaphysis	µCT (res. 4 µm)
Schneider et al. (2007)	10.3	Mouse femoral mid-diaphysis	µCT (res. 3.7 µm)
Renders et al. (2007)	53±5 48±7	Human mandibular condyle	µCT
Goulet et al. (2008)	35.6 – 79.6	Human tibia	pQCT
Martin et al. (1998)	40 – 50	Human cortical bone	µCT

Table 2.3.: Overview of the experimentally obtained lacunar porosities f_{lac}; SR-nCT standing for synchrotron radiation nano-computed tomography, and µCT standing for micro-computed tomography

Reference	f_{lac} [-]	Tissue	Method
Schneider et al. (2007)	0.013	Mouse (B6) femoral mid-diaphysis	SR-µCT
Tommasini et al. (2012)	0.015	Rat femoral diaphysis	SR-µCT
Benalla et al. (2013)	0.0169±0.005	Human mid-diaphysis femur	µCT
Hesse et al. (2014a)	0.008±0.003	Human jaw	SR-µCT
Hesse et al. (2014b)	0.013±0.007	Human jaw	SR-µCT
Palacio–Mancheno et al. (2014)	0.015±0.0044	Rat tibial mid-diaphysis	µCT
Tai et al. (2008)	0.09	Mouse fore limbs	µCT

Table 2.4.: Overview of the experimentally obtained lacunar pore diameters d_{lac}; CLSM standing for confocal laser scanning microscopy, and AFM standing for atomic force microscopy

Reference	d_{lac} [µm]	Tissue	Method
Sugawara et al. (2005)	2 – 5	Chick calvaria	CLSM
Lin and Xu (2011)	3.86±1.02	Bovine tibia, transverse direction	AFM
Lin and Xu (2011)	5.37±1.7	Bovine tibia, radial direction	AFM
Vatsa et al. (2008)	7.6±1.15	Mouse (B6) fibula	CLSM

Table 2.5.: Overview of the experimentally obtained canalicular pore diameters d_{can}; SEM standing for scanning electron microscopy, TEM standing for transmission electron microscopy, CLSM standing for confocal laser scanning microscopy, AFM standing for atomic force microscopy, and FIB/SEM standing for focused ion beam scanning electron microscopy

Reference	d_{can} [µm]	Tissue	Method
Marotti (1990)	150–550	Human tibia	SEM
You et al. (2004)	259±129	Mouse female	TEM
Sugawara et al. (2005)	<500	Chick calvaria	CLSM
Lin and Xu (2011)	426±118	Bovine tibia, transverse direction	AFM
Lin and Xu (2011)	459±144	Bovine tibia, radial direction	AFM
Lin and Xu (2011)	419±113	Bovine tibia, longitudinal direction	AFM
Schneider et al. (2011)	95	Mouse (B6) femoral mid-diaphyis	FIB/SEM
Sharma et al. (2012)	520±42	Rat tibia, cortical metaphysis, trabecular remnants	CLSM
Sharma et al. (2012)	553±33	Rat tibia, cortical metaphysis, lamellar region	CLSM

Table 2.6.: Overview of the experimentally obtained canalicular porosities f_{can}; FIB/SEM standing for focused ion beam scanning electron microscopy, SR-nCT standing for synchrotron radiation nano-computed tomography, and µCT standing for micro-computed tomography

Reference	f_{can} [-]	Tissue	Method
Schneider et al. (2011)	0.007	Mouse (B6) femoral mid-diaphysis	FIB/SEM
Hesse et al. (2015)	0.02±0.008	Human jaw	SR-nCT
Benalla et al. (2013)	0.0279±0.0091	Human femoral diaphysis	µCT

2.2. Introduction of representative volume elements

In the following, some fundamental rules defined in continuum micromechanics are reviewed, as a basis for establishing a suitable model representation for bone tissue, see Section 2.1. In continuum micromechanics, a material is thought to be macro-homogenous, but micro-heterogenous. Considering an arbitrary volume element hosting such material, this volume element is *representative* in terms of the physical behavior of the contained material if its characteristic length, ℓ_{RVE}, is "much" larger than the characteristic size of the micro-heterogeneities, d_{RVE}, within the RVE, i.e. $\ell_{\mathrm{RVE}} \gg d_{\mathrm{RVE}}$ (Hill, 1963; Zaoui, 2002; Dormieux et al., 2006). In particular, ℓ_{RVE} must be 2 to 3 times larger than d_{RVE} (Drugan and Willis, 1996) in order to comply with this requirement. On the other hand, ℓ_{RVE} must be considerably smaller than the characteristic length of the geometry of a structure composed of the material defined on the RVE, $\mathscr{L}$, as well as of the loading acting onto such a structure, $\mathscr{P}$. The requirement $\ell_{\mathrm{RVE}} \ll \{\mathscr{L}, \mathscr{P}\}$ is satisfyingly fulfilled as long as $\mathscr{L}$ and $\mathscr{P}$, respectively, are 5 to 10 times larger than ℓ_{RVE} (Kohlhauser and Hellmich, 2013).

The microstructure of the material contained within a representative volume element (RVE) is typically too complex to describe in its entirety. Instead, so-called material phases, assumed to be homogenous, are introduced. These material phases exhibit known physical properties, such as volume fractions or mechanical properties, and a variety of different phase morphologies can be established, thereby allowing the introduction of different phase shapes, and interactions between the considered material phases. Continuum micromechanics enables the derivation of mathematical relations which reconcile these conditions, for the eventual estimation of macroscopic (mechanical) properties valid on the level of the RVE, based on the corresponding phase properties. This upscaling process is often referred to as homogenization.

Homogenization can be carried out in a sequential fashion if a material phase itself exhibits a heterogeneous microstructure. In this case, an RVE can be introduced within the respective phase (Fritsch and Hellmich, 2007); the characteristic length of this new RVE, $\ell_{\mathrm{RVE,\,2}}$, must fulfil the requirement $\ell_{\mathrm{RVE,\,2}} \leq d_{\mathrm{RVE}}$, while the principle of scale separation demands that the characteristic length of the heterogeneities within the new RVE, $d_{\mathrm{RVE,\,2}}$, are considerably smaller than $\ell_{\mathrm{RVE,\,2}}$, i.e. $d_{\mathrm{RVE,\,2}} \ll \ell_{\mathrm{RVE,\,2}}$. This leads to a multi-step homogenization scheme, see Figure 2.2.

2.3. Model representation

For the development of a homogenization scheme allowing for estimation of the permeability of the multi-porous bone tissue, as defined in Section 2.1, a three-scale model representation is considered, see Figure 2.2.

Following the principle of scale separation as introduced in Section 2.2, the first RVE contains the canalicular pores, represented as cylindrical, arbitrarily oriented inclusions, which are interpenetrating, exhibiting a characteristic length of $d_{\text{can}} = 100$ nm, and the impermeable extracanalicular bone matrix phase, sometimes referred to as extracellular bone matrix. For the sake of simplicity, the extracanalicular phase is considered to be of spherical shape. Together, these two material phases form the polycrystalline extralacunar matrix which exhibits a characteristic length of $\ell_{\text{exlac}} = 0.5 - 2$ µm, thereby fulfilling $\ell_{\text{exlac}} \gg d_{\text{can}}$.

Zooming out from the smallest observation scale considered in this work, the RVE of extravascular material can be defined, consisting of a matrix of extralacunar material, and spherically shaped lacunar pores. The characteristic length of this RVE lies within the range of $\ell_{\text{exvas}} = 20 - 30$ µm, while the characteristic length of the lacunae is $d_{\text{lac}} = 10$ µm (Fritsch and Hellmich, 2007; Morin and Hellmich, 2014; Scheiner et al., 2015; Fritsch et al., 2009).

On an even larger scale of observation, macroscopic bone material can be identified at a characteristic length of $\ell_{\text{macro}} = 100 - 200$ µm. It is comprised of vascular pores, represented as cylindrical inhomogeneities with a characteristic length of $d_{\text{vas}} = 50$ µm, and the extravascular matrix. In order to cover different types of bone tissue, such as (osteonal) cortical and trabecular bone, as well as the transition zone in-between, i.e. endocortical bone, two morphologies are considered. Firstly, the vascular pores are introduced with a dominant orientation, and the extravascular bone material acts as a matrix phase hosting the pores as inclusions. This matrix-inclusion-type morphology reflects the situation in cortical bone, where Haversian canals mainly define the overall permeability. Secondly, cortical bone with a more pronounced importance of Volkmann canals, as well as trabecular bone is considered by introducing the vascular pores as an interpenetrating pore network in form of arbitrarily oriented inclusions, and the extravascular material modeled as spherical inclusions in-between.

Notably, similar modeling concepts have been developed previously in the field of bone (fluid) mechanics, e.g. to study stiffness (Hellmich et al., 2004; Fritsch and Hellmich, 2007), poroelasticity (Hellmich et al., 2009; Scheiner et al., 2015; Morin and Hellmich,

2014; Hellmich and Ulm, 2005), viscoelasticity (Eberhardsteiner et al., 2014), strength (Fritsch et al., 2009), and the trabecular permeability (Abdalrahman et al., 2015). All these works included substantial experimental validation, hence underpinning the adequacy of the chosen model representation.

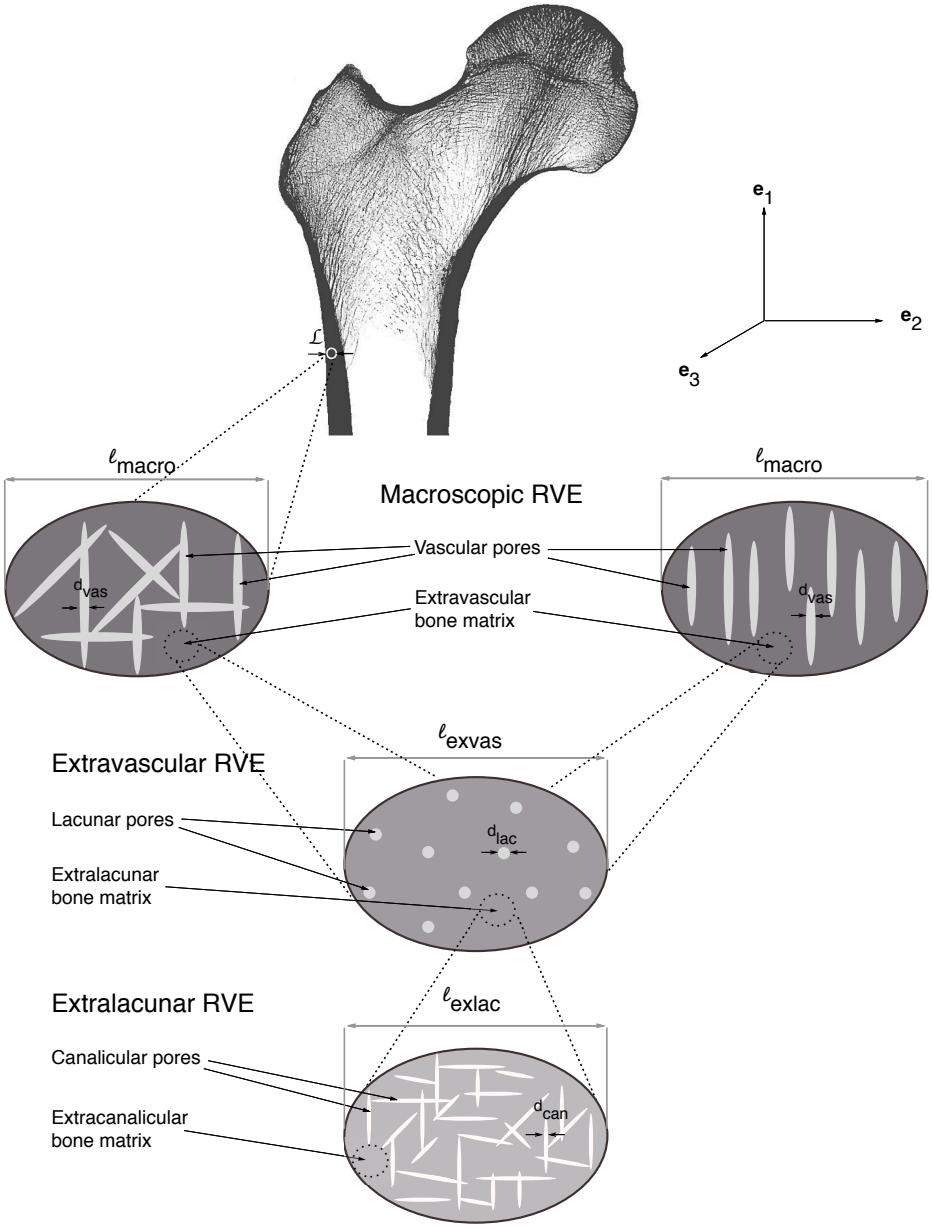

Figure 2.2.: Model representation based on which permeability upscaling and pressure gradient downscaling is performed, (from top to bottom) including the RVE of macroscopic bone tissue, which can represent both cortical bone (as indicated here) or trabecular bone (as seen in the radiograph of the coronal section of the femur (Jacobs et al., 1994)), containing vascular pores and extravascular matrix, arranged randomly or ordered, the RVE of extravascular bone material, containing lacunar pores and the extralacunar bone matrix, and the RVE of extralacunar bone material, consisting of canalicular pores and extracanalicular bone matrix

3. Development of a mathematical strategy for permeability upscaling and pressure gradient downscaling

In the following, a multi-step mathematical model is presented, allowing for interpreting the Poiseuille-type flow of pore fluid in the canalicular pores in terms of an equivalent micro-Darcy law, and to scale the respective permeability up to the macroscopic level. At the same time, the resulting mathematical framework allows for downscaling of pressure gradients from the macro- to the microscale. To that end, the work of Abdalrahman et al. (2015) served as a conceptual basis, and has been adapted according to the model representation elaborated in Section 2.3.

3.1. Step I: From the canalicular scale to extralacunar scale and vice versa

In the RVE of extralacunar material, two material phases can be found: canalicular pores and extracanalicular matrix.[5] As for the former, they are represented as long, cylindrical "tubes", mutually interconnected and interpenetrating, along which pressure gradient-driven fluid transport may occur, whereas the latter is considered to be impermeable, morphologically represented as a spherical material phase.

The laminar flow through one of these canalicular tubes is assumed to follow the well-known law of Hagen (1839) and Poiseuille (1847), see also (Sutera and Skalak, 1993): A quadratic velocity profile $v_{\mathrm{can}}(r,s)$ across the tube cross-section is triggered by a pressure gradient along the cylinder direction s, $\partial p/\partial s$, and influenced by the cylinder radius R_{can},

[5] In literature, the matrix that is referred to as "extracanalicular matrix" in this work, is usually termed "extracellular matrix" or "bone ultrastructure" (Fritsch and Hellmich, 2007).

and the dynamic fluid viscosity η; variable r denoting the radial coordinate within the tube cross-section. Mathematically, this law reads as

$$v_{\text{cylinder}}(r,s) = -\frac{\partial p}{\partial s}(s)\frac{R_{\text{can}}^2}{4\eta}\left(1-\frac{r^2}{R_{\text{can}}^2}\right). \tag{3.1}$$

To find the mean velocity $v_{\text{can}}(s)$ of the fluid in the canaliculi, the velocity distribution $v_{\text{cylinder}}(r,s)$ is averaged over the cross-sectional area A of the cylinder, yielding

$$\begin{aligned} v_{\text{can}}(s) &= \frac{1}{A}\int_A v_{\text{cylinder}}(r,s)\,\mathrm{d}A \\ &= \frac{2}{R_{\text{can}}^2}\int_0^{R_{\text{can}}} r v_{\text{cylinder}}(r,s)\,\mathrm{d}r\,. \end{aligned} \tag{3.2}$$

Upon inserting Eq. (3.1) into Eq. (3.2), the mean fluid velocity follows as a function of the canalicular radius, the pressure gradient along the longitudinal direction of the canalicular tube, i.e. in the direction of the unit vector $\mathbf{e}_{\text{s}}$, and the fluid viscosity:

$$v_{\text{can}}(s) = -\frac{R_{\text{can}}^2}{8\eta}\frac{\partial p}{\partial s}(s)\,. \tag{3.3}$$

In order to express the mean fluid velocity in vectorial format, $v_{\text{can}}(s)$ according to Eq. (3.3) has to be multiplied by the respective unit vector, yielding

$$\mathbf{v}_{\text{can}}(s) = v_{\text{can}}(s)\mathbf{e}_{\text{s}}\,. \tag{3.4}$$

Next, we aim to recast Eqs. (3.3) and (3.4) in form of a micro-Darcy law, as demonstrated in (Dormieux and Kondo, 2004, 2005; Dormieux et al., 2006),[6] connecting the vector of fluid velocity with the pressure gradient on the microscopic canalicular scale through a formal "canalicular permeability tensor". For that purpose, an alternative expression for v_{can}, is formulated in Darcy-fashion (i.e. considering incompressible fluids, and disre-

[6]Darcy considered experiments on the fluid flow through a vertical cylindrical column filled with sand between two reservoirs with different hydraulic heads, $H = P + \gamma x$, P being the macroscopic fluid pressure, $\gamma = \rho g$ the fluid unit weight and x the coordinate in vertical direction. He concluded that the flow per cross-section of sample is proportional to the difference in heads divided by the length of the sand column, which can be written as a pressure head gradient. The proportionality constant in this relation is defined as the permeability $\mathbf{K}$ and the flow $\mathbf{Q}$ is in the negative direction of the pressure gradient (Darcy, 1856):

$$\mathbf{Q} = \mathbf{K}\cdot(-\operatorname{grad} p_{\text{macro}} + \rho g)\,. \tag{3.5}$$

garding gravitational forces),

$$\mathbf{v}_{\mathrm{can}}(s) = -\mathbf{k}_{\mathrm{can}} \cdot \operatorname{grad} p \tag{3.6}$$

where the permeability related to the canalicular pores, $\mathbf{k}_{\mathrm{can}}$, can be found by comparing Eqs. (3.3) and (3.6):

$$\begin{aligned} \mathbf{k}_{\mathrm{can}} &= \frac{R_{\mathrm{can}}^2}{8\eta} \begin{pmatrix} 1 & 0 & 0 \\ 0 & 0 & 0 \\ 0 & 0 & 0 \end{pmatrix}_{\mathbf{e}_{\mathrm{s}},\mathbf{e}_{\mathrm{t}},\mathbf{e}_{\mathrm{u}}} \\ &= \frac{R_{\mathrm{can}}^2}{8\eta} \mathbf{e}_{\mathrm{s}} \otimes \mathbf{e}_{\mathrm{s}} \,, \end{aligned} \tag{3.7}$$

where symbol $\otimes$ denotes the dyadic product. The coordinate system defined by unit vectors $\mathbf{e}_{\mathrm{s}}, \mathbf{e}_{\mathrm{t}}, \mathbf{e}_{\mathrm{u}}$ is orthogonal, with $\mathbf{e}_{\mathrm{s}}$ pointing in the direction of the long cylinder axis.

Following Abdalrahman et al. (2015), the work of Dormieux and Kondo (2004) and Dormieux et al. (2006) has been taken as a guideline for the permeability homogenization on the extralacunar scale, where the canalicular pores mutually interact with impenetrable bone matrix inclusions (which are presumably of spherical shape). In particular, it is assumed that a macroscopic, homogenous pressure gradient, $\operatorname{grad} p_{\mathrm{exlac}}$, acts on the boundary of the extralacunar RVE:

$$\forall \mathbf{x} \in \partial V_{\mathrm{RVE}} : p(\mathbf{x}) = \operatorname{grad} p_{\mathrm{exlac}} \cdot \mathbf{x} \,. \tag{3.8}$$

The macroscopic pressure gradient, $\operatorname{grad} p_{\mathrm{exlac}}$, can be related to the microscopic one, $\operatorname{grad} p$, by making use of Eq. (3.8), and volume and surface integral operations, yielding

$$\int_{V_{\mathrm{RVE}}} \operatorname{grad} p(\mathbf{x}) \mathrm{d}V = V_{\mathrm{RVE}} \operatorname{grad} p_{\mathrm{exlac}} \,. \tag{3.9}$$

Thereby, the integration over the RVE volume V_{RVE} was turned into a surface integral over the boundary $\partial V_{\mathrm{RVE}}$ using the Gauss (or divergence) theorem. The pressure gradient average rule follows from rearanging Eq. (3.9):

$$\operatorname{grad} p_{\mathrm{exlac}} = \frac{1}{V_{\mathrm{RVE}}} \int_{V_{\mathrm{RVE}}} \operatorname{grad} p(\mathbf{x}) \mathrm{d}V \,. \tag{3.10}$$

Furthermore, an average rule relating the macroscopic velocity $\mathbf{v}_{\text{exlac}}$ and the microscopic velocities $\mathbf{v}(\mathbf{x})$ needs to be established. For that purpose, mass conservation is considered:

$$\forall \mathbf{x} \in V : \operatorname{div} \mathbf{v}(\mathbf{x}) = 0\,. \tag{3.11}$$

Then, it is considered that the dissipated energy due to triggering a macro-velocity through the macroscopic pressure gradient is equivalent to triggering of all the micro-velocities through the microscopic pressure gradients (Abdalrahman et al., 2015), yielding

$$\int_{V_{\text{RVE}}} \mathbf{v}(\mathbf{x}) \cdot \operatorname{grad} p(\mathbf{x}) \mathrm{d}V = V_{\text{RVE}} \mathbf{v}_{\text{exlac}} \operatorname{grad} p_{\text{exlac}}\,. \tag{3.12}$$

Making use of the divergence theorem again, Eqs. (3.8) and (3.11) imply that the expression on the left-hand side of Eq. (3.12) can be rewritten as

$$\int_{V_{\text{RVE}}} \mathbf{v}(\mathbf{x}) \cdot \operatorname{grad} p(\mathbf{x}) \mathrm{d}V = \operatorname{grad} p_{\text{exlac}} \int_{V_{\text{RVE}}} \mathbf{v}(\mathbf{x}) \mathrm{d}V\,. \tag{3.13}$$

Combining Eqs. (3.12) and (3.13) then gives access to the average rule for the velocities:

$$\mathbf{v}_{\text{exlac}} = \frac{1}{V_{\text{RVE}}} \int_{V_{\text{RVE}}} \mathbf{v}(\mathbf{x}) \mathrm{d}V\,. \tag{3.14}$$

In order to define the direction of the canaliculi, which are considered to be randomly oriented in space (see Figure 2.2 for the chosen model representation), a coordinate system defined by unit vectors $\mathbf{e}_{\text{s}}$, $\mathbf{e}_{\vartheta}$, and $\mathbf{e}_{\varphi}$ is fixed to each pore with $\mathbf{e}_{\text{s}}$ aligning with the longitudinal direction of the canaliculi. The (Euler) angles ϑ and φ signify the orientation of the local system compared to the global reference base frame ($\mathbf{e}_1$, $\mathbf{e}_2$, $\mathbf{e}_3$), see Figure 3.1. With these conventions, the dependency of the fluid velocities on the local coordinates can be specified:

$$\mathbf{v}_{\text{can}}(\vartheta, \varphi) = v_{\text{can}} \mathbf{e}_{\text{s}}(\vartheta, \varphi)\,, \tag{3.15}$$

with v_{can} being the average of the tube velocity over the canalicular length,

$$\mathbf{v}_{\text{can}}(\vartheta, \varphi) = \frac{1}{l_{\text{can}}} \int_{l_{\text{can}}} v(\mathbf{x}) \mathbf{e}_{\text{s}}(\vartheta, \varphi)\, \mathrm{d}s \tag{3.16}$$

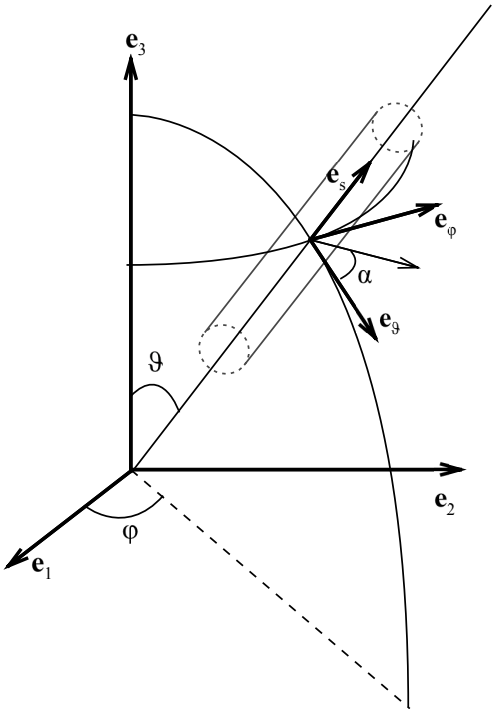

Figure 3.1.: Cylindrically shaped inclusion, longitudinally oriented along the unit vector $\mathbf{e}_s$, and inclined by Euler angles φ and ϑ with respect to the reference base frame, ($\mathbf{e}_1$, $\mathbf{e}_2$, $\mathbf{e}_3$); the local base frame, defined by the unit vectors $\mathbf{e}_s$, $\mathbf{e}_\vartheta$, and $\mathbf{e}_\varphi$ is attached to the inclusion

Introducing the micro-Darcy law defined in Eq. (3.6) into Eq. (3.16) yields

$$\mathbf{v}_{\text{can}} = \frac{1}{l_{\text{can}}} \int\limits_{l_{\text{can}}} [-\mathbf{k}_{\text{can}}(\vartheta,\varphi)] \cdot \frac{\partial p}{\partial s} \mathbf{e}_s(\vartheta,\varphi)\, \mathrm{d}s\,. \tag{3.17}$$

Employing the velocity and pressure gradient averaging rules next, see Eqs. (3.14) and (3.10), yields

$$\mathbf{v}_{\text{exlac}} = \tilde{f}_{\text{can}} \int\limits_{\varphi=0}^{2\pi} \int\limits_{\vartheta=0}^{\pi} v_{\text{can}} \mathbf{e}_s(\vartheta,\varphi) \frac{\sin\vartheta}{4\pi} \mathrm{d}\varphi \mathrm{d}\vartheta\,, \tag{3.18}$$

and

$$\operatorname{grad} p_{\text{exlac}} = \tilde{f}_{\text{can}} \int\limits_{\varphi=0}^{2\pi} \int\limits_{\vartheta=0}^{\pi} \frac{\partial p}{\partial s} \mathbf{e}_s(\vartheta,\varphi) \frac{\sin\vartheta}{4\pi} \mathrm{d}\varphi \mathrm{d}\vartheta + (1-\tilde{f}_{\text{can}}) \operatorname{grad} p_{\text{excan}}\,. \tag{3.19}$$

Notably, $\tilde{f}_{\text{can}}$ is the volume fraction of the canalicular pores in the RVE of extralacunar material, hence defined as the ratio of the canalicular volume, V_{can}, over the total volume

of the extralacunar material, V_{exlac},

$$\tilde{f}_{\mathrm{can}} = \frac{V_{\mathrm{can}}}{V_{\mathrm{exlac}}}\,, \tag{3.20}$$

which is related to the canalicular porosity defined on the macroscopic level, f_{can} by

$$\tilde{f}_{\mathrm{can}} = \frac{\bar{f}_{\mathrm{can}}}{1-\bar{f}_{\mathrm{lac}}} = \frac{f_{\mathrm{can}}}{(1-\bar{f}_{\mathrm{lac}})(1-f_{\mathrm{vas}})}\,, \tag{3.21}$$

via the lacunar porosity of the extravascular material, $\bar{f}_{\mathrm{lac}}$, and the vascular porosity of the macroscopic material, f_{vas}. The average pressure gradient outside the canaliculi in the solid matrix is $\operatorname{grad} p_{\mathrm{excan}}$, and the corresponding velocity $\mathbf{v}_{\mathrm{excan}}$ is zero.

Given the linearity of $\mathbf{v}_{\mathrm{can}}(\vartheta,\varphi)$ with the microscopic pressure gradient in Eq. (3.17), and the linearity of the mass balance law given in Eq. (3.11), a linear link between microscopic and macroscopic pressure gradients can be established via pressure gradient concentration tensors $\mathbf{A}_{\mathrm{can}}$ (Dormieux and Kondo, 2004; Dormieux et al., 2006; Abdalrahman et al., 2015). This pressure gradient concentration relation reads as

$$\frac{\partial p}{\partial s}\mathbf{e}_{\mathrm{s}}(\vartheta,\varphi) = \operatorname{grad} p_{\mathrm{can}}(\vartheta,\varphi) = \mathbf{A}_{\mathrm{can}}(\vartheta,\varphi)\cdot\operatorname{grad} p_{\mathrm{exlac}}\,, \tag{3.22}$$

and, analogously,

$$\operatorname{grad} p_{\mathrm{excan}} = \mathbf{A}_{\mathrm{excan}}\cdot\operatorname{grad} p_{\mathrm{exlac}}\,, \tag{3.23}$$

with the extracanalicular concentration tensor, $\mathbf{A}_{\mathrm{excan}}$. Inserting Eq. (3.22) into Eq. (3.18), reveals the connection between the macroscopic velocity and the macroscopic pressure gradient, under consideration of the underlying microscopic quantities:

$$\mathbf{v}_{\mathrm{exlac}} = \left[\tilde{f}_{\mathrm{can}}\int_{\varphi=0}^{2\pi}\int_{\vartheta=0}^{\pi}\left[-\mathbf{k}_{\mathrm{can}}(\vartheta,\varphi)\right]\cdot\mathbf{A}_{\mathrm{can}}(\vartheta,\varphi)\frac{\sin\vartheta}{4\pi}\mathrm{d}\varphi\mathrm{d}\vartheta\right]\cdot\operatorname{grad} p_{\mathrm{exlac}}\,. \tag{3.24}$$

so that

$$\mathbf{v}_{\mathrm{exlac}} = -\mathbf{K}^{\mathrm{hom}}_{\mathrm{exlac}}\cdot\operatorname{grad} p_{\mathrm{exlac}}\,. \tag{3.25}$$

By inserting the microscopic permeability tensor from Eq. (3.7) into Eq. (3.22), the homogenized permeability tensor in the extralacunar space, $\mathbf{K}^{\mathrm{hom}}_{\mathrm{exlac}}$, can be written as

$$\mathbf{K}^{\mathrm{hom}}_{\mathrm{exlac}} = \tilde{f}_{\mathrm{can}}\int_{\varphi=0}^{2\pi}\int_{\vartheta=0}^{\pi}\frac{R^2_{\mathrm{can}}}{8\eta}\left[\mathbf{e}_{\mathrm{s}}(\vartheta,\varphi)\otimes\mathbf{e}_{\mathrm{s}}(\vartheta,\varphi)\right]\cdot\mathbf{A}_{\mathrm{can}}(\vartheta,\varphi)\frac{\sin\vartheta}{4\pi}\mathrm{d}\varphi\mathrm{d}\vartheta\,. \tag{3.26}$$

The next step is to further define the pressure gradient concentration tensor $\mathbf{A}_{\text{can}}$. For that purpose, classical continuum mechanics (Zaoui, 2002) is utilized for transport in porous media, by adapting Eshelby's matrix-inclusion problem (Eshelby, 1957). In particular, the boundary condition

$$\text{for } x \to \infty : p(\mathbf{x}) = (\text{grad}\, p_{\text{exlac}})_{\infty} \cdot \mathbf{x} \tag{3.27}$$

is applied to an infinite domain, hosting a cylindrical inhomogeneity (or inclusion) of permeability $\mathbf{k}_{\text{inclusion}}$, while the surrounding matrix exhibits the isotropic permeability $\mathbf{K}_{\text{matrix}} = K_{\text{matrix}} \cdot \mathbf{1}$, with $\mathbf{1}$ being the second-order unit tensor. The pressure gradient in the inclusion then follows as

$$\text{grad}\, p_{\text{inclusion}} = \left[\mathbf{1} + \mathbf{P} \cdot (\mathbf{k}_{\text{inclusion}} - \mathbf{1} K_{\text{matrix}})\right]^{-1} \cdot (\text{grad}\, p_{\text{exlac}})_{\infty}\,. \tag{3.28}$$

where $\mathbf{P}$ is the Hill or inhomogeneity tensor defined as (Dormieux and Kondo, 2005)

$$\mathbf{P} = \sum_{i=1}^{3} \sum_{j=1}^{3} -\frac{1}{4\pi K_{\text{matrix}}} \frac{\partial^2 \psi}{\partial \xi_i \partial \xi_j} \mathbf{e}_i \otimes \mathbf{e}_j\,. \tag{3.29}$$

The Cartesian coordinates ξ_i and ξ_j originate from the center of the cylindrical inhomogeneity. When considering $\mathbf{e}_{\text{s}}$, $\mathbf{e}_{\vartheta}$, and $\mathbf{e}_{\varphi}$ as base vectors, aligning with the major axis of the cylinder, the location vectors can be written as $\boldsymbol{\xi} = \sum_{i=\varphi,\vartheta} \xi_i \mathbf{e}_i$. To derive the potential function ψ, the Green's function for the specific (diffusion) inclusion problem,

$$\psi(\boldsymbol{\xi}) = \int\limits_{V_{\text{inclusion}}} \frac{1}{\boldsymbol{\xi} - \boldsymbol{\xi}'} \mathrm{d}V_{\boldsymbol{\xi}'}\,, \tag{3.30}$$

needs to be found. It becomes apparent that the potential function only depends on the geometry of the inclusion, so for the present case, two potential functions must be considered, one relating to the canalicular pores, and one to the extracanalicular bone matrix.

Starting with the canaliculi, the consideration of a cylindrical shape is recalled, oriented in (ϑ, φ)-direction (Abdalrahman et al., 2015):

$$\psi_{\text{can}} = \pi \left(r^2 - R_{\text{can}}^2\right)\,. \tag{3.31}$$

After inserting the polar coordinates $\xi_1 = r\cos\alpha$, $\xi_2 = r\sin\alpha$ and $r^2 = \xi_1^2 + \xi_2^2$ (r, the radial polar coordinate and α, the angular polar coordinate) into Eq. (3.31), and subsequently into Eq. (3.29), the inhomogeneity tensor related to the canalicular pores follows

as

$$\mathbf{P}_{\text{can}} = \frac{1}{2K_{\text{matrix}}} \begin{pmatrix} 0 & 0 & 0 \\ 0 & 1 & 0 \\ 0 & 0 & 1 \end{pmatrix}_{\mathbf{e}_s, \mathbf{e}_\vartheta, \mathbf{e}_\varphi} . \tag{3.32}$$

Alternatively, $\mathbf{P}_{\text{can}}$ can be given in the base frame $(\mathbf{e}_1, \mathbf{e}_2, \mathbf{e}_3)$, by applying a standard transformation from spherical coordinates into Cartesian coordinates:

$$\mathbf{P}_{\text{can}}(\vartheta, \varphi) = \mathbf{R}\mathbf{P}_{\text{can}}\mathbf{R}^T , \tag{3.33}$$

with

$$\mathbf{R} = \begin{pmatrix} \sin\vartheta\cos\varphi & \cos\vartheta\cos\varphi & -\sin\varphi \\ \sin\vartheta\sin\varphi & \cos\vartheta\sin\varphi & \cos\varphi \\ \cos\vartheta & -\sin\vartheta & 0 \end{pmatrix} . \tag{3.34}$$

Eventually, the Eshelbian relation (3.28) for the canalicular inclusions can be written as

$$\begin{aligned} \operatorname{grad} p_{\text{can}}(\vartheta, \varphi) = \frac{\partial p}{\partial s}\mathbf{e}_s(\vartheta, \varphi) = \\ [\mathbf{1} + \mathbf{P}_{\text{can}}(\vartheta, \varphi) \cdot (\mathbf{k}_{\text{can}}(\vartheta, \varphi) - \mathbf{1}K_{\text{matrix}})]^{-1} (\operatorname{grad} p_{\text{exlac}})_\infty . \end{aligned} \tag{3.35}$$

Next, a spherical inclusion is regarded, as a representation of the solid (and impermeable) extracanalicular material phase, with R_{sphere} defining the radius of the inclusion. Accordingly, the potential function of a sphere is considered, as suggested by Dormieux et al. (2006), reading as

$$\psi_{\text{excan}} = \frac{2\pi R_{\text{sphere}}^2}{3} \left(3 - \frac{r^2}{R_{\text{sphere}}^2} \right) . \tag{3.36}$$

Appropriate parametrization, namely through $\psi_1 = r\sin\alpha_1\cos\alpha_2$, $\psi_2 = r\sin\alpha_1\sin\alpha_2$, $\psi_3 = r\cos\alpha_2$, r being the radial spherical coordinate with the corresponding longitudinal and latitudinal angles α_1 and α_2, and $r^2 = \psi_1^2 + \psi_2^2 + \psi_3^2$, as well as utilizing Eqs. (3.36) and (3.29), yields the inhomogeneity tensor, $\mathbf{P}_{\text{excan}}$:

$$\mathbf{P}_{\text{excan}} = \frac{1}{3K_{\text{matrix}}} \begin{pmatrix} 1 & 0 & 0 \\ 0 & 1 & 0 \\ 0 & 0 & 1 \end{pmatrix}_{\mathbf{e}_s, \mathbf{e}_\vartheta, \mathbf{e}_\varphi} . \tag{3.37}$$

With the solid matrix being impermeable, the Eshelbian relation (3.28) can be written as

$$\operatorname{grad} p_{\text{excan}} = [\mathbf{1} - \mathbf{P}_{\text{excan}} \cdot \mathbf{1}K_{\text{matrix}}]^{-1} (\operatorname{grad} p_{\text{exlac}})_\infty . \tag{3.38}$$

Both expressions for the microscopic gradients $\operatorname{grad} p_{\mathrm{can}}$ and $\operatorname{grad} p_{\mathrm{excan}}$, see Eqs. (3.35) and (3.38), are inserted into Eq. (3.19), in order to obtain

$$\begin{aligned}\operatorname{grad} p_{\mathrm{exlac}} = \Bigg[\tilde{f}_{\mathrm{can}} \int_{\varphi=0}^{2\pi} \int_{\vartheta=0}^{\pi} \frac{\sin\vartheta}{4\pi} [\mathbf{1} + \mathbf{P}_{\mathrm{can}}(\vartheta,\varphi) \cdot (\mathbf{k}_{\mathrm{can}}(\vartheta,\varphi) - \mathbf{1} K_{\mathrm{matrix}})]^{-1} \mathrm{d}\vartheta \mathrm{d}\varphi \\ + (1-\tilde{f}_{\mathrm{can}}) [\mathbf{1} - \mathbf{P}_{\mathrm{excan}} \cdot \mathbf{1} K_{\mathrm{matrix}}]^{-1} \Bigg] \cdot (\operatorname{grad} p_{\mathrm{exlac}})_{\infty} \,.\end{aligned} \tag{3.39}$$

Inserting Eq. (3.39) into Eq. (3.35), the pressure gradient concentration tensor related to the canalicular pores follows as

$$\begin{aligned}\mathbf{A}_{\mathrm{can}}(\vartheta,\varphi) = \big[\mathbf{1} + \mathbf{P}_{\mathrm{can}}(\vartheta,\varphi) \cdot (\mathbf{k}_{\mathrm{can}}(\vartheta,\varphi) - \mathbf{1} K^{\mathrm{hom}}_{\mathrm{exlac}})\big]^{-1} \cdot \\ \Bigg[\tilde{f}_{\mathrm{can}} \int_{\varphi=0}^{2\pi} \int_{\vartheta=0}^{\pi} \frac{\sin\vartheta}{4\pi} [\mathbf{1} + \mathbf{P}_{\mathrm{can}}(\vartheta,\varphi) \cdot (\mathbf{k}_{\mathrm{can}}(\vartheta,\varphi) - \mathbf{1} K^{\mathrm{hom}}_{\mathrm{exlac}})]^{-1} \mathrm{d}\vartheta \mathrm{d}\varphi \\ + (1-\tilde{f}_{\mathrm{can}}) [\mathbf{1} - \mathbf{P}_{\mathrm{excan}} \cdot \mathbf{1} K^{\mathrm{hom}}_{\mathrm{exlac}}]^{-1} \Bigg]^{-1} \,.\end{aligned} \tag{3.40}$$

Considering in Eq. (3.40) the inhomogeneity tensors according to Eqs. (3.32) and (3.37), as well as the canalicular permeability according to Eq. (3.7) allows the derivation of

$$\begin{aligned}&\mathbf{A}_{\mathrm{can}}(\vartheta,\varphi) \\ &= \begin{pmatrix} -\frac{3\left(-2\cos^2\varphi\cos(2\vartheta)+\cos(2\varphi)-7\right)}{2(\tilde{f}_{\mathrm{can}}+9)} & -\frac{3\sin(2\varphi)\sin^2(\vartheta)}{\tilde{f}_{\mathrm{can}}+9} & -\frac{6\cos\varphi\sin\vartheta\cos\vartheta}{\tilde{f}_{\mathrm{can}}+9} \\ -\frac{3\sin(2\varphi)\sin^2(\vartheta)}{\tilde{f}_{\mathrm{can}}+9} & \frac{3\left(2\sin^2\varphi\cos(2\vartheta)+\cos(2\varphi)+7\right)}{2(\tilde{f}_{\mathrm{can}}+9)} & -\frac{6\sin\varphi\sin\vartheta\cos\vartheta}{\tilde{f}_{\mathrm{can}}+9} \\ -\frac{6\cos\varphi\sin\vartheta\cos\vartheta}{\tilde{f}_{\mathrm{can}}+9} & -\frac{6\sin\varphi\sin\vartheta\cos\vartheta}{\tilde{f}_{\mathrm{can}}+9} & -\frac{3(\cos(2\vartheta)-3)}{\tilde{f}_{\mathrm{can}}+9} \end{pmatrix} .\end{aligned} \tag{3.41}$$

Analogously, the pressure concentration tensor related to the extracanalicular matrix is obtained:

$$\begin{aligned}\mathbf{A}_{\text{excan}} =& \left[\mathbf{1}-\mathbf{P}_{\text{excan}}\cdot\mathbf{1}K^{\text{hom}}_{\text{exlac}})\right]^{-1}\cdot \\ & \left[\tilde{f}_{\text{can}}\int_{\varphi=0}^{2\pi}\int_{\vartheta=0}^{\pi}\frac{\sin\vartheta}{4\pi}[\mathbf{1}+\mathbf{P}_{\text{can}}(\vartheta,\varphi)\cdot(\mathbf{k}_{\text{can}}(\vartheta,\varphi)-\mathbf{1}K^{\text{hom}}_{\text{exlac}})]^{-1}\text{d}\vartheta\text{d}\varphi\right. \\ & \left.+(1-\tilde{f}_{\text{can}})[\mathbf{1}-\mathbf{P}_{\text{excan}}\cdot\mathbf{1}K^{\text{hom}}_{\text{exlac}}]^{-1}\right]^{-1} \\ =& \frac{9}{9+f_{\text{can}}}\mathbf{1}\,.\end{aligned} \tag{3.42}$$

The two pressure gradient concentration tensors give access, on the one hand, when inserting them into Eq. (3.26), to the homogenized permeability of the extralacunar matrix, $\mathbf{K}^{\text{hom}}_{\text{exlac}} = K^{\text{hom}}_{\text{exlac}}\cdot\mathbf{1}$, with

$$K^{\text{hom}}_{\text{exlac}} = \frac{\tilde{f}_{\text{can}}R^2_{\text{can}}}{4\eta(9+\tilde{f}_{\text{can}})}\,, \tag{3.43}$$

and, on the other hand, when inserting them into Eqs. (3.22) and (3.23), pressure gradients in the canaliculi and in the extracanalicular matrix, reading as

$$\text{grad}\,p_{\text{can}}(\vartheta,\varphi) = \mathbf{A}_{\text{can}}(\vartheta,\varphi)\cdot\text{grad}\,p_{\text{exlac}}\,, \tag{3.44}$$

and

$$\text{grad}\,p_{\text{excan}} = \mathbf{A}_{\text{excan}}\cdot\text{grad}\,p_{\text{exlac}}\,. \tag{3.45}$$

3.2. Step II: From the lacunar/extralacunar scales to the extravascular scale and vice versa

Reiterating from Section 2.3, an RVE of extravascular bone is composed of the spherically shaped lacunar pores which are embedded in extralacunar matrix. While the latter has been dealt with in Section 3.1, the definition of the permeability representing the fluid flow in the lacunar pores requires some further elaboration. For that purpose, the work of Markov et al. (2009) is regarded. They considered spherical inclusions embedded in a porous domain, and analyzed the pressure gradient-driven fluid flow across such a domain by means of a Stokes analysis. The such computed fluid flow was then set equal to a quasi-Darcy law (analogous to the strategy pursued in Section 3.1), allowing the back-analysis

of a corresponding permeability related to the lacunar pores. In particular, Markov et al. (2009) chose the boundary conditions concerning the continuity of the normal pressure and the normal velocity components as suggested by Saffman (1971), himself thereby adopting the seminal work of Beavers and Joseph (1967). Tying in with these works, the following definition of the fluid flow velocity component, oriented tangentially to the inclusion, v_t, at the interface between the inclusion and the pore medium can be found:

$$v_\mathrm{t} = \lambda \sqrt{K_\mathrm{pormat}} \frac{\partial v_\mathrm{t}}{\partial y}, \tag{3.46}$$

where λ is the dimensionless, semi-empirical slip coefficient varying between 0 and 5,[7] and K_pormat is the permeability of the porous matrix. According to Markov et al. (2009), the permeability related to the lacunar inclusions, $\mathbf{k}_\mathrm{lac}$, embedded in the extralacunar matrix, eventually follows as

$$\mathbf{k}_\mathrm{lac} = \frac{R_\mathrm{lac}^2}{6} \left(1 - 4 \frac{\lambda \sqrt{K_\mathrm{exlac}^\mathrm{hom}}}{R_\mathrm{lac}} \right) \cdot \begin{pmatrix} 1 & 0 & 0 \\ 0 & 1 & 0 \\ 0 & 0 & 1 \end{pmatrix}, \tag{3.47}$$

where R_lac is the lacunar radius and $K_\mathrm{exlac}^\mathrm{hom}$ is the component of the isotropic, homogenized extralacunar permeability tensor.

The aforementioned slip coefficient, λ, deserves a closer look. It was first introduced by Beavers and Joseph (1967) and needs to be evaluated experimentally. In order to establish the boundary condition given in Eq. (3.46), they assumed that the uniform pressure gradients in the fluid flow domain and the porous medium are the same in longitudinal direction along the interface. The slip velocity v_slip is defined as the difference between the velocities in the fluid domain on the one side of the interface, v_f, and the velocity on the other side, v_pores, governed by the Darcy law in the porous medium. Beavers and Joseph (1967) stipulated that this slip velocity is proportional to the shear rate at the interface:

$$\left. \frac{\partial v_\mathrm{slip}}{\partial y} \right|_{y=0^+} = \frac{\beta}{\sqrt{K_\mathrm{pormat}}} (v_\mathrm{f} - v_\mathrm{pores}), \tag{3.48}$$

with $y = 0^+$ indicating that the gradient is evaluated at the interface, towards the fluid phase. Thus, a proportionality constant β is introduced, mainly defined by the surface structure of the porous medium; β is independent of the fluid viscosity (Beavers and

[7] The indicated range for λ, $\lambda \in [0, 5]$, follows from the experiments conducted by Beavers and Joseph (1967); they measured the flow through different kinds of metallic materials with varying pore sizes.

Joseph, 1967), but depends on the flow direction, the Reynolds number, the width of the inclusion, and on the normal distance from the interface, y, chosen for measuring both the Darcy velocity and the velocity in the fluid (Sahraoui and Kaviany, 1991). Furthermore, according to Beavers and Joseph (1967), β increases linearly with the porosity of the solid material. These dependencies were verified in the flow experiments of Sahraoui and Kaviany (1991). Saffman's boundary condition, being an approximation of the one considered by Beavers and Joseph (1967) for small pore sizes, also contains the aforementioned proportionality coefficient, in form of $\lambda = \beta^{-1}$.

Upscaling of $\mathbf{k}_{\mathrm{lac}}$ and $K^{\mathrm{hom}}_{\mathrm{exlac}}$ to the extravascular level is done analogously to the first step, see Section 3.1:

$$\mathbf{K}^{\mathrm{hom}}_{\mathrm{exvas}} = \bar{f}_{\mathrm{lac}}\mathbf{k}_{\mathrm{lac}} \cdot \mathbf{A}_{\mathrm{lac}} + (1-\bar{f}_{\mathrm{lac}})\mathbf{K}^{\mathrm{hom}}_{\mathrm{exlac}} \cdot \mathbf{A}_{\mathrm{exlac}}\,, \tag{3.49}$$

where $\bar{f}_{\mathrm{lac}}$ is the lacunar porosity quantified in the extravascular RVE, related to the macroscopic lacunar porosity via

$$\bar{f}_{\mathrm{lac}} = \frac{f_{\mathrm{lac}}}{(1-f_{\mathrm{vas}})}\,, \tag{3.50}$$

while $\mathbf{A}_{\mathrm{lac}}$ and $\mathbf{A}_{\mathrm{exlac}}$ are the pressure gradient concentration tensors relating the extravascular pressure gradient to the lacunar and extralacunar gradients. These two concentration tensors are based on a Mori-Tanaka-type scheme (Mori and Tanaka, 1973), owing to the matrix-inclusion type morphology of the extravascular RVE, yielding

$$\begin{aligned}\mathbf{A}_{\mathrm{lac}} = &\left[\mathbf{1} + \mathbf{P}_{\mathrm{lac}} \cdot (\mathbf{k}_{\mathrm{lac}} - \mathbf{1}K_{\mathrm{exlac}})\right]^{-1} \cdot \\ &\left[\bar{f}_{\mathrm{lac}}[\mathbf{1} + \mathbf{P}_{\mathrm{lac}} \cdot (\mathbf{k}_{\mathrm{lac}} - \mathbf{1}K_{\mathrm{exlac}})]^{-1} + (1-\bar{f}_{\mathrm{lac}})\mathbf{1}\right]^{-1},\end{aligned} \tag{3.51}$$

and

$$\mathbf{A}_{\mathrm{exlac}} = \left[\bar{f}_{\mathrm{lac}}[\mathbf{1} + \mathbf{P}_{\mathrm{lac}} \cdot (\mathbf{k}_{\mathrm{lac}} - \mathbf{1}K_{\mathrm{exlac}})]^{-1} + (1-\bar{f}_{\mathrm{lac}})\mathbf{1}\right]^{-1}. \tag{3.52}$$

Thereby, the inhomogeneity tensor $\mathbf{P}_{\mathrm{lac}}$ is defined analogously to $\mathbf{P}_{\mathrm{excan}}$, namely as

$$\mathbf{P}_{\mathrm{lac}} = \frac{1}{3K^{\mathrm{hom}}_{\mathrm{exlac}}} \cdot \begin{pmatrix} 1 & 0 & 0 \\ 0 & 1 & 0 \\ 0 & 0 & 1 \end{pmatrix}. \tag{3.53}$$

Inserting Eq. (3.53) into Eqs. (3.51) and (3.52), while also considering $\mathbf{k}_{\mathrm{lac}}$ according to Eq. (3.47) and $\mathbf{K}_{\mathrm{exlac}}^{\mathrm{hom}}$ according to Eq. (3.43), yields

$$\begin{aligned}\mathbf{A}_{\mathrm{lac}} =& 9 f_{\mathrm{can}} R_{\mathrm{can}}^2 \Bigg/ \\ & \left(18\eta(f_{\mathrm{lac}}-1)R_{\mathrm{lac}} \left(2\lambda \sqrt{\frac{f_{\mathrm{can}} R_{\mathrm{can}}^2}{\eta(f_{\mathrm{can}}+9)}} - R_{\mathrm{lac}} \right) + \right. \\ & \left. f_{\mathrm{can}} \left(2\eta(f_{\mathrm{lac}}-1)R_{\mathrm{lac}} \left(2\lambda \sqrt{\frac{f_{\mathrm{can}} R_{\mathrm{can}}^2}{\eta(f_{\mathrm{can}}+9)}} - R_{\mathrm{lac}} \right) + 3(f_{\mathrm{lac}}+2)R_{\mathrm{can}}^2 \right) \right) \mathbf{1}\,,\end{aligned} \tag{3.54}$$

and

$$\begin{aligned}\mathbf{A}_{\mathrm{exlac}} =& \left[9 f_{\mathrm{lac}} f_{\mathrm{can}} R_{\mathrm{can}}^2 \Bigg/ \left(18\eta R_{\mathrm{lac}} \left(R_{\mathrm{lac}} - 2\lambda \sqrt{\frac{f_{\mathrm{can}} R_{\mathrm{can}}^2}{\eta(f_{\mathrm{can}}+9)}} \right) + \right. \right. \\ & \left. \left. 2\eta f_{\mathrm{can}} R_{\mathrm{lac}} \left(R_{\mathrm{lac}} - 2\lambda \sqrt{\frac{R_{\mathrm{can}} R_{\mathrm{can}}^2}{\eta(f_{\mathrm{can}}+9)}} \right) + 6 f_{\mathrm{can}} R_{\mathrm{can}}^2 \right) - f_{\mathrm{lac}} + 1 \right]^{-1},\end{aligned} \tag{3.55}$$

and, when inserting these expressions into Eq. (3.49),

$$\begin{aligned}K_{\mathrm{exvas}}^{\mathrm{hom}} =& -2K_{\mathrm{exlac}}^{\mathrm{hom}} \times \\ & \Big(-3\tilde{f}_{\mathrm{can}} + 3\tilde{f}_{\mathrm{can}}\bar{f}_{\mathrm{lac}} + \frac{R_{\mathrm{lac}}}{R_{\mathrm{can}}}(\eta\lambda m)(18 + 2\tilde{f}_{\mathrm{can}} + 36\bar{f}_{\mathrm{lac}} + 4\tilde{f}_{\mathrm{can}}\bar{f}_{\mathrm{lac}}) + \\ & \left(\frac{R_{\mathrm{lac}}}{R_{\mathrm{can}}} \right)^2 \eta(-9 - \tilde{f}_{\mathrm{can}} - 18\bar{f}_{\mathrm{lac}} - 2\tilde{f}_{\mathrm{can}}\bar{f}_{\mathrm{lac}}) \Big) \times \\ & \Big(6\tilde{f}_{\mathrm{can}} + 3\tilde{f}_{\mathrm{can}}\bar{f}_{\mathrm{lac}} - \frac{R_{\mathrm{lac}}}{R_{\mathrm{can}}}(\eta\lambda m)(36 + 4\tilde{f}_{\mathrm{can}} - 36\bar{f}_{\mathrm{lac}} - 4\tilde{f}_{\mathrm{can}}\bar{f}_{\mathrm{lac}}) + \\ & \left(\frac{R_{\mathrm{lac}}}{R_{\mathrm{can}}} \right)^2 \eta(18 + 2\tilde{f}_{\mathrm{can}} - 18\bar{f}_{\mathrm{lac}} - 2\tilde{f}_{\mathrm{can}}\bar{f}_{\mathrm{lac}}) \Big)^{-1},\end{aligned} \tag{3.56}$$

with factor m defined as $m = \sqrt{\tilde{f}_{\mathrm{can}} / [\eta(9 + \tilde{f}_{\mathrm{can}})]}$.

Notably, as will be justified by respective computations in Section 4.1, it is reasonable to introduce the approximation $\frac{R_{\mathrm{lac}}}{R_{\mathrm{can}}} \to \infty$, in which case Eqs. (3.54) and (3.55) simplify to

$$\mathbf{A}_{\mathrm{lac}} = \frac{9\tilde{f}_{\mathrm{can}} R_{\mathrm{can}}^2}{3\tilde{f}_{\mathrm{can}}(\bar{f}_{\mathrm{lac}}+2)R_{\mathrm{can}}^2 - 2\eta(\tilde{f}_{\mathrm{can}}+9)(\bar{f}_{\mathrm{lac}}-1)R_{\mathrm{lac}}^2} \mathbf{1}\,, \tag{3.57}$$

and

$$\mathbf{A}_{\mathrm{exlac}} = \frac{1}{1 - f_{\mathrm{lac}}} \mathbf{1} \cdot \operatorname{grad} p_{\mathrm{exvas}}\,, \tag{3.58}$$

yielding, when inserting these two expressions into Eq. (3.49),

$$K_{\mathrm{exvas}}^{\mathrm{hom}} = \frac{R_{\mathrm{can}}^2 \tilde{f}_{\mathrm{can}}(1+2\bar{f}_{\mathrm{lac}})}{4\eta(9+\tilde{f}_{\mathrm{can}})(1-\bar{f}_{\mathrm{lac}})}\,. \tag{3.59}$$

Analogously to Eqs. (3.44) and (3.45), the pressure downscaling relations on the RVE of extralacunar bone material read as

$$\mathrm{grad}\, p_{\mathrm{lac}} = \mathbf{A}_{\mathrm{lac}} \cdot \mathrm{grad}\, p_{\mathrm{exvas}}\,, \tag{3.60}$$

and

$$\mathrm{grad}\, p_{\mathrm{exlac}} = \mathbf{A}_{\mathrm{exlac}} \cdot \mathrm{grad}\, p_{\mathrm{exvas}}\,. \tag{3.61}$$

3.3. Step III: From the vascular/extravascular scales to the macroscopic scale and vice versa

Finally, the last step deals with establishing mathematical relations between permeabilities and pressure gradients of the extravascular and vascular material, and the respective properties on the level of macroscopic bone tissue. As indicated in Section 2.3, two morphological situations, and their effects on the corresponding up- and downscaling relations, are studied.

On the one hand, the exact same morphological situation as in the first homogenization step, i.e. arbitrarily oriented, cylindrical (vascular) pores mutually interacting with spherically shaped, extravascular bone matrix, is considered – in the following, this morphology is referred to as "approach A". While the permeability of the former material phase, $\mathbf{k}_{\mathrm{vas}}$, is again based on equating the Poiseuille flow in the pores with a Darcy-type transport law, see Section 3.1, leading to

$$\mathbf{k}_{\mathrm{vas}} = \frac{R_{\mathrm{vas}}^2}{8\eta} \begin{pmatrix} 1 & 0 & 0 \\ 0 & 0 & 0 \\ 0 & 0 & 0 \end{pmatrix}_{\mathbf{e}_{\mathrm{s}},\mathbf{e}_{\mathrm{t}},\mathbf{e}_{\mathrm{u}}}\,, \tag{3.62}$$

with R_{vas} as the radius of the vascular pores, and η as the fluid dynamic permeability. The permeability of the extravascular bone material, $\mathbf{K}_{\mathrm{exvas}}^{\mathrm{hom}}$, is known from the second homogenization step, see Section 3.2, and in particular Eq. (3.59). Analogously to $\mathbf{K}_{\mathrm{exvas}}^{\mathrm{hom}}$, compare Section 3.2, the upscaled permeability on the RVE of macroscopic bone tissue,

$\mathbf{K}^{\mathrm{hom}}_{\mathrm{macro}}$, reads as

$$\mathbf{K}^{\mathrm{hom,\,A}}_{\mathrm{macro}} = f_{\mathrm{vas}} \int_{\varphi}^{2\pi} \int_{\vartheta}^{\pi} \mathbf{k}_{\mathrm{vas}}(\vartheta,\varphi) \cdot \mathbf{A}^{\mathrm{A}}_{\mathrm{vas}}(\vartheta,\varphi) \frac{\sin\vartheta}{4\pi} \mathrm{d}\vartheta \mathrm{d}\varphi + (1-f_{\mathrm{vas}}) \mathbf{K}^{\mathrm{hom}}_{\mathrm{exvas}} \cdot \mathbf{A}^{\mathrm{A}}_{\mathrm{exvas}}\,, \quad (3.63)$$

with the concentration tensors $\mathbf{A}^{\mathrm{A}}_{\mathrm{vas}}$ and $\mathbf{A}^{\mathrm{A}}_{\mathrm{exvas}}$ defined as

$$\begin{aligned} \mathbf{A}^{\mathrm{A}}_{\mathrm{vas}}(\vartheta,\varphi) = & \left[\mathbf{1} + \mathbf{P}^{\mathrm{A}}_{\mathrm{vas}}(\vartheta,\varphi) \cdot (\mathbf{k}_{\mathrm{vas}}(\vartheta,\varphi) - \mathbf{K}^{\mathrm{hom,\,A}}_{\mathrm{macro}})\right]^{-1} \cdot \\ & \left[f_{\mathrm{vas}} \int_{\varphi=0}^{2\pi} \int_{\vartheta=0}^{\pi} \frac{\sin\vartheta}{4\pi} [\mathbf{1} + \mathbf{P}^{\mathrm{A}}_{\mathrm{vas}}(\vartheta,\varphi) \cdot (\mathbf{k}_{\mathrm{vas}}(\vartheta,\varphi) - \mathbf{K}^{\mathrm{hom,\,A}}_{\mathrm{macro}})]^{-1} \mathrm{d}\vartheta \mathrm{d}\varphi \right. \\ & \left. + (1-f_{\mathrm{vas}}) \left[\mathbf{1} + \mathbf{P}^{\mathrm{A}}_{\mathrm{exvas}} \cdot (\mathbf{K}^{\mathrm{hom}}_{\mathrm{exvas}} - \mathbf{K}^{\mathrm{hom,\,A}}_{\mathrm{macro}})\right]^{-1} \right]^{-1}, \end{aligned} \quad (3.64)$$

and

$$\begin{aligned} \mathbf{A}^{\mathrm{A}}_{\mathrm{exvas}} = & \left[\mathbf{1} + \mathbf{P}^{\mathrm{A}}_{\mathrm{exvas}} \cdot (\mathbf{K}^{\mathrm{hom}}_{\mathrm{exvas}} - \mathbf{K}^{\mathrm{hom,\,A}}_{\mathrm{macro}})\right]^{-1} \cdot \\ & \left[f_{\mathrm{vas}} \int_{\varphi=0}^{2\pi} \int_{\vartheta=0}^{\pi} \frac{\sin\vartheta}{4\pi} [\mathbf{1} + \mathbf{P}^{\mathrm{A}}_{\mathrm{vas}}(\vartheta,\varphi) \cdot (\mathbf{k}_{\mathrm{vas}}(\vartheta,\varphi) - \mathbf{K}^{\mathrm{hom,\,A}}_{\mathrm{macro}})]^{-1} \mathrm{d}\vartheta \mathrm{d}\varphi + \right. \\ & \left. (1-f_{\mathrm{vas}}) \cdot \left[\mathbf{1} + \mathbf{P}^{\mathrm{A}}_{\mathrm{exvas}} \cdot (\mathbf{K}^{\mathrm{hom}}_{\mathrm{exvas}} - \mathbf{K}^{\mathrm{hom,\,A}}_{\mathrm{macro}})\right]^{-1} \right]^{-1}. \end{aligned} \quad (3.65)$$

$\mathbf{P}^{\mathrm{A}}_{\mathrm{vas}}(\vartheta,\varphi)$ and $\mathbf{P}^{\mathrm{A}}_{\mathrm{exvas}}$ in Eqs. (3.64) and (3.65) are the inhomogeneity tensors for cylindrical and spherical inclusions embedded in a matrix of permeability $\mathbf{K}^{\mathrm{hom,\,A}}_{\mathrm{macro}}$, defined analogously to Eqs. (3.32) and (3.37). Inserting these definitions of $\mathbf{P}^{\mathrm{A}}_{\mathrm{vas}}(\vartheta,\varphi)$ and $\mathbf{P}^{\mathrm{A}}_{\mathrm{exvas}}$, as well as the definition of $\mathbf{k}_{\mathrm{vas}}$ according to Eq. (3.62) into Eqs. (3.64) and (3.65) yields

$$\mathbf{A}^{\mathrm{A}}_{\mathrm{vas}}(\vartheta,\varphi) = \begin{pmatrix} A^{\mathrm{A}}_{\mathrm{vas,\,11}}(\vartheta,\varphi) & A^{\mathrm{A}}_{\mathrm{vas,\,12}}(\vartheta,\varphi) & A^{\mathrm{A}}_{\mathrm{vas,\,13}}(\vartheta,\varphi) \\ A^{\mathrm{A}}_{\mathrm{vas,\,21}}(\vartheta,\varphi) & A^{\mathrm{A}}_{\mathrm{vas,\,22}}(\vartheta,\varphi) & A^{\mathrm{A}}_{\mathrm{vas,\,23}}(\vartheta,\varphi) \\ A^{\mathrm{A}}_{\mathrm{vas,\,31}}(\vartheta,\varphi) & A^{\mathrm{A}}_{\mathrm{vas,\,32}}(\vartheta,\varphi) & A^{\mathrm{A}}_{\mathrm{vas,\,33}}(\vartheta,\varphi) \end{pmatrix}, \quad (3.66)$$

with the components of $\mathbf{A}^{\mathrm{A}}_{\mathrm{vas}}(\vartheta,\varphi)$ following as

$$\begin{aligned}
A^{\mathrm{A}}_{\mathrm{vas},\,11}(\vartheta,\varphi) =& \Big(\left(-6\cos^2\varphi\cos(2\vartheta)+3\cos(2\varphi)-21\right)(\tilde{f}_{\mathrm{can}}(2\bar{f}_{\mathrm{lac}}+1)\times \\
& \left(4f_{\mathrm{vas}}-9\right)R^2_{\mathrm{can}}+(\tilde{f}_{\mathrm{can}}+9)(\bar{f}_{\mathrm{lac}}-1)f_{\mathrm{vas}}R^2_{\mathrm{vas}}\Big)\Big/ \\
& \Big(2(\tilde{f}_{\mathrm{can}}+9)(\bar{f}_{\mathrm{lac}}-1)(f^2_{\mathrm{vas}}+9f_{\mathrm{vas}})R^2_{\mathrm{vas}}- \\
& 4\tilde{f}_{\mathrm{can}}(2\bar{f}_{\mathrm{lac}}+1)(7f_{\mathrm{vas}}-9f_{\mathrm{vas}})+27)R^2_{\mathrm{can}}\Big),
\end{aligned} \tag{3.67}$$

$$\begin{aligned}
A^{\mathrm{A}}_{\mathrm{vas},\,12}(\vartheta,\varphi) =& A^{\mathrm{A}}_{\mathrm{vas},\,21}(\vartheta,\varphi) \\
=& \Big(3\sin^2\vartheta\sin(2\varphi)(\tilde{f}_{\mathrm{can}}(2\bar{f}_{\mathrm{lac}}+1)\times \\
& \left(4f_{\mathrm{vas}}-9\right)R^2_{\mathrm{can}}+(\tilde{f}_{\mathrm{can}}+9)(\bar{f}_{\mathrm{lac}}-1)f_{\mathrm{vas}}R^2_{\mathrm{vas}}\Big)\Big/ \\
& \Big((\tilde{f}_{\mathrm{can}}+9)(\bar{f}_{\mathrm{lac}}-1)(f^2_{\mathrm{vas}}+9f_{\mathrm{vas}})R^2_{\mathrm{vas}}- \\
& 2\tilde{f}_{\mathrm{can}}(2\bar{f}_{\mathrm{lac}}+1)(7f^2_{\mathrm{vas}}-9f_{\mathrm{vas}})+27)R^2_{\mathrm{can}}\Big),
\end{aligned} \tag{3.68}$$

$$\begin{aligned}
A^{\mathrm{A}}_{\mathrm{vas},\,13}(\vartheta,\varphi) =& A^{\mathrm{A}}_{\mathrm{vas},\,31}(\vartheta,\varphi) \\
=& \Big(3\sin(2\vartheta)\cos(\varphi)(\tilde{f}_{\mathrm{can}}(2\bar{f}_{\mathrm{lac}}+1)\times \\
& \left(4f_{\mathrm{vas}}-9\right)R^2_{\mathrm{can}}+(\tilde{f}_{\mathrm{can}}+9)(\bar{f}_{\mathrm{lac}}-1)f_{\mathrm{vas}}R^2_{\mathrm{vas}}\Big)\Big/ \\
& \Big((\tilde{f}_{\mathrm{can}}+9)(\bar{f}_{\mathrm{lac}}-1)(f^2_{\mathrm{vas}}+9f_{\mathrm{vas}})R^2_{\mathrm{vas}}- \\
& 2\tilde{f}_{\mathrm{can}}(2\bar{f}_{\mathrm{lac}}+1)(7f^2_{\mathrm{vas}}-9f_{\mathrm{vas}})+27)R^2_{\mathrm{can}}\Big),
\end{aligned} \tag{3.69}$$

$$\begin{aligned}
A^{\mathrm{A}}_{\mathrm{vas},\,22}(\vartheta,\varphi) =& \Big(\left(6\sin^2\varphi\cos(2\vartheta)+3\cos(2\varphi)+21\right)(\tilde{f}_{\mathrm{can}}(2\bar{f}_{\mathrm{lac}}+1)\times \\
& \left(4f_{\mathrm{vas}}-9\right)R^2_{\mathrm{can}}+(\tilde{f}_{\mathrm{can}}+9)(\bar{f}_{\mathrm{lac}}-1)f_{\mathrm{vas}}R^2_{\mathrm{vas}}\Big)\Big/ \\
& \Big(2(\tilde{f}_{\mathrm{can}}+9)(\bar{f}_{\mathrm{lac}}-1)(f^2_{\mathrm{vas}}+9f_{\mathrm{vas}})R^2_{\mathrm{vas}}- \\
& 4\tilde{f}_{\mathrm{can}}(2\bar{f}_{\mathrm{lac}}+1)(7f^2_{\mathrm{vas}}-9f_{\mathrm{vas}})R^2_{\mathrm{can}}\Big),
\end{aligned} \tag{3.70}$$

$$\begin{aligned}
A^{\mathrm{A}}_{\mathrm{vas},\,23}(\vartheta,\varphi) =& A^{\mathrm{A}}_{\mathrm{vas},\,32}(\vartheta,\varphi) \\
=& \Big(3\sin(2\vartheta)\sin(\varphi)(\tilde{f}_{\mathrm{can}}(2\bar{f}_{\mathrm{lac}}+1)\times \\
& \left(4f_{\mathrm{vas}}-9\right)R^2_{\mathrm{can}}+(\tilde{f}_{\mathrm{can}}+9)(\bar{f}_{\mathrm{lac}}-1)f_{\mathrm{vas}}R^2_{\mathrm{vas}}\Big)\Big/ \\
& \Big((\tilde{f}_{\mathrm{can}}+9)(\bar{f}_{\mathrm{lac}}-1)(f^2_{\mathrm{vas}}+9f_{\mathrm{vas}})R^2_{\mathrm{vas}}- \\
& 2\tilde{f}_{\mathrm{can}}(2\bar{f}_{\mathrm{lac}}+1)(7f^2_{\mathrm{vas}}-9f_{\mathrm{vas}})+27)R^2_{\mathrm{can}}\Big),
\end{aligned} \tag{3.71}$$

and

$$
\begin{aligned}
A^{\mathrm{A}}_{\mathrm{vas},\,33}(\vartheta,\varphi) = &\Big((-9+3\cos(2\vartheta))\,(\tilde{f}_{\mathrm{can}}(2\bar{f}_{\mathrm{lac}}+1)(4f_{\mathrm{vas}}-9)R^2_{\mathrm{can}} + \\
&(\tilde{f}_{\mathrm{can}}+9)(\bar{f}_{\mathrm{lac}}-1)f_{\mathrm{vas}}R^2_{\mathrm{vas}}\Big) \Big/ \\
&\Big((\tilde{f}_{\mathrm{can}}+9)(\bar{f}_{\mathrm{lac}}-1)(f^2_{\mathrm{vas}}+9f_{\mathrm{vas}})R^2_{\mathrm{vas}} - \\
&2\tilde{f}_{\mathrm{can}}(2\bar{f}_{\mathrm{lac}}+1)(7f^2_{\mathrm{vas}}-9f_{\mathrm{vas}})+27)R^2_{\mathrm{can}}\Big)\,,
\end{aligned}
\tag{3.72}
$$

as well as

$$
\begin{aligned}
\mathbf{A}^{\mathrm{A}}_{\mathrm{exvas}} = &-\Big(9\left(6\tilde{f}_{\mathrm{can}}(2\bar{f}_{\mathrm{lac}}+1)(f_{\mathrm{vas}}-1)R^2_{\mathrm{can}} + (\tilde{f}_{\mathrm{can}}+9)(\bar{f}_{\mathrm{lac}}-1)f_{\mathrm{vas}}R^2_{\mathrm{vas}}\right)\Big) \Big/ \\
&\Big(2\tilde{f}_{\mathrm{can}}(2\bar{f}_{\mathrm{lac}}+1)(f_{\mathrm{vas}}(7f_{\mathrm{vas}}-9)+27)R^2_{\mathrm{can}} - \\
&(\tilde{f}_{\mathrm{can}}+9)(\bar{f}_{\mathrm{lac}}-1)f_{\mathrm{vas}}(f_{\mathrm{vas}}+9)R^2_{\mathrm{vas}}\Big)\mathbf{1}\,.
\end{aligned}
\tag{3.73}
$$

Inserting furthermore the definitions of $\mathbf{A}^{\mathrm{A}}_{\mathrm{vas}}(\vartheta,\varphi)$ and $\mathbf{A}^{\mathrm{A}}_{\mathrm{exvas}}$ according to Eqs. (3.66) – (3.73) into Eq. (3.63) yields the following expression for $\mathbf{K}^{\mathrm{hom,\,A}}_{\mathrm{macro}}$:

$$
\begin{aligned}
\mathbf{K}^{\mathrm{hom,\,A}}_{\mathrm{macro}} = &\Bigg(\frac{54\tilde{f}^2_{\mathrm{can}}(2\bar{f}_{\mathrm{lac}}+1)^2(f_{\mathrm{vas}}-1)^2R^4_{\mathrm{can}}}{(\tilde{f}_{\mathrm{can}}+9)(\bar{f}_{\mathrm{lac}}-1)} + (\tilde{f}_{\mathrm{can}}+9)(\bar{f}_{\mathrm{lac}}-1)f^2_{\mathrm{vas}}R^4_{\mathrm{vas}} + \\
&\tilde{f}_{\mathrm{can}}(2\bar{f}_{\mathrm{lac}}+1)(13f^2_{\mathrm{vas}}-18f_{\mathrm{vas}})R^2_{\mathrm{can}}R^2_{\mathrm{vas}}\Bigg) / \\
&\Bigg(4\eta(\tilde{f}_{\mathrm{can}}+9)(\bar{f}_{\mathrm{lac}}-1)(f^2_{\mathrm{vas}}+9f_{\mathrm{vas}})R^2_{\mathrm{vas}} - \\
&8\eta\tilde{f}_{\mathrm{can}}(2\bar{f}_{\mathrm{lac}}+1)(7f^2_{\mathrm{vas}}-9f_{\mathrm{vas}}+27)R^2_{\mathrm{can}}\Bigg)\mathbf{1}\,.
\end{aligned}
\tag{3.74}
$$

Furthermore, two pressure downscaling relations are obtained; one relating the macroscopic pressure gradient to the pressure gradient in the vascular pores,

$$
\operatorname{grad} p^{\mathrm{A}}_{\mathrm{vas}} = \mathbf{A}^{\mathrm{A}}_{\mathrm{vas}}(\vartheta,\varphi)\cdot\operatorname{grad} p_{\mathrm{macro}}\,,
\tag{3.75}
$$

and one relating the macroscopic pressure gradient to the pressure gradient arriving in the extravascular bone material,

$$
\operatorname{grad} p^{\mathrm{A}}_{\mathrm{exvas}} = \mathbf{A}^{\mathrm{A}}_{\mathrm{exvas}}\cdot\operatorname{grad} p_{\mathrm{macro}}\,.
\tag{3.76}
$$

On the other hand, the second morphological scenario considered in this work comprises vascular pores oriented in the direction of the main anatomical axis as it occurs in long bones, with the extravascular bone material acting as a matrix phase hosting the pores in form of inclusions, see Section 2.3 – in the following this morphology is referred to as "approach B". The corresponding homogenized macroscopic permeability tensor reads as

$$\mathbf{K}_{\text{macro}}^{\text{hom,B}} = f_{\text{vas}}\mathbf{k}_{\text{vas}} \cdot \mathbf{A}_{\text{vas}}^{\text{B}} + (1 - f_{\text{vas}})\mathbf{K}_{\text{exvas}}^{\text{hom}} \cdot \mathbf{A}_{\text{exvas}}^{\text{B}}\,, \tag{3.77}$$

with the pressure gradient concentration tensors $\mathbf{A}_{\text{vas}}^{\text{B}}$ and $\mathbf{A}_{\text{exvas}}^{\text{B}}$ defined as

$$\begin{aligned}\mathbf{A}_{\text{vas}}^{\text{B}} =& \big(\mathbf{1} + \mathbf{P}_{\text{vas}}^{\text{B}} \cdot (\mathbf{k}_{\text{vas}} - \mathbf{K}_{\text{exvas}}^{\text{hom}})\big)^{-1} \times \\ & \big[f_{\text{vas}}\big(\mathbf{1} + \mathbf{P}_{\text{vas}}^{\text{B}} \cdot (\mathbf{k}_{\text{vas}} - \mathbf{K}_{\text{exvas}}^{\text{hom}})\big)^{-1} + (1 - f_{\text{vas}}) \cdot \mathbf{1}\big]^{-1}\,,\end{aligned} \tag{3.78}$$

and

$$\mathbf{A}_{\text{exvas}}^{\text{B}} = \big[f_{\text{vas}}\big(\mathbf{1} + \mathbf{P}_{\text{vas}}^{\text{B}} \cdot (\mathbf{k}_{\text{vas}} - \mathbf{K}_{\text{exvas}}^{\text{hom}})\big)^{-1} + (1 - f_{\text{vas}}) \cdot \mathbf{1}\big]^{-1}\,, \tag{3.79}$$

where $\mathbf{P}_{\text{vas}}^{\text{B}}$ is the inhomogeneity tensor of a cylindrical inclusion, embedded in a matrix of permeability $\mathbf{K}_{\text{exvas}}^{\text{hom}}$, see Eq. (3.32). Considering the latter definition, as well as $\mathbf{k}_{\text{vas}}$ according to Eq. (3.62), and $\mathbf{K}_{\text{exvas}}^{\text{hom}}$ according to Eq. (3.59), in Eqs. (3.78) and (3.79), yields

$$\mathbf{A}_{\text{vas}}^{\text{B}} = \begin{pmatrix} 1 & 0 & 0 \\ 0 & \frac{2}{f_{\text{vas}}+1} & 0 \\ 0 & 0 & \frac{2}{f_{\text{vas}}+1} \end{pmatrix}, \tag{3.80}$$

and

$$\mathbf{A}_{\text{exvas}}^{\text{B}} = \begin{pmatrix} 1 & 0 & 0 \\ 0 & \frac{1}{f_{\text{vas}}+1} & 0 \\ 0 & 0 & \frac{1}{f_{\text{vas}}+1} \end{pmatrix}. \tag{3.81}$$

Insertion of these definitions of $\mathbf{A}_{\text{vas}}^{\text{B}}$ and $\mathbf{A}_{\text{exvas}}^{\text{B}}$ into Eq. (3.77) gives access to the permeability tensor of macroscopic homogenized bone tissue,

$$\mathbf{K}_{\text{macro}}^{\text{hom, B}} = K_{\text{macro, l}}^{\text{hom, B}}\mathbf{e}_{\text{s}} \otimes \mathbf{e}_{\text{s}} + K_{\text{macro, t}}^{\text{hom, B}}\mathbf{e}_{\text{t}} \otimes \mathbf{e}_{\text{t}} + K_{\text{macro, t}}^{\text{hom, B}}\,, \mathbf{e}_{\text{u}} \otimes \mathbf{e}_{\text{u}} \tag{3.82}$$

with the longitudinal permeability, $K_{\text{macro, l}}^{\text{hom, B}}$, reading as

$$K_{\text{macro, l}}^{\text{hom, B}} = \frac{2\tilde{f}_{\text{can}}R_{\text{can}}^2(2\bar{f}_{\text{lac}}+1)(f_{\text{vas}}-1) + f_{\text{vas}}R_{\text{vas}}^2(9+\tilde{f}_{\text{can}})(\bar{f}_{\text{lac}}-1)}{8\eta(9+\tilde{f}_{\text{can}})(\bar{f}_{\text{lac}}-1)}\,, \tag{3.83}$$

and with the permeability in transverse direction, $K^{\text{hom, B}}_{\text{macro, t}}$, reading as

$$K^{\text{hom, B}}_{\text{macro, t}} = \frac{\tilde{f}_{\text{can}} R^2_{\text{can}} (2\bar{f}_{\text{lac}} + 1)(f_{\text{vas}} - 1)}{(36\eta + 4\eta\tilde{f}_{\text{can}})(\bar{f}_{\text{lac}} - 1)(f_{\text{vas}} + 1)} \,. \tag{3.84}$$

The respective downscaling relations for the pressure gradients follow as

$$\operatorname{grad} p^{\text{B}}_{\text{vas}} = \mathbf{A}^{\text{B}}_{\text{vas}} \cdot \operatorname{grad} p_{\text{macro}} \,, \tag{3.85}$$

and

$$\operatorname{grad} p^{\text{B}}_{\text{exvas}} = \mathbf{A}^{\text{B}}_{\text{exvas}} \cdot \operatorname{grad} p_{\text{macro}} \,. \tag{3.86}$$

4. Model evaluation

This section is devoted to presenting how the multiscale model presented in Section 3 can be numerically evaluated. First, the focus is on permeability upscaling, from the level of single canaliculi to the level of macroscopic bone tissue, see Section 4.1. Then, it is shown how the same model can be used to also downscale macroscopically applied pressure gradients to the scale of canalicular pores, see Section 4.2.

For the subsequently presented simulations, physiologically reasonable ranges of bone porosities on all covered hierarchical levels have been considered. While the hence relevant canalicular, lacunar, and vascular porosities have already been discussed thoroughly in Section 2.1, see Tables 2.1, 2.3, and 2.6, the aforementioned ranges are, for the sake of clarity, briefly summarized below:

- The canalicular porosity, f_{can}, has been identified to amount to 0.007 in murine mid-diaphysial femurs, based on focused ion beam scanning electron microscopy (Schneider et al., 2011); to 0.02 in the human mandible, based on synchrotron radiation nano-computed tomography scanning (Hesse et al., 2015); and to 0.03 in the human diaphysial femur, based on micro-computed tomography scanning (Benalla et al., 2013). However, it must be taken into account that the model requires $\tilde{f}_{\text{can}}$ as input, i.e. the canalicular porosities quantified on the RVE of extralacunar bone material, see Eq. (3.21). For example, when considering an average lacunar porosity of $\bar{f}_{\text{lac}} = 0.059$, and an average vascular porosity of $f_{\text{vas}} = 0.075$, $f_{\text{can}} = 0.007$ relates to $\tilde{f}_{\text{can}} = 0.008$. In the following, a canalicular porosity range of $[0.005, 0.03]$ is considered for f_{can}, see Table 2.6.

- The lacunar porosity, f_{lac}, has been evaluated to be 0.013 for the murine femoral mid-diaphysis (Schneider et al., 2007), around 0.02 for the human femoral mid-diaphysis (Benalla et al., 2013), and 0.015 for rat diaphysial bone (Tommasini et al., 2012; Palacio–Mancheno et al., 2014) by means of μCT, especially utilizing synchrotron-radiation (SR-μCT) (Hesse et al., 2014a,b). In other studies, however, such as by Tai et al. (2008), much higher porosities of around 0.09 were measured, utilizing scanning electron microscopy in back-scattered mode on murine bone, see

Table 2.3. Considering, as explained above, the difference between f_{lac} and $\bar{f}_{\mathrm{lac}}$ (i.e. the lacunar porosity quantified on the RVE of macroscopic tissue and on the RVE of extravascular material respectively), see Eq. (3.50), the lacunar porosity range in the following, is $[0.01, 0.1]$ for f_{lac}.

- The vascular porosity, f_{vas}, has been identified to amount to 0.06 – 0.09 in the human femoral mid-diaphysis by means of computed tomography and microradiography (Bousson et al., 2000, 2001; Cooper et al., 2003, 2007), to 0.06 – 0.07 by means of digitalized virtual microscopy also measured in the human femur (Feik et al., 1997; Stein et al., 1999), and to 0.01 – 0.05 in murine bone by means of synchrotron radiation micro-computed tomography (Schneider et al., 2007, 2009), see Table 2.1. Thus, a porosity range of $[0.05, 0.1]$ is considered for f_{vas} in the following.

Furthermore, the up- and downscaling relations derived in Section 3 explicitly contain the vascular and canalicular radii. Referring to Tables 2.2 and 2.5, the following ranges are considered as physiologically reasonable:

- Based on scanning electron microscopy and transmission electron microscopy (Marotti, 1990; You et al., 2004), canalicular diameters of 150 to 400 nm have been identified, while atomic force microscopy has suggested a range of 400 to 500 nm (Lin and Xu, 2011), see Table 2.5. Hence, in the following, a canalicular diameter range of $[150, 500]$ nm is considered.

- By means of μCT, vascular radii of 5 – 7 μm were measured for rodent bones on the one hand, while values of 35 – 80 μm (Martin et al., 1998; Renders et al., 2007; Goulet et al., 2008) were found for human bones on the other hand. Accordingly, a range of $[10, 80]$ μm is considered for d_{vas}.

Additionally, the derived mathematical (upscaling and downscaling) relations are governed by the dynamic viscosity of the pore fluid, η, see for example Eqs. (3.43), (3.59), (3.60), (3.74), (3.83), and (3.84). It is well known that the dynamic viscosity of bulk water amounts to $\eta_{\mathrm{bulkwater}} = 0.001$ Pa s – this value has been used frequently in both experimental and theoretical studies, related to the movement of fluid in the lacunar-canalicular pore system of bone (Gururaja et al., 2005; Weinbaum et al., 1994; Gardinier et al., 2010). However, it should be noted that water is a polarized fluid, and as such changes its transport behavior when adjacent to electrically charged surfaces (such as the hydroxyapatite crystals, building up extracanalicular bone material). In fact, so-called

structured, or ice-type water (of "liquid crystalline" nature) forms, leading to a higher viscosity and a lower diffusivity in the affected regions, referred to as "surface zone" (Henniker, 1949), or "exclusion zone" (Pollack, 2013), must be considered as compared to the undisturbed bulk state. The thickness of this zone ranges from some hundred micrometers up to a few millimetres (Ichikawa et al., 2002; Pivonka et al., 2004), as evidenced by several different experimental modalities, see Abdalrahman et al. (2015) for a brief overview. Moreover, Ichikawa et al. (2000, 2002) quantified by means of molecular dynamics studies (on water molecules which are surrounded by clay-type mineral surfaces) that the viscosity in structured water increases on average by a factor of approximately 7. Hence, given that the pore fluid in bone tissue is quite similar to water, it is assumed that the dynamic viscosity of the fluid contained in all considered pore spaces amounts to $\eta_{\text{bonepores}} = 7\,\eta_{\text{bulkwater}} = 0.007$ Pa s.

4.1. Permeability upscaling

4.1.1. Extralacunar permeability

Evaluating Eq. (3.43) for varying underlying parameters shows how $K^{\text{hom}}_{\text{exlac}}$ is quantitatively influenced by them. First, the canalicular porosity f_{can} and the canalicular radius R_{can} are held constant, at $f_{\text{can}} = 0.02$ and $R_{\text{can}} = 100\,\text{nm}$, while the pore fluid viscosity is varied between 0.001 Pa s (which is the viscosity of bulk water) and 0.01 Pa s(related, for example, to the effect of water layering). It turns out that this tenfold increase of the viscosity leads, as expected, to a corresponding reduction of the extralacunar permeability $K^{\text{hom}}_{\text{exlac}}$ by factor 10, from $K^{\text{hom}}_{\text{exlac}} = 6.3 \times 10^{-15}$ m^2/ (Pa s) for $\eta = 0.001$ Pa s to $K^{\text{hom}}_{\text{exlac}} = 6.3 \times 10^{-16}$ m^2/ (Pa s) for $\eta = 0.01$ Pa s, see Figure 4.1(a).

In a second study, the pore fluid viscosity is held constant at $\eta = 0.007$ Pa s, while f_{can} is varied between 0.005 and 0.03, and R_{can} between 75 and 250 nm, in order to elucidate how $K^{\text{hom}}_{\text{exlac}}$ changes within the experimentally relevant, physiologically meaningful range of f_{can} and R_{can}. Within this considered range, $K^{\text{hom}}_{\text{exlac}}$ apparently increases not quite, but almost linearly with increasing f_{can}, while increasing R_{can} leads to an exponential increase of $K^{\text{hom}}_{\text{exlac}}$, see Figure 4.1(b).

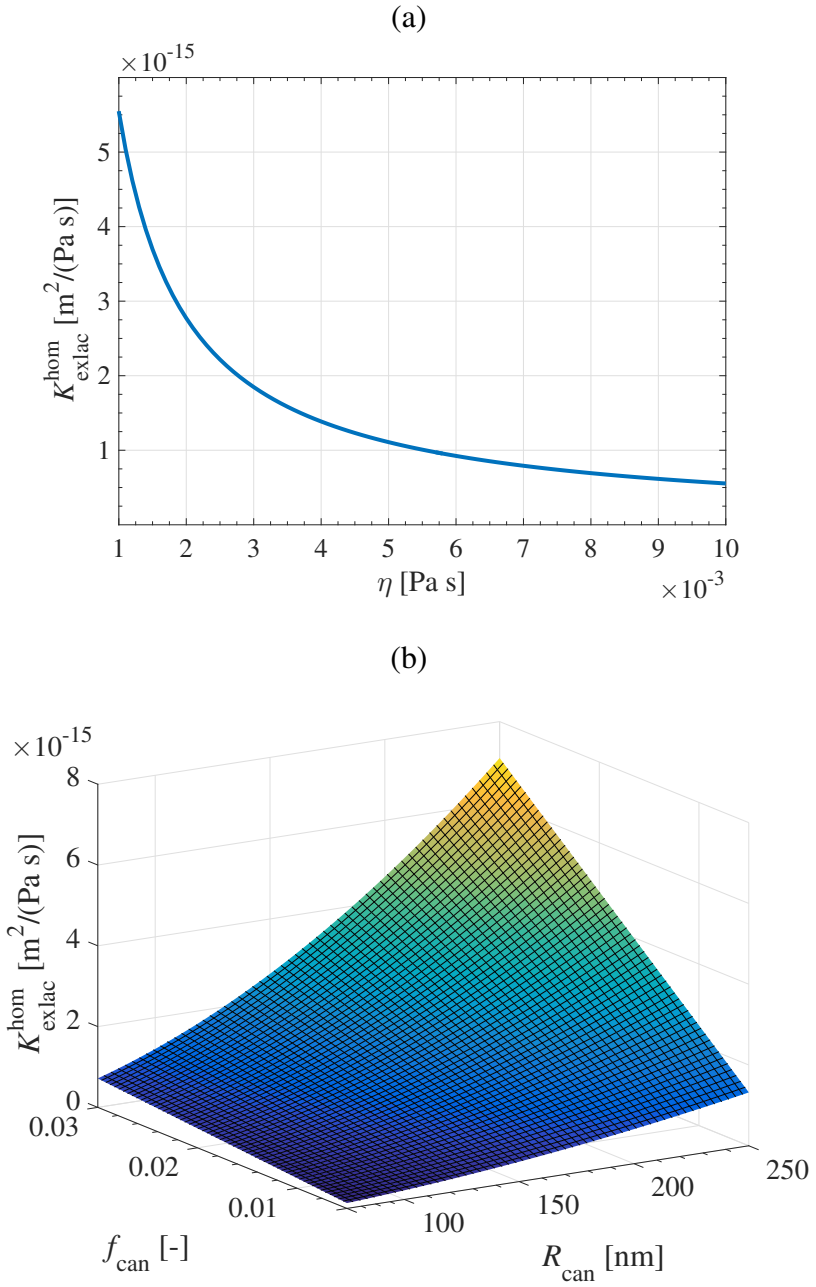

Figure 4.1.: (a) Effect of varying pore fluid viscosity on the extralacunar permeability $K^{\text{hom}}_{\text{exlac}}$ (while considering $f_{\text{can}} = 0.02$ and $R_{\text{can}} = 100$ nm); (b) the dependence of $K^{\text{hom}}_{\text{exlac}}$ on the canalicular porosity f_{can} and radius R_{can} (while considering $\eta = 0.007$ Pa s)

4.1.2. Extravascular permeability

The mathematical expression derived for homogenizing the permeability on the level of extravascular bone material, i.e. Eq. (3.56), contains the semi-empirical coefficient λ, $0 \leq \lambda \leq 5$, see Section 3.2. Before studying the influence of other parameters, the impor-

tance of λ in the present context is first elucidated. For that purpose, Eq. (3.56) is numerically evaluated, thereby considering $f_{\text{can}} = 0.02$, $f_{\text{lac}} = 0.1$, $R_{\text{can}} = 100\,\text{nm}$, $R_{\text{lac}} = 5\,\mu\text{m}$, and $\eta = 0.007$ Pa s, see Figure 4.2. Obviously, within the relevant λ-range, the influence of λ on $K^{\text{hom}}_{\text{exvas}}$ is negligible – increasing λ from 0 to 5 implies an increase of $K^{\text{hom}}_{\text{exvas}}$ by only 2.43%. Furthermore, it has been argued in Section 3.2 that λ can be eliminated from the permeability relation if $R_{\text{lac}} >> R_{\text{can}}$, or, in other words, if $\frac{R_{\text{lac}}}{R_{\text{can}}} \to \infty$, eventually leading to Eq. (3.59). In the following, this simplifying assumption is corroborated. In particular, Eq. (3.56) is evaluated for $\frac{R_{\text{lac}}}{R_{\text{can}}} \in [5,\, 10^3]$ and for $\lambda \in [0,\, 5]$, while considering $f_{\text{can}} = 0.02$, $f_{\text{lac}} = 0.1$, and $\eta = 0.007$ Pa s. The results of this analysis unambiguously show that for ratios $\frac{R_{\text{lac}}}{R_{\text{can}}}$ in the physiologically relevant range, i.e. between $[10^1,\, 10^2]$, the influence of this ratio on $K^{\text{hom}}_{\text{exvas}}$ is negligible, hence setting $\frac{R_{\text{lac}}}{R_{\text{can}}} \to \infty$ in Eq. (3.56) is justified, see Figure 4.3. The latter conclusion has also been confirmed in the work of Markov et al. (2009), who could show that for setting $\frac{R_{\text{lac}}}{R_{\text{can}}} \to \infty$ the condition $R_{\text{lac}} >> \sqrt{K^{\text{hom}}_{\text{exlac}}}$ must be satisfied – this is actually the case for the RVE of extravascular bone material.

Hence, for further analysis of $K^{\text{hom}}_{\text{exvas}}$, Eq. (3.59) is utlized. According to this equation, $K^{\text{hom}}_{\text{exlac}}$ is governed by the porosities f_{can} and f_{vas}, by the canalicular radius R_{can}, as well as by the pore fluid viscosity. While the latter is held constant at $\eta = 0.007$ Pa s, the first study related to the behavior of $K^{\text{hom}}_{\text{exlac}}$ comprises varying porosities, between $f_{\text{can}} \in [0.005,\, 0.03]$ and $f_{\text{lac}} \in [0.01,\, 0.1]$, revealing that within the studied porosity ranges, $K^{\text{hom}}_{\text{exlac}}$ increases with increasing porosities almost linearly, see Figure 4.4(a). Increasing the porosities, beyond experimentally motivated upper limits, would show that the dependencies of $K^{\text{hom}}_{\text{exlac}}$ on f_{can} and f_{lac} are actually non-linear (not shown here).

Furthermore, the structure of Eq. (3.59) readily suggests that R_{can} has a major influence on $K^{\text{hom}}_{\text{exvas}}$. This dependence is illustrated by varying R_{can} between $[75,\, 250]\,\text{nm}$, while considering $f_{\text{can}} = 0.02$ and $f_{\text{lac}} = 0.1$, see Figure 4.4(b).

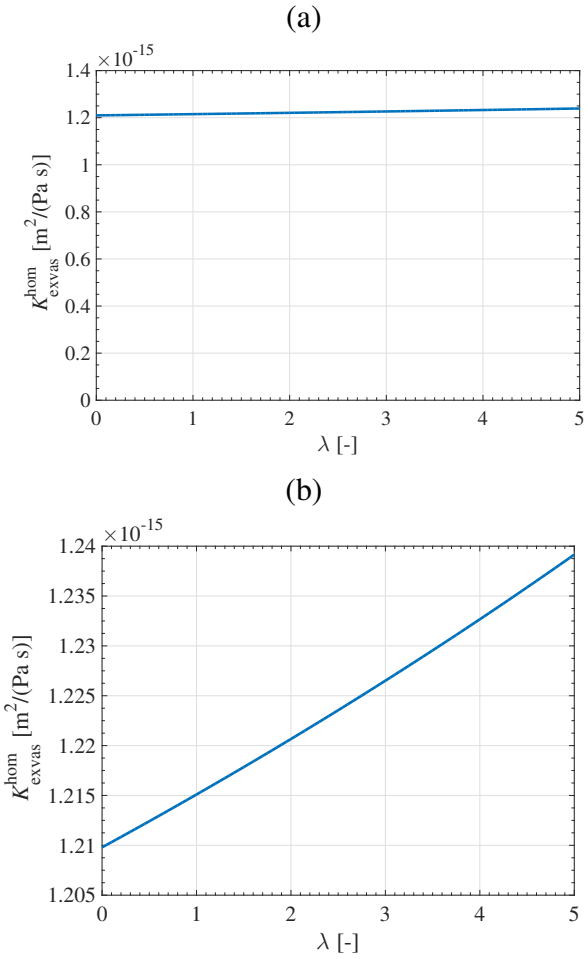

Figure 4.2.: Influence of λ on the homogenized extravascular permeability $K^{\text{hom}}_{\text{exvas}}$, for λ within a range of 0 to 5 (while considering $f_{\text{can}} = 0.02$, $f_{\text{lac}} = 0.1$, $R_{\text{can}} = 100$ nm, $R_{\text{lac}} = 5\,\mu$m, $\eta = 0.007$ Pa s)

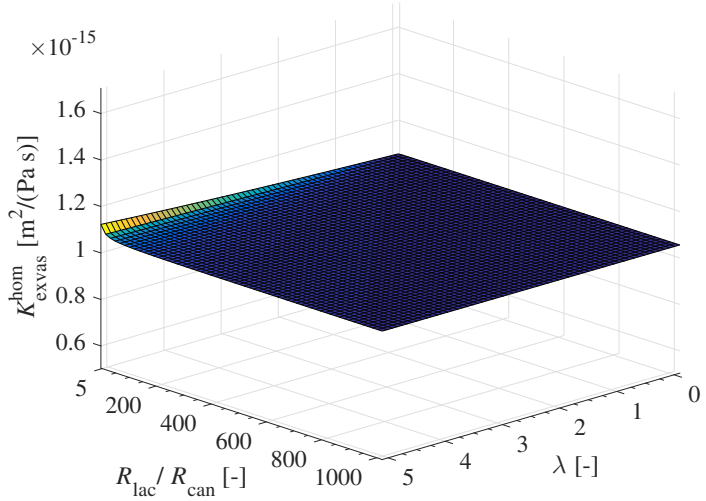

Figure 4.3.: Dependence of the homogenized extravascular permeability $K^{\text{hom}}_{\text{exvas}}$ on the ratio of the lacunar and canalicular pore radii, $\frac{R_{\text{lac}}}{R_{\text{can}}}$, and on the slip coefficient λ (while considering f_{can} = 0.02, f_{lac} = 0.1, and $\eta = 0.007$ Pa s)

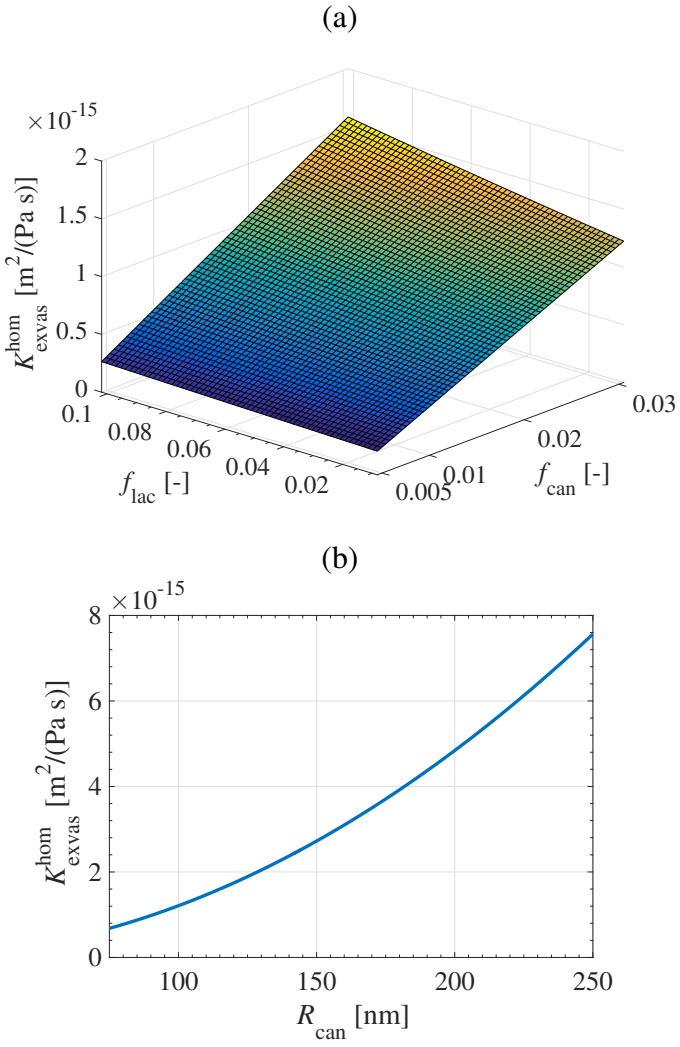

Figure 4.4.: Dependence of the homogenized extravascular permeability $K^{\text{hom}}_{\text{exvas}}$ on (a) the porosities f_{can} and f_{lac} (while considering $R_{\text{can}} = 100$ nm, and $\eta = 0.007$ Pa s), and on (b) the canalicular radius R_{can} (while considering $f_{\text{can}} = 0.02$, $f_{\text{lac}} = 0.1$, and $\eta = 0.007$ Pa s)

As for validation of the obtained extravascular permeabilities, corresponding values from literature are considered, see Table 4.1. In these studies, the porosity was consistently derived in intrinsic format. Hence, the homogenized, Darcy-type permeability, resulting from Eq. (3.59) must be multiplied by the pore fluid viscosity, $\kappa^{\text{hom}}_{\text{exvas}} = K^{\text{hom}}_{\text{exvas}} \cdot \eta$. The such obtained intrinsic permeabilities agree well with the range given in the studies summarized in Table 4.1. It is however striking that the results of the present study are actually on the higher end of the range of the permeabilities given in Table 4.1. The reason for this is that in the present study the cell processes contained in the canaliculi are neglected, as opposed to some of the considered works, e.g. (Weinbaum et al., 1994; Zhang et al., 1998; Smit et al., 2002; Beno et al., 2006; Lemaire et al., 2008), who do take this effect into account.

Table 4.1.: Values for the extravascular intrinsic permeability, based on combinations of experimental data and theoretical analysis

Reference	κ_{exvas} [m^2]	Method	Direction
Gururaja et al. (2005)	6.7×10^{-18}	FE of lacunar flow, adapted from Weinbaum et al. (1994), without cell process	Axial
Gururaja et al. (2005)	7.5×10^{-18}	FE of lacunar flow, adapted from Weinbaum et al. (1994), with cell process	Axial
Gururaja et al. (2005)	6.7×10^{-21}	FE of lacunar flow, adapted from Weinbaum et al. (1994), with+without cell process	Radial
Weinbaum et al. (1994)	$10^{-22} - 10^{-19}$	Ultrastructure model with cell process	
Beno et al. (2006)	$10^{-22} - 10^{-19}$	FE with µstructure measurements, adapted from Weinbaum et al. (1994)	Radial
Lemaire et al. (2008)	5.9×10^{-18} -2×10^{-17}	Adapted from Weinbaum et al. (1994)	
Gailani et al. (2009)	5×10^{-25} -8×10^{-24}	Poroelastic model and stress-relaxation testing on bovine bone	
Gardinier et al. (2010)	2.8×10^{-23}	Rapid compaction of canine bone and recording of intramedullary pressure	

Interestingly, the homogenized permeability of extravascular bone material, $K^{\text{hom}}_{\text{exvas}}$, see Eq. (3.59), is exactly the same as the effective permeability found by Markov et al. (2009) for a porous medium with spherical inclusions by utilizing the Maxwell-Garnett equation which was originally derived for the electromagnetic behavior of a double-porous medium (Garnett, 1904), according to following equation:

$$K^{\text{hom}}_{\text{exvas}} = K^{\text{hom}}_{\text{exlac}} \frac{2K^{\text{hom}}_{\text{exlac}} + k_{\text{lac}} + 2\bar{f}_{\text{lac}}(k_{\text{lac}} - K^{\text{hom}}_{\text{exlac}})}{2K^{\text{hom}}_{\text{exlac}} + k_{\text{lac}} - 2\bar{f}_{\text{lac}}(k_{\text{lac}} - K_{\text{exlac}})}. \tag{4.1}$$

Inserting $K^{\text{hom}}_{\text{exlac}}$ according to Eqs. (3.43) and k_{lac} according to (3.47) would yield Eq. (3.56).

4.1.3. Macroscopic permeability

As for the RVE of macroscopic bone tissue, two morphological concepts are pursued in this work. Eq. (3.74) relates to approach A, defining the isotropic permeability due to arbitrarily oriented, interpenetrating vascular pores, while Eq. (3.83) and (3.84), defining

the longitudinal and transversal components of the macroscopic permeability tensor, relate to approach B, representing vascular pores oriented predominantly along the main anatomical axis of long bones. However, it turns out that the two transversal components are by around six orders of magnitude smaller than the longitudinal component, due to which they are deemed irrelevant and presentation of the respective plots is omitted. In the following, the results of evaluating Eqs. (3.74) and (3.83) for varying porosities are presented. In particular, f_{can} was varied within a range of $[0.005, 0.03]$, f_{lac} within a range of $[0.01, 0.1]$, and f_{vas} within a range of $[0.02, 0.1]$, see Figures 4.5. Notably, the permeability results of approach A closely correspond to previously published values for the macroscopic cortical permeability found in experimental and modeling approaches, such as (Rouhana et al., 1981; Dillaman et al., 1991; Zhang et al., 1998; Malachanne et al., 2008). Moreover, it becomes apparent that for both approaches A and B the effects of f_{can} and f_{lac} are negligible, whereas increasing f_{vas} has a decisive influence on $K_{\mathrm{macro}}^{\mathrm{hom,\,A}}$ and $K_{\mathrm{macro}}^{\mathrm{hom,\,B}}$. Hence, on the macroscopic level, the permeability is essentially only driven by the vascular pores, and the permeability on the extravascular matrix does not play a role. It is furthermore striking that, in the studied range of f_{vas}, $K_{\mathrm{macro,\,l}}^{\mathrm{hom,\,B}}$ is around 4.5 times the value of $K_{\mathrm{macro}}^{\mathrm{hom,\,A}}$.

Interestingly, the introduction of the so-called specific surface, S_{V}, which can readily be linked to the vascular radius by

$$R_{\mathrm{vas}} = \frac{2 f_{\mathrm{vas}}}{S_{\mathrm{V}}}, \tag{4.2}$$

into Eqs. (3.74) and (3.83) yields a Kozeny-Carman-type relation for $K_{\mathrm{macro}}^{\mathrm{hom,\,A}}$ and $K_{\mathrm{macro,\,l}}^{\mathrm{hom,\,B}}$, see also Abdalrahman et al. (2015). This means that the macroscopic homogenized permeability exhibits asymptotic behavior, tending towards infinity for $f_{\mathrm{vas}} = 1$. The specific surface of bone tissue can be introduced empirically, as a function of f_{vas}, see e.g (Martin et al., 1998; Lerebours et al., 2015b).

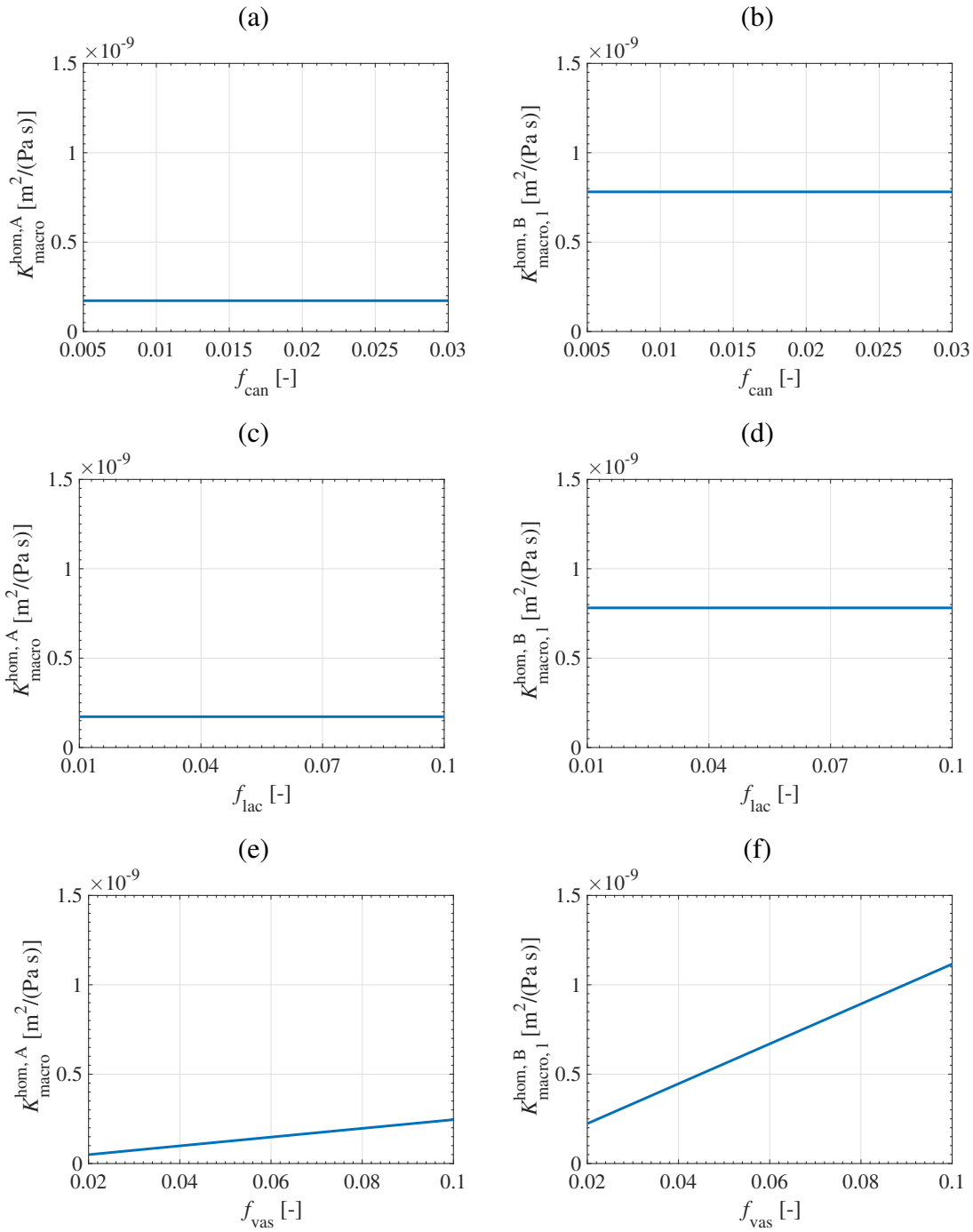

Figure 4.5.: The macroscopic permeabilities $K^{\text{hom, A}}_{\text{macro}}$ and $K^{\text{hom, B}}_{\text{macro, 1}}$ for varying f_{can}, f_{lac}, and f_{vas}, (while considering $R_{\text{can}} = 100$ nm, $R_{\text{vas}} = 25$ µm); (a) and (b) for $f_{\text{can}} \in [0.005, 0.03]$ while $f_{\text{lac}} = 0.1$ and $f_{\text{vas}} = 0.07$; (c) and (d) for $f_{\text{lac}} \in [0.01, 0.1]$ while $f_{\text{can}} = 0.02$ and $f_{\text{vas}} = 0.07$; and (e) and (f) for $f_{\text{vas}} \in [0.02, 0.1]$ while $f_{\text{can}} = 0.02$ and $f_{\text{lac}} = 0.1$

4.2. Pressure gradient downscaling

As already pointed out earlier, the mathematical framework derived in Section 3 can not only be used for permeability upscaling (as demonstrated in Section 4.1), but also for downscaling pressure gradients from the macroscopic scale to the scale of the canalicular pores. In the following, for the sake of demonstration, the downscaling relations given in Eqs. (3.44), (3.61), (3.76), and (3.86) are numerically evaluated sequentially. Hence Eqs. (3.76) and (3.86), respectively, are employed to downscale macroscopic pressure gradients to the level of the extravascular bone material. The resulting pressure gradient is inserted into Eq. (3.61) to downscale it to the level of extralacunar bone material. Finally, the pressure gradient occurring in the extralacunar bone material is inserted into Eq. (3.44) to obtain the sought-after pressure gradient in the canalicular pores, $\operatorname{grad} p_{\mathrm{can}}(\vartheta,\varphi)$. Since it has been established that fluid flow in the canalicular pores presumably occurs in longitudinal direction only, the longitudinal contribution of $\operatorname{grad} p_{\mathrm{can}}(\vartheta,\varphi)$ is computed:

$$\operatorname{grad} p_{\mathrm{can,s}}(\vartheta,\varphi) = \mathbf{e}_{\mathrm{s}}(\vartheta,\varphi)\cdot\operatorname{grad} p_{\mathrm{can}}(\vartheta,\varphi)\,, \tag{4.3}$$

with

$$\mathbf{e}_{\mathrm{s}}(\vartheta,\varphi) = (\sin\vartheta\cos\varphi,\,\sin\vartheta\sin\varphi,\,\cos\vartheta)^{\mathrm{T}}\,. \tag{4.4}$$

Furthermore, the influence of the orientation of the macroscopic pressure gradients is studied. For that purpose, the following macroscopic pressure gradients are considered: $\operatorname{grad} p_{\mathrm{macro}} = (1\;0\;0)^{\mathrm{T}}$ MPa/mm, $\operatorname{grad} p_{\mathrm{macro}} = (0\;1\;0)^{\mathrm{T}}$ MPa/mm, and $\operatorname{grad} p_{\mathrm{macro}} = (0\;0\;1)^{\mathrm{T}}$ MPa/mm. Then, considering a specific configuration of the three RVEs, the direction-dependence of the canalicular pressure gradient in response to a certain macroscopic pressure gradient can be investigated. Prescribing $f_{\mathrm{can}} = 0.02$, $f_{\mathrm{lac}} = 0.1$, $f_{\mathrm{vas}} = 0.07$, $R_{\mathrm{can}} = 100\,\mathrm{nm}$, $R_{\mathrm{vas}} = 50\,\mu\mathrm{m}$, and $\eta = 0.007$ Pa s leads to the canalicular pressure gradients shown in Figure 4.6. As expected, the maximum canalicular pressure gradient occurs in the canaliculi which are oriented in direction of the macroscopic pressure gradient.

In addition, it is interesting to study the effect of the porosities on the microscopically resulting pressure gradients, in the typical ranges as described at the beginning of Section 4. Considering a macroscopic pressure gradient of $\operatorname{grad} p_{\mathrm{macro}} = (0\;0\;1)^{\mathrm{T}}$ MPa/mm in Figure 4.7. Obviously, within the considered porosity ranges, the influence of f_{can} is of minor importance, whereas $\max(\operatorname{grad} p_{\mathrm{can,s}})$, i.e. the maximum pressure gradient occurring along all possible pore orientations, increases more significantly with increasing f_{lac} and with decreasing f_{vas}. In any case, variations within the considered porosity ranges do

not lead to substantial changes in the corresponding pressure gradients in the canalicular pores.

Furthermore, it is striking that arbitrarily oriented, interpenetrating vascular pores (approach A) induce much higher canalicular pressure gradients than vascular pores oriented along the main anatomical axis (approach B). Clearly, these results do not change when considering a differently oriented macroscopic pressure gradient; what changes is merely the direction at which the maximum canalicular pressure gradients occur.

Of course, the downscaling relations that have been used so far to compute the canalicular pore pressure gradients in response to a macroscopically prescribed one can also be employed to estimate the pressure gradients in material phases discernible on the observation scales in-between, see Figure 4.9 for the pressure gradients occurring in the extravascular bone material, and Figure 4.10 for the pressure gradients occurring in the extralacunar bone material, both related to a macroscopic pressure gradient of $\operatorname{grad} p_{\mathrm{macro}} = (0\ 0\ 1)^{\mathrm{T}}$ MPa/mm. The aforementioned figures reveal that for approach A, i.e for arbitrarily oriented vascular pores, a non-negligible porosity-dependence is only observed for the effect of $\operatorname{grad} p_{\mathrm{exlac}}$on f_{lac}, whereas for approach B, i.e. for the vascular pores oriented in direction of the main anatomical axis, $\operatorname{grad} p_{\mathrm{exvas}}$ is sensitive to changes of f_{vas}, and $\operatorname{grad} p_{\mathrm{exlac}}$ is sensitive to changes of both f_{vas} and f_{can}.

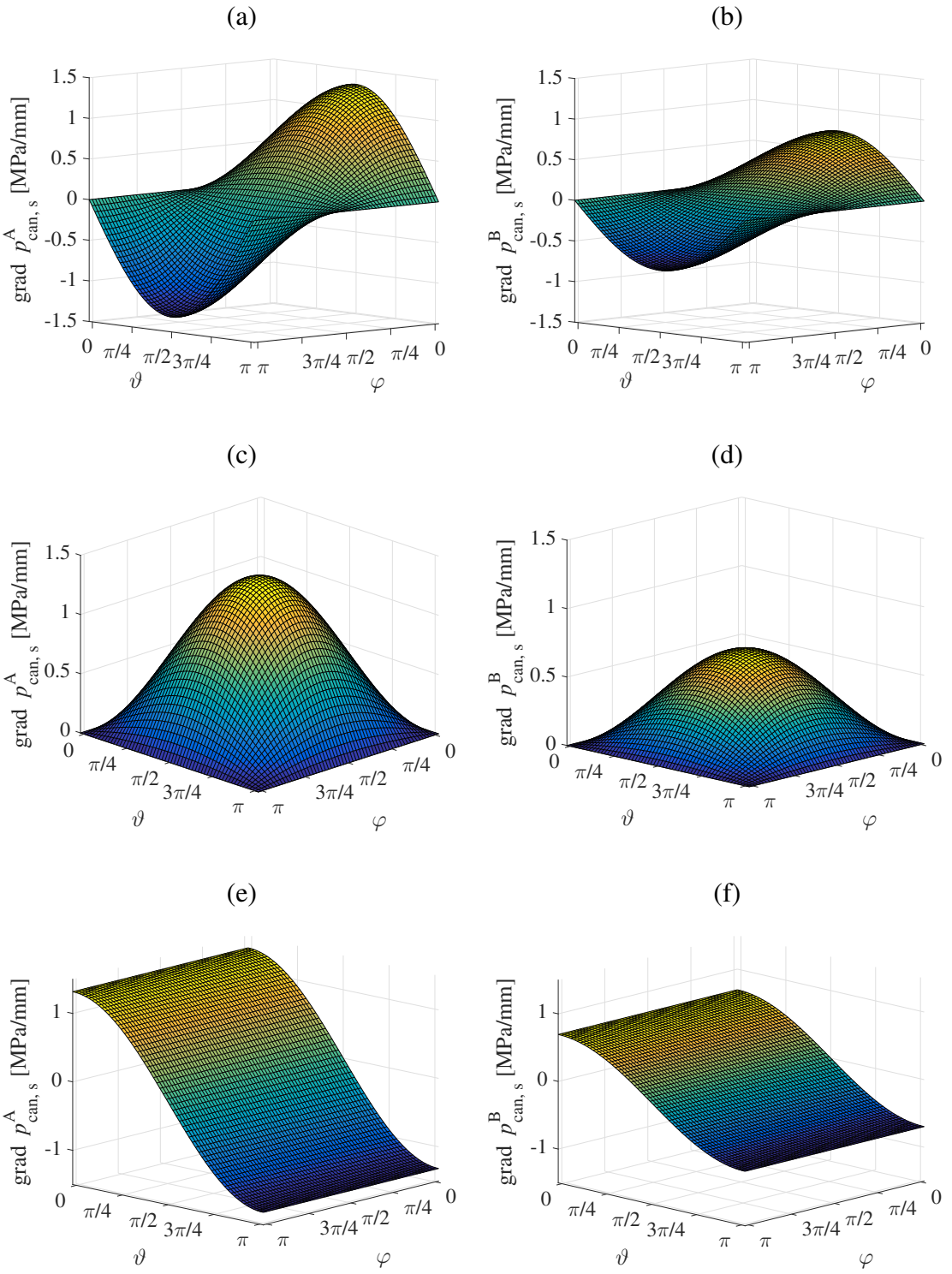

Figure 4.6.: Downscaled canalicular pressure gradient in longitudinal direction of the arbitrarily oreinted canaliculi, grad $p_{\mathrm{can,s}}(\vartheta,\varphi)$, for arbitrarily oriented vascular pores, see (a), (c) and (e), as well as for vascular pores oriented in the main anatomical direction, see (b), (d), and (f); (a) and (b) relate to a macroscopic pressure gradient of grad $p_{\mathrm{macro}} = (1\ 0\ 0)^{\mathrm{T}}$ MPa/mm, (b) and (c) relate to grad $p_{\mathrm{macro}} = (0\ 1\ 0)^{\mathrm{T}}$ MPa/mm, and (e) and (f) relate to grad $p_{\mathrm{macro}} = (0\ 0\ 1)^{\mathrm{T}}$ MPa/mm, see (e) and (f)

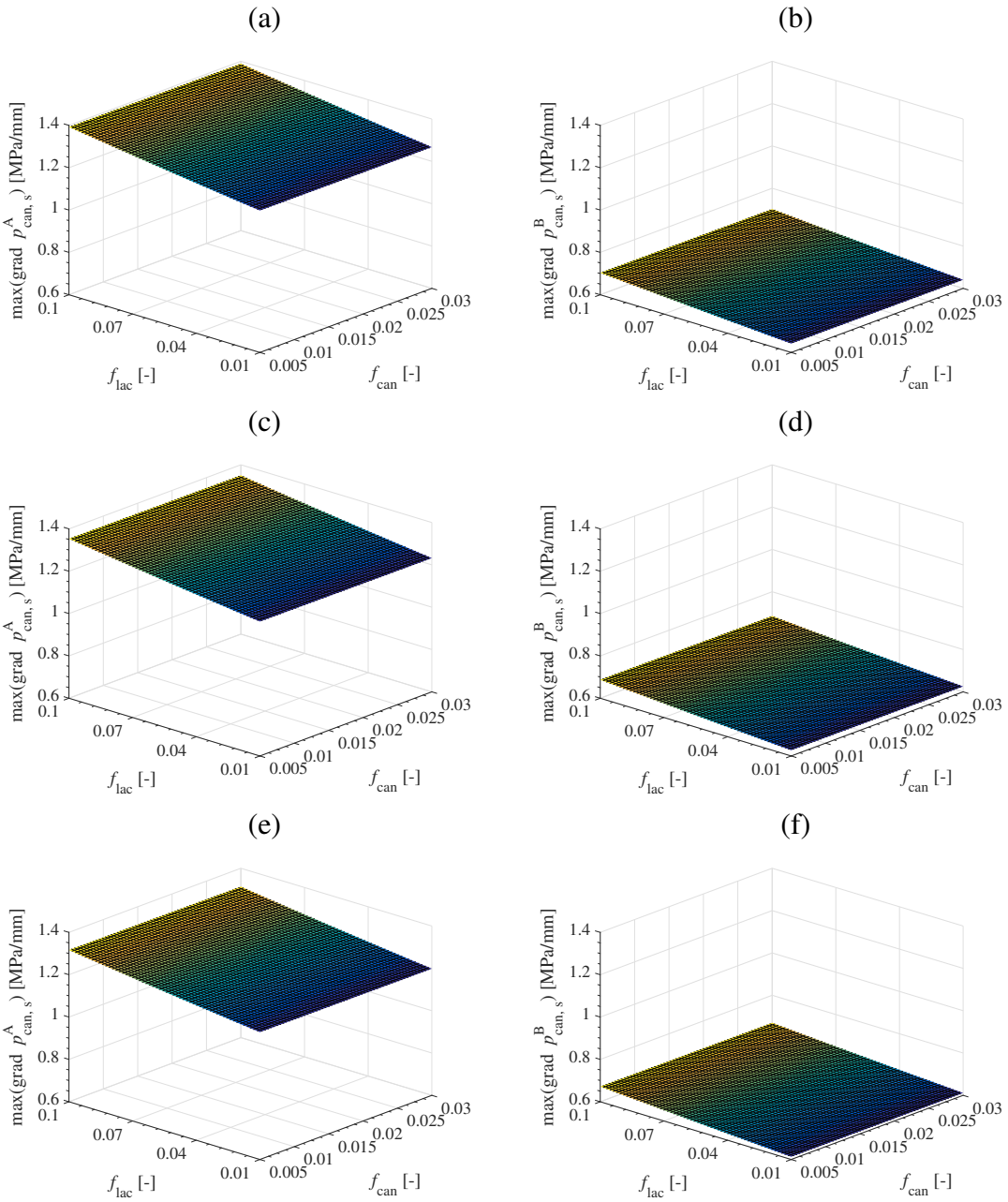

Figure 4.7.: Dependence of the maximum canalicular pressure gradient in pore direction, $\max(\operatorname{grad} p_{\mathrm{can,s}})$ for $\operatorname{grad} p_{\mathrm{macro}} = (0\,0\,1)^{\mathrm{T}}$ MPa/mm, on the porosities f_{can}, f_{lac}, and f_{vas}; for $f_{\mathrm{vas}} = 0.05$, see (a) and (b), $f_{\mathrm{vas}} = 0.075$, see (c) and (d), and $f_{\mathrm{vas}} = 0.1$, see (e) and (f); in all studies f_{can} is varied between $[0.005, 0.03]$ and f_{lac} between $[0.01, 0.1]$, while $R_{\mathrm{can}} = 100\,\mathrm{nm}$ and $R_{\mathrm{vas}} = 50\,\mu\mathrm{m}$; (a), (c), and (e) relate to arbitrarily oriented vascular pores (approach A), while (b), (d), and (f) relate to vascular pores oriented in direction of the main anatomical axis (approach B)

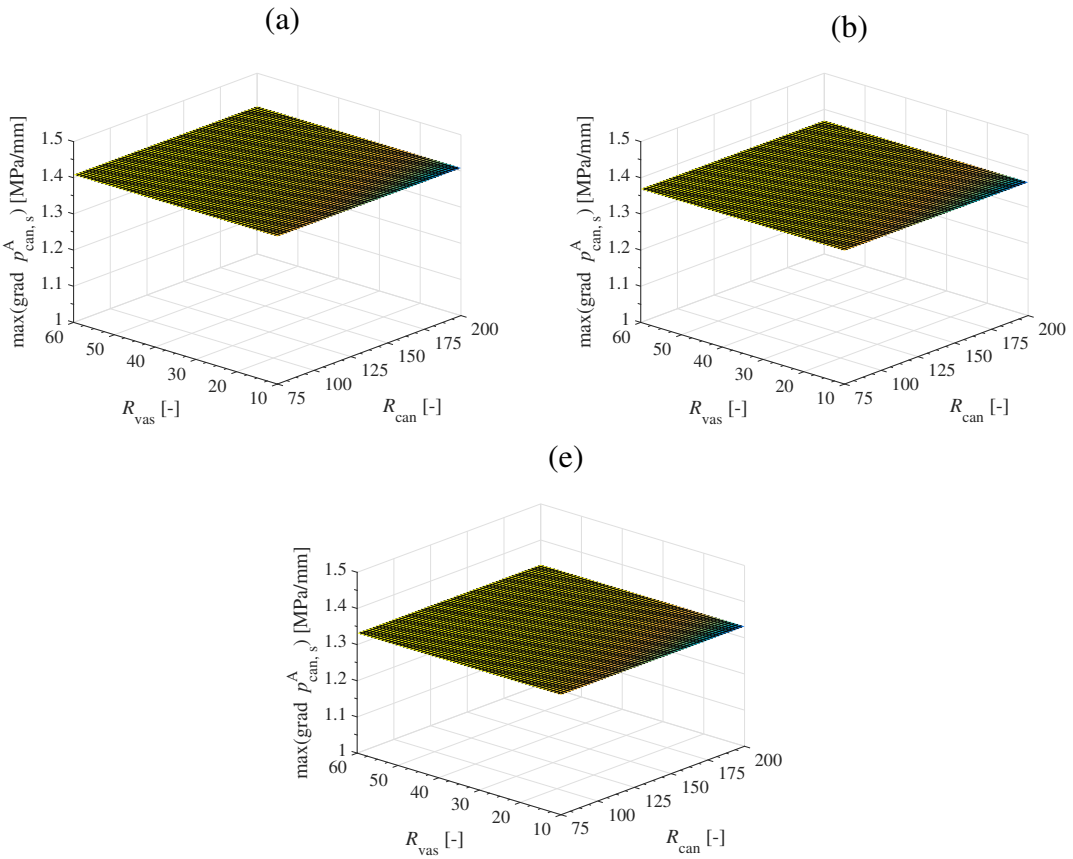

Figure 4.8.: dependence of the maximum canalicular pressure gradient in pore direction for arbitrarily oriented vascular pores, $\max(\operatorname{grad} p^{\mathrm{A}}_{\mathrm{can,s}})$ for $\operatorname{grad} p_{\mathrm{macro}} = (0\,0\,1)^{\mathrm{T}}$ MPa/mm, on the radii R_{can} and R_{vas}; for $f_{\mathrm{vas}} = 0.05$, see (a), $f_{\mathrm{vas}} = 0.075$, see (b), and $f_{\mathrm{vas}} = 0.1$, see (c); in all studies R_{can} is varied between $[75,\ 200]$ nm and R_{vas} between $[10,\ 60]$ µm, while $f_{\mathrm{can}} = 0.03$ and $f_{\mathrm{lac}} = 0.1$

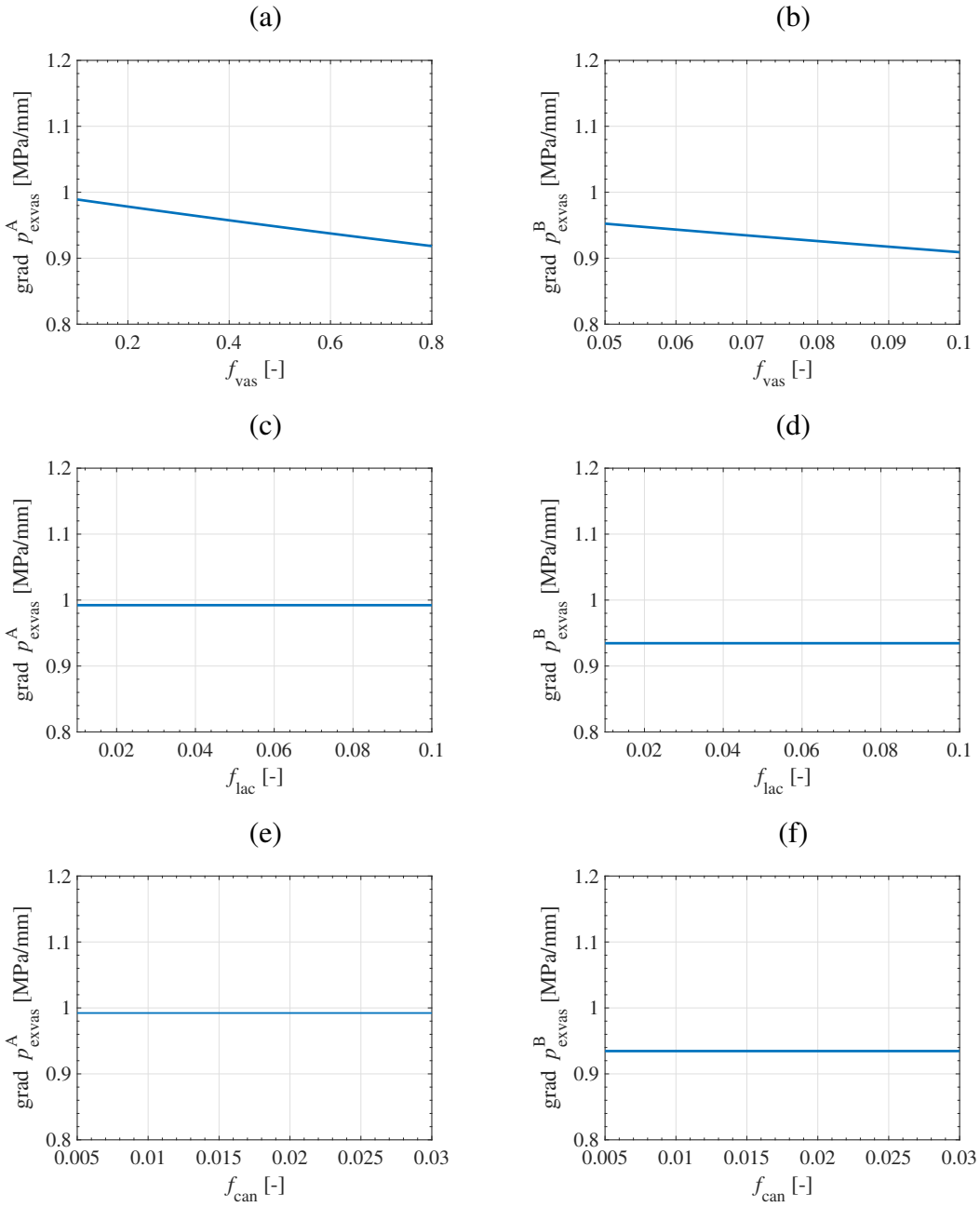

Figure 4.9.: Dependence of the downscaled extravascular pressure gradients $\operatorname{grad} p_{\mathrm{exvas}}$ for a macroscopic pressure gradient of $\operatorname{grad} p_{\mathrm{macro}} = (0\ 0\ 1)^{\mathrm{T}}$ MPa/mm, for arbitrarily oriented vascular pores, see (a), (c) and (e) as well as for vascular pores oriented in the main anatomical direction, see (b), (d), and (f), on $f_{\mathrm{vas}} \in [0.05, 0.1]$, while considering $f_{\mathrm{can}} = 0.02$, $f_{\mathrm{lac}} = 0.1$, see (a) and (b), depending on $f_{\mathrm{lac}} \in [0.01, 0.1]$, while $f_{\mathrm{can}} = 0.02$, $f_{\mathrm{vas}} = 0.07$, see (c) and (d), and depending on $f_{\mathrm{can}} \in [0.005, 0.03]$, while $f_{\mathrm{lac}} = 0.1$, $f_{\mathrm{vas}} = 0.07$, see (e) and (f) (while considering $R_{\mathrm{can}} = 100\,\mathrm{nm}$, $R_{\mathrm{vas}} = 50\,\mu\mathrm{m}$)

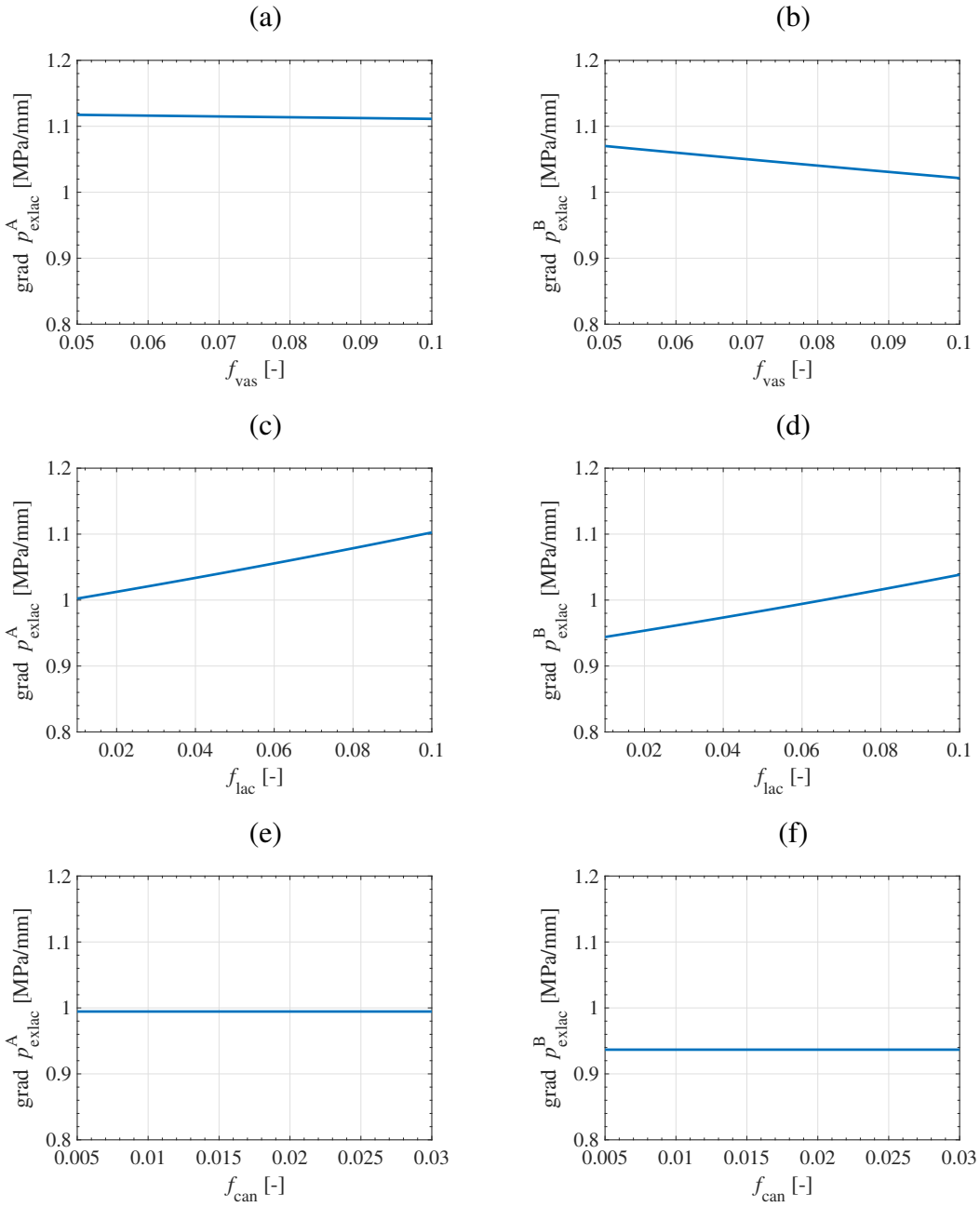

Figure 4.10.: Dependence of the downscaled extralacunar pressure gradients $\operatorname{grad} p_{\mathrm{exlac}}$ for a macroscopic pressure gradient of $\operatorname{grad} p_{\mathrm{macro}} = (0\ 0\ 1)^{\mathrm{T}}$ MPa/mm, for arbitrarily oriented vascular pores, see (a), (c) and (e) as well as for vascular pores oriented in the main anatomical direction, see (b), (d), and (f), on $f_{\mathrm{vas}} \in [0.05, 0.1]$, while considering $f_{\mathrm{can}} = 0.02$, $f_{\mathrm{lac}} = 0.1$, see (a) and (b), depending on $f_{\mathrm{lac}} \in [0.01, 0.1]$, while $f_{\mathrm{can}} = 0.02$, $f_{\mathrm{vas}} = 0.07$, see (c) and (d), and depending on $f_{\mathrm{can}} \in [0.005, 0.03]$, while $f_{\mathrm{lac}} = 0.1$, $f_{\mathrm{vas}} = 0.07$, see (e) and (f) (while considering $R_{\mathrm{can}} = 100\,\mathrm{nm}$, $R_{\mathrm{vas}} = 50\,\mu\mathrm{m}$)

5. Assessment of the capacity of canalicular fluid flow as stimulus of osteocyte activities in cortical bone

This section is finally devoted to addressing the fundamental question of this thesis, namely whether the fluid flow occurring in the canalicular pores of bone is a potent stimulus, effectively mediating the activities of osteocytes. For simplicity and for conciseness, the focus is thereby on cortical bone, whereas the analysis presented subsequently could be similarly carried out for trabecular bone.

5.1. Estimation of a physiologically relevant macroscopic pressure gradient

Based on gait analysis (Forner–Cordero et al., 2006), strain gauge measurements (Cordey and Gautier, 1999), and mathematical modeling (Duda et al., 1997), a (compressive) normal force of $N = -700$ N, and a bending moment of $M = 50$ Nm were identified to represent physiological loading conditions to which a human femur is typically subjected (Lerebours et al., 2015a). Assuming that in the long, median part of a femur (i.e., the *vastus intermedius*), the organ structure somewhat resembles an annular beam, see Figure 5.1, it seems reasonable to utilize the well-established concept of beam theory for translating the aforementioned compressive force and bending moment into a corresponding distribution of mechanical stress.

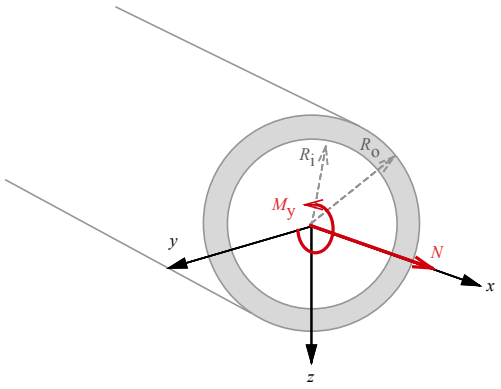

Figure 5.1.: The midshaft of a long bone is approximated as a hollow cylinder with an inner R_i and an outer radius R_o, exposed to an axial loading N and a bending moment M_y.

The classical equation defining the stress distribution in the cross-section of an Euler-Bernoulli beam due to combined axial and bending loading reads as (Timoshenko, 1953; Gere and Timoshenko, 1997; Mang and Hofstetter, 2004)

$$\sigma_{xx}(y,z) = \frac{N}{A} + \frac{M_y}{I_y} z - \frac{M_z}{I_z} y. \tag{5.1}$$

where $\sigma_{xx}(y,z)$ is the normal stress component in x-direction (i.e. the main anatomical axis if the beam is considered to represent a long bone), N is the normal force, M_y and M_z, respectively, are the bending moments with respect to the y- and z-axes, I_y and I_z, respectively, are the moments of inertia (or second moment of area) with respect to the y- and z-axes, respectively, and x, y, and z are the coordinates of a Cartesian coordinate system whose origin is located at the centroid of the cross-section. The shape of the cross-section implies that

$$I_x = I_z = I = \frac{A}{4}\left(R_o^2 + R_i^2\right) \tag{5.2}$$

with R_i and R_o being the inner and outer radii of the annular beam – hence, R_i defines the medullary cavity of the organ – and A is the cross-sectional area, $A = (R_o^2 - R_i^2)\pi$. Eq. (5.1) is now evaluated while considering that $N = -700\,\mathrm{N}$, $M_y = M = 50\,\mathrm{Nm}$, and $M_z = 0$. Further taking into account that $R_i = 5.05\,\mathrm{mm}$ and $R_o = 14.2\,\mathrm{mm}$ (Liu et al., 2017; Huang et al., 2012), then leads to

$$\sigma_{xx}[\mathrm{MPa}] = -1.30 + 1.60 \times 10^3 \cdot z. \tag{5.3}$$

For translating $\sigma_{xx}(z)$ into a corresponding pressure distribution, the hydrostatic part of the related stress tensor is considered:

$$p_{\mathrm{macro}}(z) = -\frac{1}{3}\mathrm{tr}\left(\sigma(x)\right) = -\frac{1}{3}\sigma_{xx}(z) \tag{5.4}$$

In further consequence,

$$\operatorname{grad} p_{\mathrm{macro}} = \begin{pmatrix} 0 \\ 0 \\ -533.3 \end{pmatrix}_{\mathbf{e}_x,\mathbf{e}_y,\mathbf{e}_z} , \tag{5.5}$$

given in MPa/mm, follows.

5.2. Estimation of fluid velocities typically occurring in the canalicular pores

In the following, the fluid flow occurring in the canalicular pores will be estimated based on the downscaling relations that were derived in Section 3 and discussed in terms of numerical evaluation in Section 4.2, considering macroscopic pressure gradients found in Section 5.1 as input quality. Combining the aforementioned downscaling relation, the subsequently presented numerical results are based on the following two equations:

$$\mathbf{v}^{\mathrm{A}}_{\mathrm{can}}(\vartheta,\varphi) = -\mathbf{k}_{\mathrm{can}}(\vartheta,\varphi)\cdot\mathbf{A}_{\mathrm{can}}(\vartheta,\varphi)\cdot\mathbf{A}_{\mathrm{exlac}}\cdot\mathbf{A}^{\mathrm{A}}_{\mathrm{exvas}}\cdot\operatorname{grad} p_{\mathrm{macro}}\,, \tag{5.6}$$

and

$$\mathbf{v}^{\mathrm{B}}_{\mathrm{can}}(\vartheta,\varphi) = -\mathbf{k}_{\mathrm{can}}(\vartheta,\varphi)\cdot\mathbf{A}_{\mathrm{can}}(\vartheta,\varphi)\cdot\mathbf{A}_{\mathrm{exlac}}\cdot\mathbf{A}^{\mathrm{B}}_{\mathrm{exvas}}\cdot\operatorname{grad} p_{\mathrm{macro}}\,, \tag{5.7}$$

The component of interest is the flow along the canalicular longitudinal axis, requiring the calculation of the longitudinal component of the canalicular velocity vector, according to

$$v^{\mathrm{A}}_{\mathrm{can,s}}(\vartheta,\varphi) = \mathbf{e}_{\mathrm{s}}(\vartheta,\varphi)\cdot\mathbf{v}^{\mathrm{A}}_{\mathrm{can}}(\vartheta,\varphi) \tag{5.8}$$

and

$$v^{\mathrm{B}}_{\mathrm{can,s}}(\vartheta,\varphi) = \mathbf{e}_{\mathrm{s}}(\vartheta,\varphi)\cdot\mathbf{v}^{\mathrm{B}}_{\mathrm{can}}(\vartheta,\varphi)\,, \tag{5.9}$$

where the maximum velocities, $\max(v^{\mathrm{A}}_{\mathrm{can,\,s}})$ and $\max(v^{\mathrm{B}}_{\mathrm{can,\,s}})$, are obtained for canaliculi arranged parallel to the macroscopic pressure gradient.

Subsequently, several numerical studies are presented, illustrating the effects of variations in f_{can}, f_{lac}, f_{vas}, R_{can}, and R_{vas} on the resulting velocities, thereby considering the ranges of these parameters that have been justified to be physiologically meaningful in Section 4, namely $f_{\mathrm{can}} \in [0.005, 0.03]$, $f_{\mathrm{lac}} \in [0.01, 0.1]$, $f_{\mathrm{vas}} \in [0.05, 0.1]$, $R_{\mathrm{can}} \in [75, 200]$ nm, and $R_{\mathrm{vas}} \in [10, 60]$ µm, see Figures 5.2, 5.3 and 5.4.

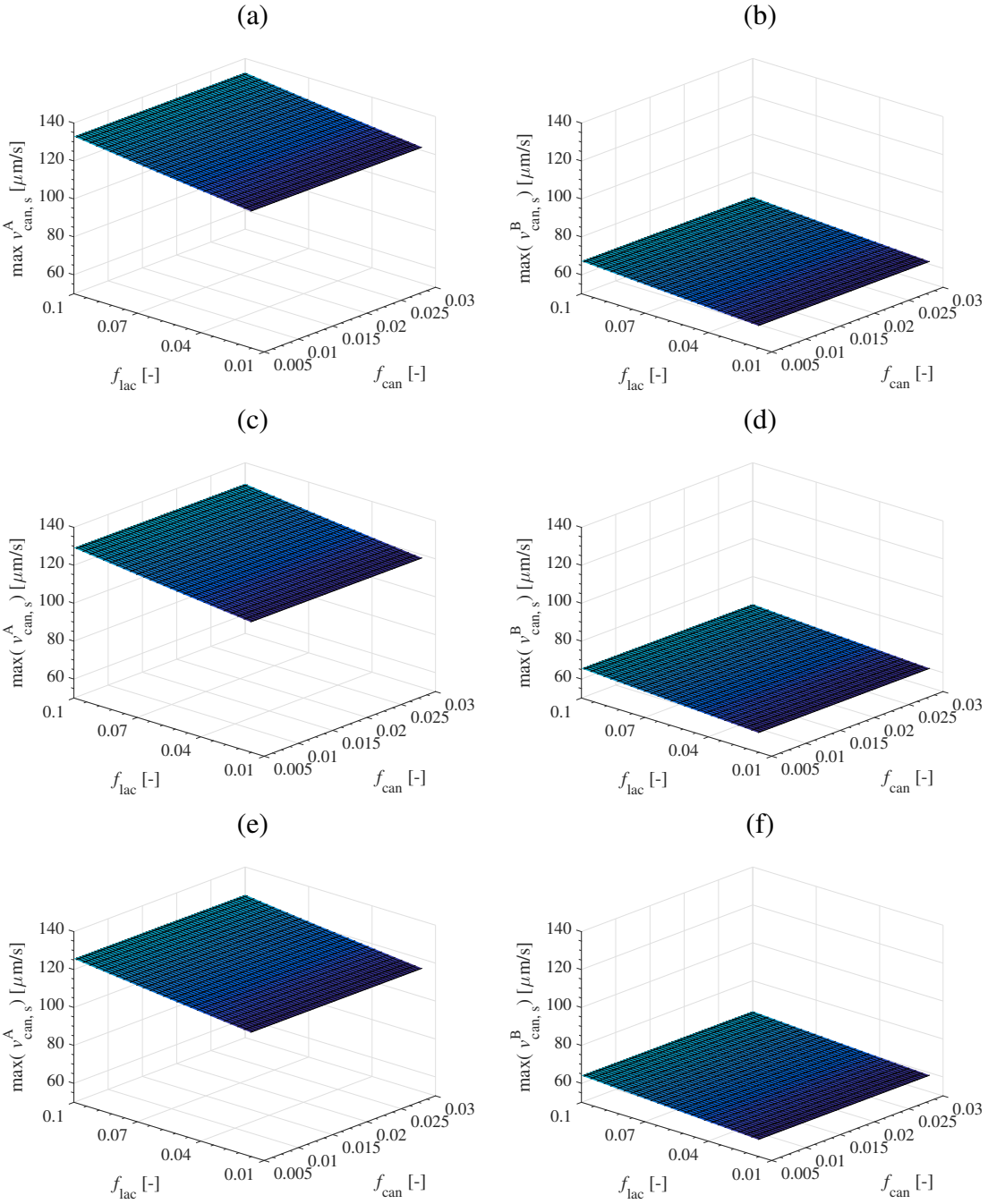

Figure 5.2.: Dependence of the maximum canalicular velocities $\max(v^{A}_{can,s})$ and $\max(v^{B}_{can,s})$ on the porosities f_{lac} in a range of 0.01 – 0.1, and f_{can} in a range of 0.005 – 0.03 for arbitrarily oriented vascular pores, see (a), (c), and (e), and for longitudinally oriented vascular pores (b), (e), and (f), considering $f_{vas} = 0.05$, see (a) and (b), $f_{vas} = 0.075$, see (c) and (d), and $f_{vas} = 0.1$, see (e) and (f), (while considering $R_{can} = 100\,\text{nm}$ and $R_{vas} = 50\,\mu\text{m}$)

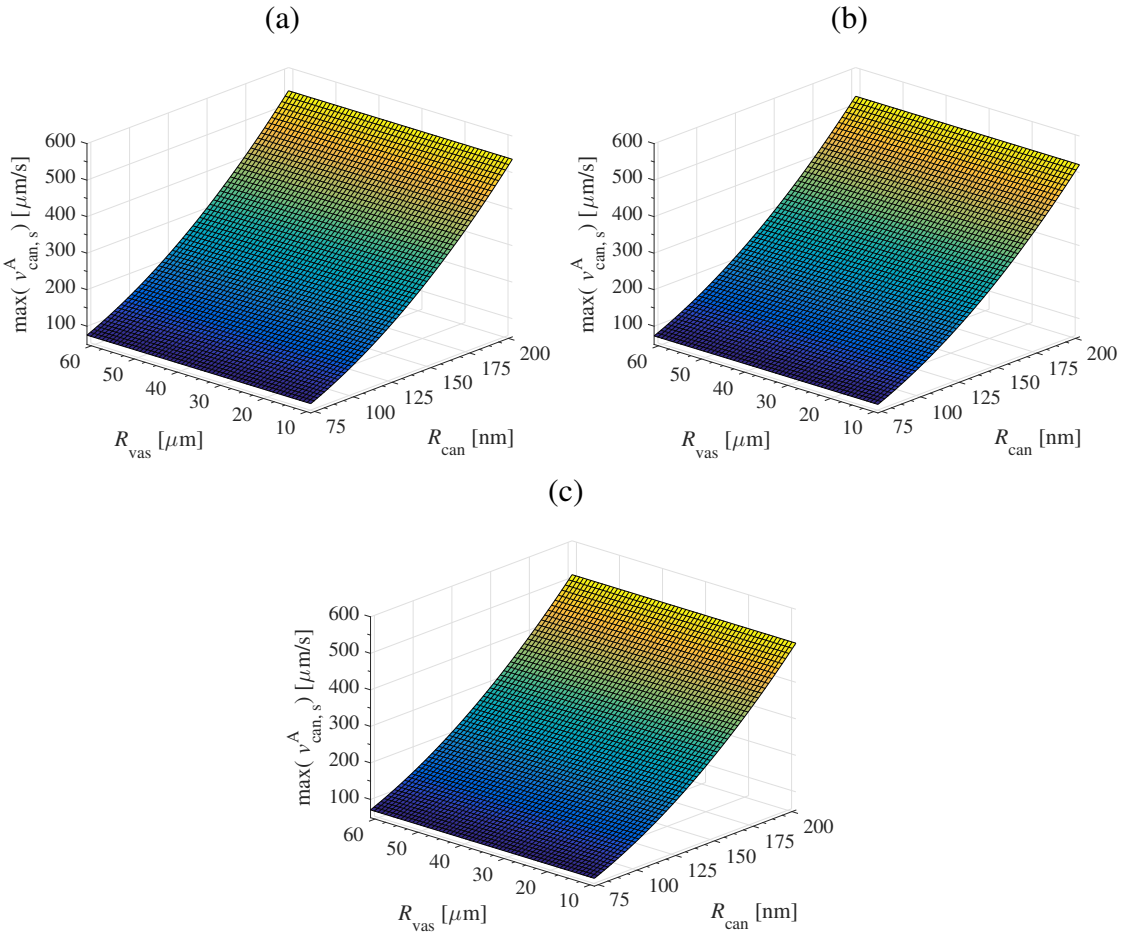

Figure 5.3.: Dependence of the maximum canalicular velocities $\max(v^{A}_{can,s})$ on the radii R_{vas} ranging between 10 – 60 µm, and R_{can} ranging between 75 – 200 nm, for arbitrarily oriented vascular pores, considering $f_{vas} = 0.05$, see (a), for $f_{vas} = 0.075$, see (b), and for $f_{vas} = 0.1$, see (c) (while $f_{can} = 0.02$ and $f_{lac} = 0.1$)

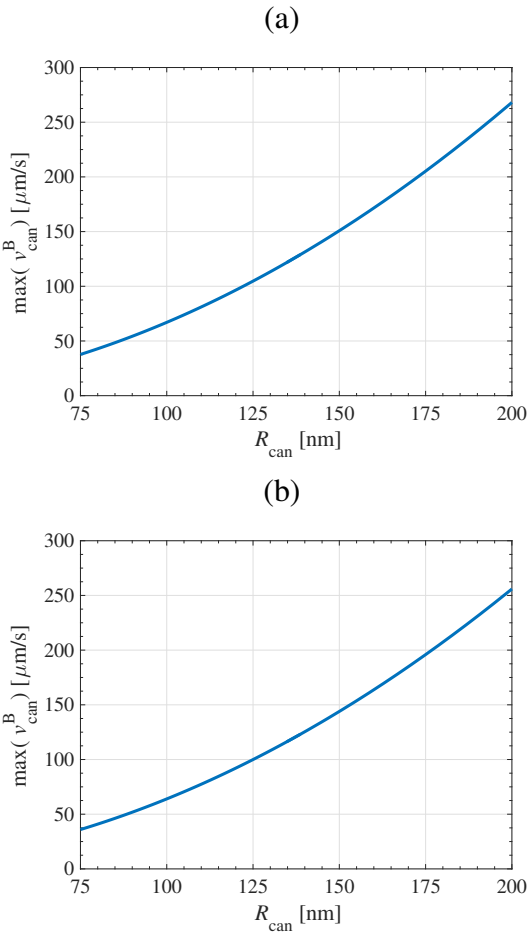

Figure 5.4.: Dependence of the maximum canalicular velocities $\max(v^{B}_{can,s})$ on the radius R_{can} ranging between 75 – 200 nm, for longitudinally oriented vascular pores, considering $f_{vas} = 0.05$, see (a), and for $f_{vas} = 0.1$, see (b) (while considering $f_{can} = 0.02$ and $f_{lac} = 0.1$)

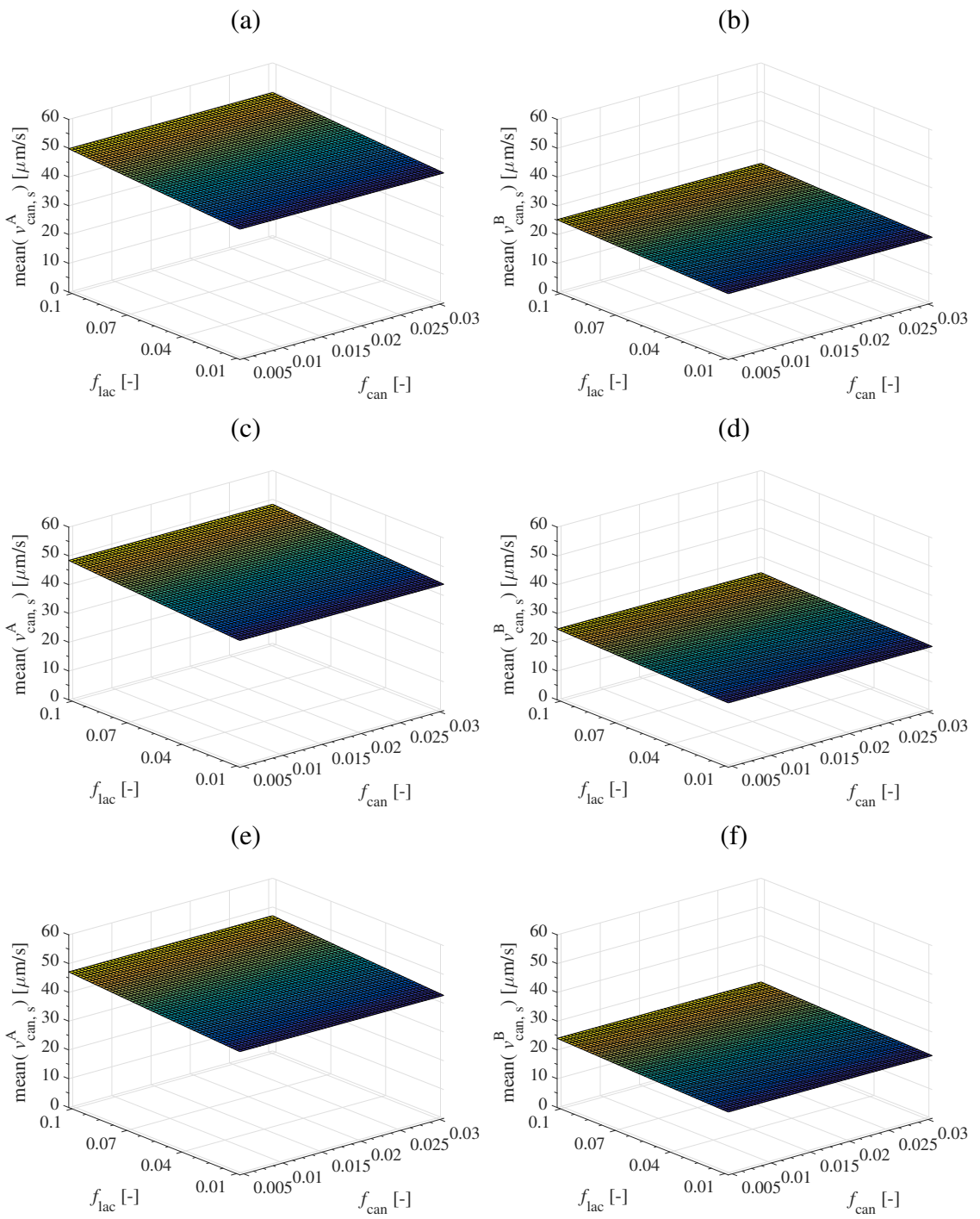

Figure 5.5.: Dependence of the mean canalicular velocities mean($v^{A}_{can,s}$) and mean($v^{B}_{can,s}$) on the porosities f_{lac} in a range of 0.01 – 0.1, and f_{can} in a range of 0.005 – 0.03 for arbitrarily oriented vascular pores, see (a), (c), and (e), and for longitudinally oriented vascular pores (b), (e), and (f), considering $f_{vas} = 0.05$, see (a) and (b), $f_{vas} = 0.075$, see (c) and (d), and $f_{vas} = 0.1$, see (e) and (f), (while considering $R_{can} = 100\,\text{nm}$ and $R_{vas} = 50\,\mu\text{m}$)

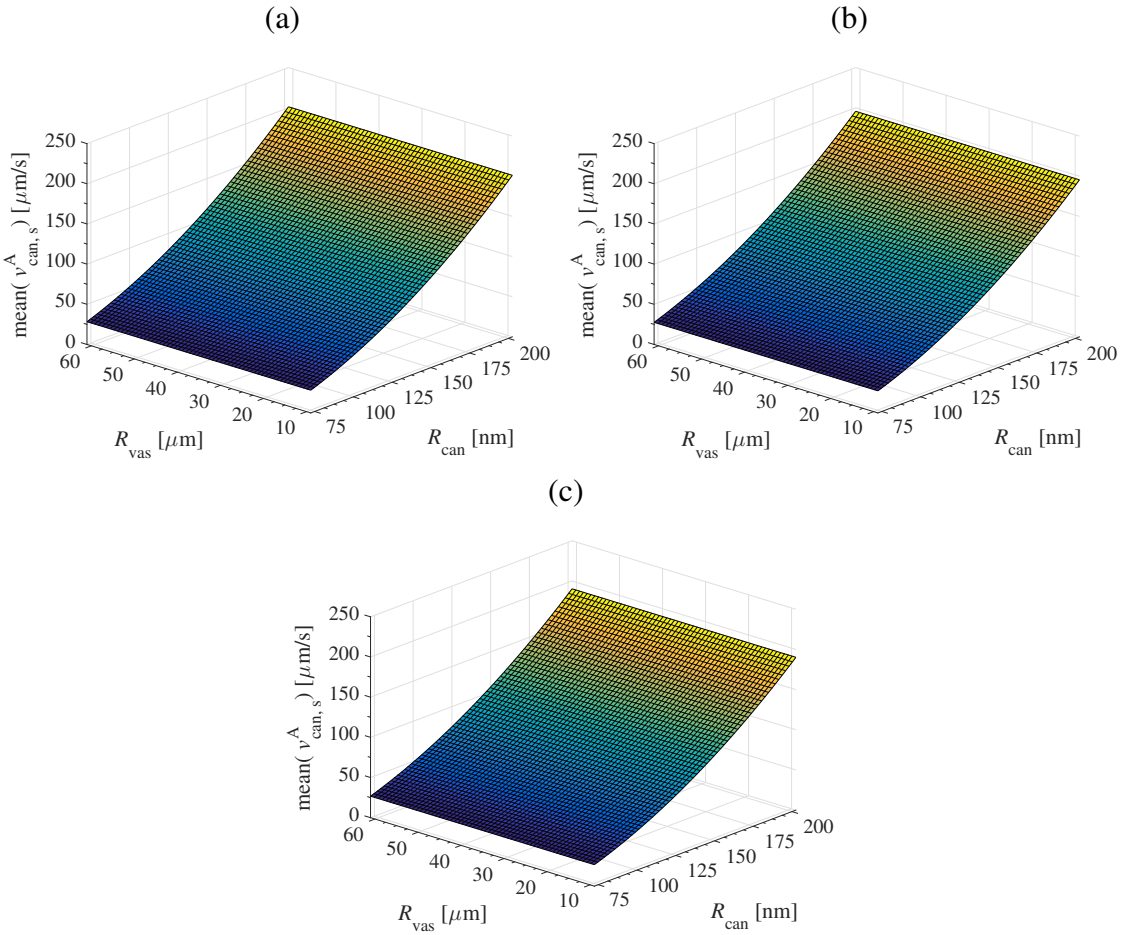

Figure 5.6.: Dependence of the mean canalicular velocities mean($v^{A}_{can,s}$) on the radii R_{can} ranging between 75 – 200 nm, and R_{vas} ranging between 10 – 60 μm, for randomly oriented vascular pores, considering $f_{vas} = 0.05$, see (a), $f_{vas} = 0.075$, see (b), and $f_{vas} = 0.1$, see (c) (while considering $f_{can} = 0.02$ and $f_{lac} = 0.1$)

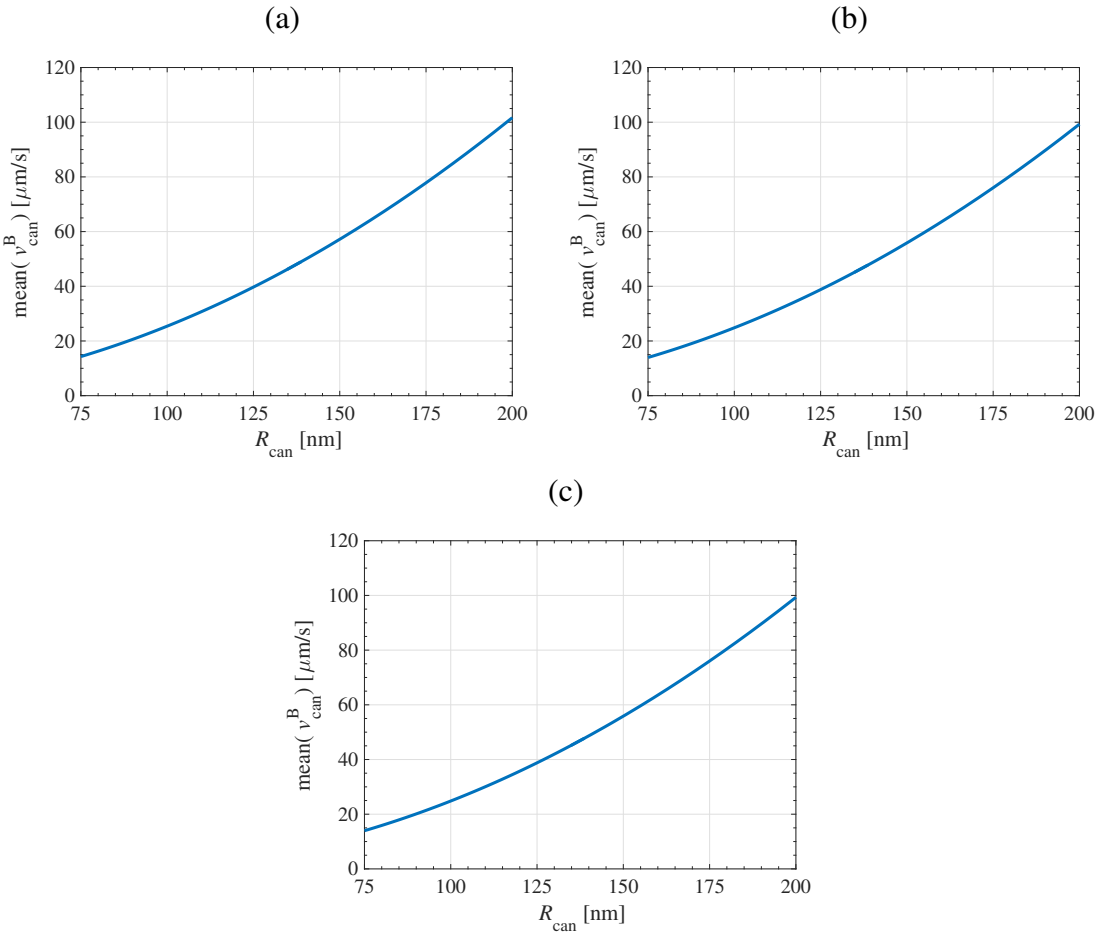

Figure 5.7.: Dependence of the mean canalicular velocities mean($v_{can,s}^{B}$) on the radius R_{can} ranging between 75 – 200 nm, for longitudinally oriented vascular pores, considering $f_{vas} = 0.05$, see (a), $f_{vas} = 0.075$, and $f_{vas} = 0.1$, see (c) (while considering $f_{can} = 0.02$ and $f_{lac} = 0.1$)

5.3. Comparison of model predictions and experimental data

A large number of experiments have been performed in order to verify the so-called "fluid flow-hypothesis", which is based on the assumption that the shear forces acting on cell body and cell processes of osteocytes resulting from the flow of the surrounding pore fluid lead to excitation of the cell. For example, parallel plate setups described by by Klein–Nulend et al. (1995b) and originally by Frangos et al. (1988) have been utilized in many studies, showing that shear forces of around 0.01 to 3 Pa prompt an increased ATP production in the cell (Vaughan et al., 2014; Genetos et al., 2005; Smalt et al., 1997), higher levels of prostaglandin (Bakker et al., 2003; Klein–Nulend et al., 1995a; Haut Donahue et al., 2003), and elevated levels of intracellular calcium ions (Haut Donahue et al., 2003). The cells are usually cultured in a monolayer and firmly attached to a glass slide before they are placed in the flow channel, which has two fluid reservoirs on either end, one higher than the other; thus the flow is driven by gravity, while a constant pressure head is maintained by a pump that drives the fluid back up from the lower reservoir to the higher one. The shear forces that were exerted on either osteoblasts or osteocytes in the 2D flow chamber experiments varied between 0.01 Pa (Smalt et al., 1997) and 2 Pa (Jacobs et al., 1998), depending on the experimental geometry and the viscosity of the utilized fluid. In many studies (Frangos et al., 1988; Genetos et al., 2005; Bakker et al., 2003; Klein–Nulend et al., 1995a; Haut Donahue et al., 2003; Kreke et al., 2005; Jacobs et al., 1998), the shear force acting onto the cell wall was estimated by means of

$$\tau = \frac{6Q\eta}{bh^2}\,, \tag{5.10}$$

relating the cell wall shear force τ to the average volumetric flow rate in the channel Q, with $h \cdot b$ being the channel cross-sectional area, and η the dynamic fluid viscosity. However, the equation above is based on the assumption of steady laminar flow, and can thus be only applied to a very limited amount of cases *in vitro* and is not likely to apply to *in vivo* conditions (Scheiner et al., 2015). It should also be mentioned that most of the considered studies utilized a fluid viscosity of $\eta = 0.001$ Pa s. However, the actual viscosity of bone pore fluid is expected to be higher than that, by around factor 7, see the respective discussion at the beginning of Section 4. Hence, the reliability and adequacy of experimentally obtained shear forces is rather questionable.

Table 5.1.: Values for the fluid velocity v that have been shown to stimulate bone cells *in vitro*

Reference	Experiment	v [μm/s]	Results
Genetos et al. (2005)	Steady laminar fluid flow on osteoblasts in flow channel for 5 minutes	$44 \cdot 10^3$	Increase of ATP production in 1^{st} minute of stimulation
Haut Donahue et al. (2003)	Oscillating fluid flow on osteoblasts, with different viscosities, flow rates and peak shear stresses	$107 \cdot 10^3$ $26.8 \cdot 10^3$ $68.5 \cdot 10^3$	Increased intracellular Ca^{2+} concentration and prostaglandin
Smalt et al. (1997)	Osteoblasts in flow channel with varying steady flow rates and experiments with increased viscosity	200 660 $132 \cdot 10^3$	NO and PGE_2 production, especially high for higher viscosity
Kreke et al. (2005)	Steady laminar flow on bone marrow stromal cells	$7.5 \cdot 10^3$	Osteoblastic cell differentiation
Jacobs et al. (1998)	Osteoblasts in parallel flow chamber; constant, oscillating, and pulsed flow	$107 \cdot 10^3$	Increased intracellular Ca^{2+}; response lowest for oscillating, decrease for higher frequency
Bakker et al. (2001)	Pulsating fluid flow in flow chamber on osteoblasts	$27.8 \cdot 10^3$ $45.8 \cdot 10^3$ $87.5 \cdot 10^3$	NO and PGE_2 production
Sinlapabodin et al. (2016)	Perfusion bioreactor with osteoblast precursor cells, 30 or 60 min steady flow	434 $1.30 \cdot 10^3$ $2.17 \cdot 10^3$	Osteogenic differentiation
Li et al. (2009)	hBMSCs in perfusion bioreactor with different flow rates and varying shear stresses by adapting fluid viscosity; fluid dynamics simulation for shear stress	430 870 $1.30 \cdot 10^3$	Increased osteoblast differentiation, especially for the highest shear stress (0.015 Pa) and the lowest mass transport (3 $\frac{\text{ml}}{\text{min}}$)
Bancroft et al. (2002)	Long-term fluid perfusion of 3D scaffold seeded with marrow stromal osteoblasts	18.5 61.7 185	Enhanced matrix deposition

For the above-mentioned reasons, only directly measured fluid flow *velocities* are considered in the following, see the overview presented in Table 5.1. Besides osteocytes (or osteocyte-type cells), this overview includes other kinds of cells occurring in bone as

well.[8] Thereby, the effects of the fluid velocities acting on these cells *in vitro* include indications of immediate anabolic activity such as ATP, nitric oxide and prostaglandins (Bonewald, 2006). Nitric oxide, a short-lived radical, is not only produced by osteocytes, but also by osteoblasts in response to mechanical loading in order to promote bone formation and suppress resorption by suppressing osteoclastogenisis via OPG and RANK-L signaling (Smalt et al., 1997; Tan et al., 2007). The type-E prostaglandins, especially prostaglandin E_2, that are produced by mechanical loading have been shown to promote as well as suppress bone resorption and formation (Pilbeam et al., 2008; Bonewald and Johnson, 2008; Kamel et al., 2006). PGE_2 production is enabled by the entrance of Ca^{2+} into the osteocyte, possibly through mechanosensitive channels (Ajubi et al., 1999).

As seen in Table 5.1, the experimentally used fluid velocities are much (by orders of magnitude) higher than most of the canalicular velocities that were computed by means of the multiscale model presented in this work, see Section 5.2, irrespective of the considered parameter variations. The only effective "amplifier" of the canalicular fluid flow seems to be the radius of the canaliculi, although it should be noted that not even the maximum fluid flow velocities related to the maximum canalicular radii reach the velocities which turned out to be required to stimulate cells *in vitro*, see Figures 5.2, 5.3 and in particular 5.4; and this is even more true for the average velocities, being the arithmetic mean over all possible pore orientations, see Figures 5.6 – 5.7. One important contributor to this outcome is certainly the effect of water layering which effectively reduces the permeability of bone tissue and thus leads to a decreased canalicular flow velocity by a factor 7; relating to an increase of the viscosity from $\eta = 0.001$ Pa s to $\eta = 0.007$ Pa s.

Recalling the initially posed key question of this thesis, these results imply that, at least for the bone configurations studied in this work, the pressure gradient-induced fluid flow in the canalicular pores fails to be a potent stimulus for osteocyte activities. However, several situations are conceivable in which the here computed velocities may be substantially exceeded; for example when considering areas subjected to much higher bending moments; when considering areas of porosity heterogeneities (i.e. when the composition of the bone tissue further increases the loading-induced pressure gradients); and of course

[8] Notably, osteoblasts are more easiely isolated than osteocytes, and a number of relevant lineages are available. Hence, osteoblasts are often considered to be experimentally favorable, as compared to osteocytes. However, even though osteocytes and osteoblasts are from the same lineage, there are differences between the two cell types in response to mechanical stimulation (Bonewald and Johnson, 2008; Lu et al., 2012). Higher levels of shear stress are required to prompt a release of PGE_2 in osteoblasts compared to osteocytes (1.6 Pa versus 0.2 Pa) (Kamel et al., 2010). On the other hand, it was shown that the calcium response to shear stress was higher in osteoblasts in the range of 1.2 – 2.4 Pa compared to osteocytes and the authors attributed this difference to the lower degree of focal adhesion on the glass slide of osteocytes, compared to osteoblasts (Kamioka et al., 2006)

when considering, instead of the canalicular pores, the vascular pores, where, due to the much larger pore dimensions, the fluid velocities can be expected to be much higher as well.

Hence, the bottomline of this work is that, according to the computations presented in the previous sections, pressure gradient-driven fluid flow in the pore spaces of bone cannot be considered to occur in *all* of the here studied bone pore spaces at the required magnitude (especially not in the canalicular pores where it had been assumed that fluid flow effectively acts on the there residing cell processes of osteocytes). However, under certain, physiologically still reasonable loading conditions, sufficiently large pressure gradients may develop, especially in the large pore spaces of bone. Hence osteoblasts, osteoclasts, and bone lining cells, all of which are located in the vascular pore space, may indeed experience excitation by fluid flow.

6. Summary and concluding remarks

In this thesis, a multiscale model of bone tissue has been presented, allowing for upscaling the permeability of single canalicular pores up to the macroscopic level. This model can also be utilized for scaling macroscopically applied mechanical loading down to the correspondingly arising pressure gradients in canalicular (and also lacunar and vascular) pores, where they drive Poiseuille-type flow of the pore fluid. This way, besides also studying the various, composition- and morphology-related influences on the upscaled (or homogenized) permeability, the important question was addressed whether physiologically relevant macroscopic loading conditions are able to provoke canalicular pressure gradients that are capable of effectively stimulating the activities of osteocytes (whose cell processes are located in the canaliculi). For that purpose, the computed fluid velocities were compared with the fluid velocities that could be shown experimentally to induce cellular activities.

Focusing in this work on cortical bone, the answer, according to the here presented calculations, to the aforementioned question must be "no" (or at least "rather not") – the computed fluid velocities were much smaller than the ones used in the mentioned *in vitro* experiments, see Section 5.3 for details. However, it should be stressed that these results do not imply the complete non-relevance of fluid flow in the context of mechanical cell stimulation. Reiterating from Section 5.3, several scenarios are conceivable, leading to canalicular fluid velocities much higher than the ones computed here; such as significant porosity gradients (implying also higher pressure gradients), impact-type loading conditions (causing larger bending moments), or consideration of the vascular pores (where the larger pore dimensions lead to larger fluid velocities) instead of canalicular pores.

As far as future work is concerned, several possibilities for improving the relevance of the conclusions listed above should be mentioned, including

- Explicit consideration of the cell processes in the fluid flow model, as the cell processes may have a non-negligible influence of the fluid flow conditions;

- Basing the computations on the three-dimensional distribution of stress occurring in the bone tissue under physiological loading conditions, in order to thoroughly study the effects of macroscopic stress heterogeneities on the canalicular fluid flow; and
- Conducting *in vitro* fluid flow tests using much lower fluid velocities (i.e. in the range of the here computed ones), in order to observe their effects in terms of cell excitation.

Appendix A.

Nomenclature

Abbreviations

AFM	atomic force microscopy
ATP	adenosine triphosphate
BMU	basic multicellular unit
can	canalicular
CLSM	confocal scanning laser microscopy
COX-2	cyclooxigenase-2
CT	computed tomography
excan	extracanalicular
exlac	extralacunar
exvas	extravascular
FIB	focussed ion beam
FRAP	fluorescence recovery after photobleach
hom	homogenized
lac	lacunar
macro	macroscopic
max	maximum value
mean	mean value
nCT	nano-computed tomography
NO	nitric oxide
OPG	osteoprotegerin
PGE_2	prostaglandin E_2
PTH	parathyroid hormone
RANK	receptor activator of nuclear factor kappa-light-chain-enhancer of activated B cells

RANK L	receptor activator of nuclear factor kappa-light-chain-enhancer of activated B cells ligand
RVE	representative volume element
SEM	scanning electron microscopy
SR	synchrotron radiation
TEM	transmission electron microscopy
TGFβ	transforming growth factor β
vas	vascular
VM	virtual microscopy
Wnt	wingless gene
μCT	micro-computed tomography
μRG	micro-radiography

Latin symbols

A	cross-sectional area
$\mathbf{A}_{\text{can}}$	pressure gradient concentration tensor for canalicular pores
$\mathbf{A}_{\text{excan}}$	pressure gradient concentration tensor for extracanalicular material
$\mathbf{A}^{\text{A}}_{\text{exvas}}$	pressure gradient concentration tensor for extravascular material, considering randomly oriented vascular pores
$\mathbf{A}^{\text{B}}_{\text{exvas}}$	pressure gradient concentration tensor for extravascular material, considering longitudinally oriented vascular pores
$\mathbf{A}_{\text{exlac}}$	pressure gradient concentration tensor for extralacunar material
$\mathbf{A}_{\text{lac}}$	pressure gradient concentration tensor for lacunar pores
$\mathbf{A}^{\text{A}}_{\text{vas}}$	pressure gradient concentration tensor for vascular pores, considering randomly oriented vascular pores
$\mathbf{A}^{\text{B}}_{\text{vas}}$	pressure gradient concentration tensor for vascular pores, considering longitudinally oriented vascular pores
d_{can}	characteristic length of canalicular inclusions
d_{lac}	characteristic length of lacunar inclusions
d_{vas}	characteristic length of vascular inclusions
d_{RVE}	characteristic pore size of RVE
$\mathbf{e}_i$	unit vector in Cartesian base frame $i = 1,2,3$
$\tilde{f}_{\text{can}}$	volume fraction of canalicular pores measured in the extralacunar RVE
$\bar{f}_{\text{can}}$	volume fraction of canalicular pores measured in the extravascular RVE
f_{can}	volume fraction of canalicular pores measured in the macroscopic RVE
$\bar{f}_{\text{lac}}$	volume fraction of lacunar pores measured in the extravascular RVE

f_{lac}	volume fraction of lacunar pores measured in the macroscopic RVE
f_{vas}	volume fraction of vascular pores measured in the macroscopic RVE
g	free-fall acceleration
I_y	moment of inertia with respect to the y-axis
I_z	moment of inertia with respect to the z-axis
$\mathbf{K}$	permeability tensor
$\mathbf{k}_{\mathrm{can}}$	permeability tensor of canalicular pore space
k_{can}	components of the permeability tensor of canalicular pore space
$\mathbf{k}_{\mathrm{lac}}$	permeability tensor of lacunar pore space
k_{lac}	components of the permeability tensor of lacunar pore space
$\mathbf{k}_{\mathrm{vas}}$	permeability tensor of vascular pore space
k_{vas}	components of the permeability tensor of vascular pore space
$\mathbf{K}^{\mathrm{hom}}_{\mathrm{exlac}}$	homogenized permeability tensor of extralacunar material
$K^{\mathrm{hom}}_{\mathrm{exlac}}$	components of the homogenized permeability tensor of extralacunar material
$\mathbf{K}^{\mathrm{hom}}_{\mathrm{exvas}}$	homogenized permeability tensor of extravascular material
$K^{\mathrm{hom}}_{\mathrm{exvas}}$	components of the homogenized permeability tensor of extravascular material
$\mathbf{K}^{\mathrm{hom,\,A}}_{\mathrm{macro}}$	homogenized permeability tensor of macroscopic material, considering randomly organized vascular pores
$K^{\mathrm{hom,\,A}}_{\mathrm{macro}}$	components of the homogenized permeability tensor of macroscopic material, considering randomly organized vascular pores
$\mathbf{K}^{\mathrm{hom,\,B}}_{\mathrm{macro}}$	homogenized permeability tensor of macroscopic material, considering longitudinally oriented vascular pores
$K^{\mathrm{hom,\,B}}_{\mathrm{macro}}$	components of the homogenized permeability tensor of macroscopic material, considering longitudinally oriented vascular pores
ℓ_{RVE}	characteristic length of the RVE
ℓ_{exlac}	characteristic length of the extralacunar RVE
ℓ_{exvas}	characteristic length of the extravascular RVE
ℓ_{macro}	characteristic length of the macroscopic RVE
$\mathscr{L}$	characteristic length of the structure containing the material phases
M	bending moment
N	normal force
$\mathscr{P}$	characteristic length of the loading of the structure containing the material phases
p_{can}	canalicular pore pressure
$p^{\mathrm{A}}_{\mathrm{can}}$	canalicular pore pressure for arbitrarily oriented vascular pores

$p^{\mathrm{B}}_{\mathrm{can}}$	canalicular pore pressure for longitudinally oriented vascular pores
p_{excan}	extracanalicular pore pressure
p_{exlac}	extralacunar pore pressure
p_{exvas}	extravascular pore pressure
p_{lac}	lacunar pore pressure
p_{vas}	vascular pore pressure
p_{macro}	macroscopic pressure
$\mathbf{P}$	inhomogeneity tensor
$\mathbf{P}_{\mathrm{can}}$	inhomogeneity tensor for canalicular pores
$\mathbf{P}_{\mathrm{excan}}$	inhomogeneity tensor for extracanalicular material
$\mathbf{P}_{\mathrm{lac}}$	inhomogeneity tensor for lacunar pores
$\mathbf{P}_{\mathrm{exlac}}$	inhomogeneity tensor for extralacunar material
$\mathbf{P}_{\mathrm{vas}}$	inhomogeneity tensor for vascular pores
$\mathbf{P}_{\mathrm{vas}}$	inhomogeneity tensor for extravascular material
$\mathbf{Q}$	flow vector
$\mathbf{R}$	rotational matrix
R_{can}	canalicular pore pressure
R_{lac}	lacunar radius
R_{vas}	vascular radius
R_{o}	average radius of the femur
R_{i}	average radius of the femoral medullary cavity
$\mathbf{v}_{\mathrm{can}}$	velocity vector in the canalicular pores
v_{can}	component of velocity vector in the canalicular pores
$\mathbf{v}^{\mathrm{A}}_{\mathrm{can}}$	velocity vector in the canalicular pores for arbitrarily oriented vascular pores
$v^{\mathrm{A}}_{\mathrm{can,s}}$	component of velocity vector in the canalicular pores for arbitrarily oriented vascular pores in longitudinal direction of the canaliculus
$\mathbf{v}^{\mathrm{B}}_{\mathrm{can}}$	velocity vector in the canalicular pores for longitudinally oriented vascular pores
$v^{\mathrm{B}}_{\mathrm{can,s}}$	component of velocity vector in the canalicular pores for longitudinally oriented vascular pores in longitudinal direction of the canaliculus
$\mathbf{v}_{\mathrm{exlac}}$	velocity vector in the extralacunar material
v_{exlac}	component of the velocity vector in the extralacunar material
$\mathbf{v}_{\mathrm{exvas}}$	velocity vector in the extravascular material
v_{exvas}	component of the velocity vector in the extravascular material
$\mathbf{x}$	location vector
$\mathbf{1}$	2^{nd} order identity tensor

Greek symbols

α	angular polar coordinate
β	inverse slip coefficient
γ	fluid unit weight
η	dynamic viscosity of fluid
ϑ	Eulerian angle in Euklidean space
κ	intrinsic permeability
λ	slip coefficient
$\boldsymbol{\xi}$	location vector
ξ_i	component of location vector, i=φ,ϑ
φ	Eulerian angle in Euklidean space
ψ	potential function
ρ	fluid density

List of Figures

List of Tables

Bibliography

Abdalrahman, T., Scheiner, S., Hellmich, C. Is trabecular bone permeability governed by molecular ordering–induced fluid viscosity gain? Arguments from re–evaluation of experimental data in the framework of homogenization theory. *J Theor Biol*, 365:433–444, 2015.

Ajubi, N.E., Klein–Nulend, J., Alblas, M.J., Burger, E.H., Nijweide, P.J. Signal transduction pathways involved in fluid flow–induced PGE 2 production by cultured osteocytes. *Am J Physiol Endocrinol Metab*, pages E171–E178, 1999.

Ambekar, R., Chittenden, M., Jasiuk, I., Toussaint Jr, K.C. Quantitative second–harmonic generation microscopy for imaging porcine cortical bone: Comparison to SEM and its potential to investigate age–related changes. *Bone*, 50(3):643–650, 2012.

Ardizzoni, A. Osteocyte lacunar size–lamellar thickness relationships in human secondary osteons. *Bone*, 28(2):215–219, 2001.

Bakker, A.D., Klein–Nulend, J., Burger, E.H. Mechanotransduction in bone cells proceeds via activation of COX–2, but not COX–1. *Biochem Biophys Res Commun*, 305(3):677–683, 2003.

Bakker, A.D., Soejima, K., Klein–Nulend, J., Burger, E.H. The production of nitric oxide and prostaglandin E_2 by primary bone cells is shear stress dependant. *J Biomech*, 34:671–677, 2001.

Bancroft, G.N., Sikavitsas, V.I., van den Dolder, J., Sheffield, T.L., Ambrose, C.G., Jansen, J.A., Mikos, A.G. Fluid flow increases mineralized matrix deposition in 3D perfusion culture of marrow stromal osteoblasts in a dose–dependent manner. *PNAS*, 99(20):12600–12605, 2002.

Bassett, C. Biological significance of piezoelectricity. *Calcif Tissue Res*, 1(4):252–272, 1968.

Beavers, G.S., Joseph, D.D. Boundary conditions at a naturally permeable wall. *J Fluid Mech*, 30:197–207, 1967.

Benalla, M., Palacio–Mancheno, P.E., Fritton, S.P., Cardoso, L., Cowin, S.C. Dynamic permeability of the lacunar–canalicular system in human cortical bone. *Biomech Model Mechanobiol*, 13(4):801–812, 2013.

Beno, T., Yoon, Y.J., Cowin, S.C., Fritton, S.P. Estimation of bone permeability using accurate microstructural measurements. *J Biomech*, 39(13):2378–2387, 2006.

Bilezikian, J.P., Raisz, L.G., Rodan, G.A. Principles of Bone Biology, volume 1. Academic Press, 2 edition, 2002.

Bonewald, L.F. Mechanosensation and transduction in osteocytes. *BoneKEy Osteovision*, 3(10):7–15, 2006.

Bonewald, L.F. The amazing osteocyte. *J Bone Min Res*, 26(2):229–238, 2011.

Bonewald, L.F., Johnson, M.L. Osteocytes, mechanosensing and Wnt signaling. *Bone*, 42(4):606–615, 2008.

Bonewald, L.F., Mundy, G.R.M.D. Role of transforming growth factor–beta in bone remodeling. *Clin Orthop Relat Res*, 250:261–276, 1990.

Bousson, V., Bergot, C., Meunier, A., Barbot, F., Parlier-Cuau, C., Laval-Jeantet, A.M., Laredo, J.D. CT of the middiaphyseal femur: Cortical bone mineral density and relation to porosity. *Radiology*, 217(1), 2000.

Bousson, V., Meunier, A., Bergot, C., Vicaut, E., Rocha, M.A., Morais, M.H., Laval-Jeantet, A.M., Laredo, J.D. Distribution of intracortical porosity in human midfemoral cortex by age and gender. *J Bone Min Res*, 16(7):1308–1317, 2001.

Buckwalter, J.A., Glimcher, M.J., Cooper, R.R., Recker, R. Part I: Structure, blood supply, cells, matrix, and mineralization. *J Bone Joint Surg Am*, 77(8):1256–1275, 1995.

Campbell, G.M., Sophocleous, A. Quantitative analysis of bone and soft tissue by micro–computed tomography: Applications to ex vivo and in vivo studies. *BoneKEy Reports*, 3:1–12, 2014.

Clarke, B. Normal bone anatomy and physiology. *Clinical J Am Soc Nephrol*, 3(Suppl 3):S131–S139, 2008.

Cooper, D., Thomas, C., Clement, J., Turinsky, A., Sensen, C., Hallgrimson, B. Age–dependent change in the 3D structure of cortical porosity at the human femoral midshaft. *Bone*, 40(4):957–965, 2007.

Cooper, D., Turinsky, A., Sensen, C., Hallgrimson, B. Quantitative 3D analysis of the canal network in cortical bone by micro–computed tomography. *Anat Rec Part B New Anat*, 274(1):169–179, 2003.

Cordey, J., Gautier, E. Strain gauges used in the mechanical testing of bones part III: Strain analysis, graphic determination of the neutral axis. *Injury Int J Care Injured*, 30:S–A21–S–A25, 1999.

Darcy, H. Les Fontaines Publiques de la Ville de Dijon [The Public Fountains of the City of Dijon]. Dalmont, Paris, 1856. In French.

Daxner, T., Rammerstorfer, F.G., Böhm, H.J. Adaption der Dichteverteilung in gewichts–effizienten Metallstrukturen [Adaption of density distribution in weight–efficient metal structures]. https://www.ilsb.tuwien.ac.at/ daxner/ictam-projekt/monatsprojekt.html, 2000. Accessed: 2016-12-6, In German.

Dillaman, R.M., Roer, R.D., Gay, D.M. Fluid movement in bone: Theoretical and empirical. *J Biomech*, 24:163–177, 1991.

Dobnig, H., Turner, R.T. Evidence that intermittent treatment with parathyroid hormone increases bone formation in adult rats by activation of bone lining cells. *Endocrinology*, 136(8):3632–3638, 1995.

Dormieux, L., Kondo, D. Approche micromécanique du couplage perméabilité endommagement [Micromechanical approach to the coupling between permeability and damage]. *Comptes Rendus Mécanique*, 332(2):135–140, 2004. In French.

Dormieux, L., Kondo, D. Diffusive transport in disordered media: Application to the determination of the tortuosity and the permeability of cracked materials. In Applied Micromechanics of Porous Materials, volume 480, pages 83–106. Springer, New York, 2005.

Dormieux, L., Kondo, D., Ulm, F.J. Microporomechanics. John Wiley & Sons, Ltd, Chichester, 2006.

Drugan, W., Willis, J. A micromechanics–based nonlocal constitutive equation and estimates of representative volume element size for elastic composites. *J Mech Phys Solids*, 44(4):497–524, 1996.

Duda, G.N., Schneider, E., Chao, E.Y.S. Internal forces and moments in the femur during walking. *J Biomech*, 30(9):933–941, 1997.

Dunlop, J.W.C., Hartmann, M.A., Bréchet, Y.J., Fratzl, P., Weinkamer, R. New suggestions for the mechanical control of bone remodeling. *Calcif Tissue Int*, 85(1):45–54, 2009.

Eberhardsteiner, L., Hellmich, C., Scheiner, S. Layered water in crystal interfaces as source for bone viscoelasticity: Arguments from a multiscale approach. *Comput Methods Biomech Biomed Engin*, 17(1):48–63, 2014.

Eshelby, J. The determination of the elastic field of an ellipsoidal inclusion, and related problems. A(241):376–396, 1957.

Fantner, G.E., Rabinovych, O., Schitter, G., Thurner, P., Kindt, J.H., Finch, M.M., Weaver, J.C., Golde, L.S., Morse, D.E., Lipman, E.A., Rangelow, I.W., Hansma, P.K. Hierarchical interconnections in the nano–composite material bone: Fibrillar cross–links resist fracture on several length scales. *Compos Sci Technol*, 66(9):1205–1211, 2006.

Feik, S.A., Thomas, C.D., Clement, J.G. Age–related changes in cortical porosity of the midshaft of the human femur. *J Anat*, 191:407–416, 1997.

Forner–Cordero, A., Koopman, H.J.F.M., van der Helm, F.C.T. Inverse dynamics calculations during gait with restricted ground reaction force information from pressure insoles. *Gait Posture*, 23(2):189–199, 2006.

Fox, S.W., Chow, J.W.M. Nitric oxide synthase expression in bone cells. *Bone*, 23(1):1–6, 1998.

Frame, B., Parfitt, A.M. Osteomalacia: Current concepts. *Ann Intern Med*, 89:966–982, 1978.

Frangos, J.A., Johnson, D. Fluid flow in bone: Stimulated release at remodeling mediators. *Biorheology*, 2(32):187–187, 1995.

Frangos, J.A., McIntire, L.V., Eskin, S.G. Shear stress induced stimulation of mammalian cell metabolism. *Biotech Bioeng*, 32:1053–1060, 1988.

Fraser, W.D. Hyperparathyroidism. *The Lancet*, 374(9684):145–158, 2009.

Fritsch, A., Hellmich, C. 'Universal' microstructural patterns in cortical and trabecular, extracellular and extravascular bone materials: Micromechanics–based prediction of anisotropic elasticity. *J Theor Biol*, 244(4):597–620, 2007.

Fritsch, A., Hellmich, C., Dormieux, L. Ductile sliding between mineral crystals followed by rupture of collagen crosslinks: Experimentally supported micromechanical explanation of bone strength. *J Theor Biol*, 260(2):230–252, 2009.

Fritton, S.P., Weinbaum, S. Fluid and solute transport in bone: Flow–induced mechanotransduction. *Annu Rev Fluid Mech*, 41(1):347–374, 2009.

Frost, H.M., Thomas, C.C. Bone Remodeling Dynamics. Thomas, Springfield, IL, 1963.

Gailani, G., Benalla, M., Mahamud, R., Cowin, S.C., Cardoso, L. Experimental determination of the permeability in the lacunarcanalicular porosity of bone. *J Biomech Eng*, 131(10):101007, 2009.

Gardinier, J.D., Townend, C.W., Jen, K.P., Wu, Q., Duncan, R.L., Wang, L. In situ permeability measurement of the mammalian lacunar–canalicular system. *Bone*, 46(4):1075–1081, 2010.

Garnett, J.C.M. Colours in metal glasses and in metallic films. *Philos Trans R Soc London*, 203:Ser. B, 1904.

Genetos, D.C., Geist, D.J., Liu, D., Donahue, H.J., Duncan, R.L. Fluid shear–induced ATP secretion mediates prostaglandin release in MC3T3–E1 osteoblasts. *J Bone Miner Res*, 20(1):41–49, 2005.

Gere, J.M., Timoshenko, S.P. Mechanics of Materials. PWS Publishing Company, Boston, 1997.

Goulet, G.C., Hamilton, N., Cooper, D., Coombe, D., Tran, D., Martinuzzi, R., Zernicke, R.F. Influence of vascular porosity on fluid flow and nutrient transport in loaded cortical bone. *J Biomech*, 41(10):2169–2175, 2008.

Gray, H. Anatomy of the Human Body. Lea & Febiger, Philadelphia, 1918.

Gururaja, S., Kim, H.J., Swan, C.C., Brand, R.A., Lakes, R.S. Modeling deformation–induced fluid flow in cortical bone's canalicular–lacunar system. *Ann Biomed Eng*, 33(1):7–25, 2005.

Hagen, G. Über die Bewegung des Wassers in engen cylindrischen Röhren [On the movement of water in narrow cylindrical tubes]. *Poggendorfs Ann Phys Chem*, 1839.

Haut Donahue, T.L., Haut, T.R., Yellowley, C.E., Donahue, H.J., Jacobs, C.R. Mechanosensitivity of bone cells to oscillating fluid flow induced shear stress may be modulated by chemotransport. *J Biomech*, 36(9):1363–1371, 2003.

Hazenberg, J.G., Freeley, M., Foran, E., Thomas, C.L., Taylor, D. Microdamage: A cell transducing mechanism based on ruptured osteocyte processes. *J Biomech*, 39(11):2096–2103, 2006.

Hellmich, C., Barthélémy, J.F., Dormieux, L. Mineral–collagen interactions in elasticity of bone ultrastructure – A continuum micromechanics approach. *Euro J Mech*, A–Solids(23):783–810, 2004.

Hellmich, C., Celundova, D., Ulm, F.J. Multiporoelasticity of hierarchically structured materials: Micromechanical foundations and application to bone. *J Eng Mech*, 135(5):382–394, 2009.

Hellmich, C., Ulm, F.J. Drained and undrained poroelastic properties of healthy and pathological bone: A poro–micromechanical investigation. *Transp Porous Media*, 58(3):243–268, 2005.

Henniker, J. The depth of the surface zone of a liquid. *Rev Mod Phys*, 21:322–341, 1949.

Hesse, B., Langer, M., Varga, P., Pacureanu, A., Dong, P., Schrof, S., Männicke, N., Suhonen, H., Olivier, C., Maurer, P., Kazakia, G.J., Raum, K., Peyrin, F. Alterations of mass density and 3D osteocyte lacunar properties in bisphosphonate–related osteonecrotic human jaw bone, a synchrotron μCT study. *PLoS ONE*, 9(2):1–11, 2014a.

Hesse, B., Männicke, N., Pacureanu, A., Varga, P., Langer, M., Maurer, P., Peyrin, F., Raum, K. Accessing osteocyte lacunar geometrical properties in human jaw bone on the submicron length scale using synchrotron radiation μCT. *J Microsc*, 255(3):158–168, 2014b.

Hesse, B., Varga, P., Langer, M., Pacureanu, A., Schrof, S., Männicke, N., Suhonen, H., Maurer, P., Cloetens, P., Peyrin, F., Raum, K. Canalicular network morphology is the

major determinant of the spatial distribution of mass density in human bone tissue: Evidence by means of synchrotron radiation phase–contrast nano–CT. *J Bone Miner Res*, 30(2):346–356, 2015.

Hill, R. Elastic properties of reinforced solids: Some theoretical principles. *J Mech Phys Solids*, 11(5):357–372, 1963.

Huang, B.W., Chang, C.H., Wang, F.S., Lin, A.D., Tsai, Y.C., Huang, M.Y., Tseng, J.G. Dynamic characteristics of a hollow femur. *Life Sci J*, 9(1):723–726, 2012.

Huang, J.C., Sakata, T., Pfleger, L.L., Bencsik, M., Halloran, B.P., Bikle, D.D., Nissenson, R.A. PTH differentially regulates expression of RANKL and OPG. *J Bone Miner Res*, 19(2):235–244, 2004.

Ichikawa, Y., Kawamura, K., Fujii, N., Nattavut, T. Molecular dynamics and multiscale homogenization analysis of seepage/diffusion problem in bentonite clay. *Int J Numer Methods Eng*, 54(12):1717–1749, 2002.

Ichikawa, Y., Kawamura, K., Nakano, M., Kitayama, K., Fujii, N. Molecular Behavior and Micro/Macro Analysis of Diffusion Problem in Bentonite. In ECCOMAS. Barcelona, Spain, 2000.

Imamura, K., Ozawa, H., Hiraide, T., Takahashi, N., Shibasaki, Y., Fukuhura, T., Suda, T. Continuously applied compressive pressure induces bone resorption by a mechanism involving prostaglandin E2 synthesis. *J Cell Physiol*, 144(2):222–228, 1990.

Jacobs, C.R., Beaupré, G.S., Carter, D.R. Maintenance and Adaptation of Bone Tissue: The Importance of Mechanical Stimuli, Republished from the 1994 Rehabilitation R&D Center Progress Report. https://web.stanford.edu/group/rrd/Publications/mech5.html, 1994. Accessed: 2016-10-30.

Jacobs, C.R., Yellowley, C.E., Davis, B.R., Zhou, Z., Cimbala, J.M., Donahue, H.J. Differential effect of steady versus oscillating flow on bone cells. *J Biomech*, 31:969–976, 1998.

Kaarniranta, K., Elo, M.A., Sironen, R.K., Karjalainen, H.M., Helminen, H.J., Lammi, M.J. Stress responses of mammalian cells to high hydrostatic pressure. *Biorheology*, 40(1–3):87–92, 2003.

Kamel, M.A., Holladay, B.R., Johnson, M.L. Potential interaction of prostaglandin and Wnt signaling pathways mediating bone cell responses to fluid flow. *J Bone Min Res*, 21(Suppl 1):S92, 2006.

Kamel, M.A., Picconi, J.L., Lara–Castillo, N., Johnson, M.L. Activation of β–catenin signaling in MLO–Y4 osteocytic cells versus 2T3 osteoblastic cells by fluid flow shear stress and PGE2: Implications for the study of mechanosensation in bone. *Bone*, 47(5):872–881, 2010.

Kamel–ElSayed, S.A., Tiede–Lewis, L.M., Lu, Y., Veno, P.A., Dallas, S.L. Novel approaches for two and three dimensional multiplexed imaging of osteocytes. *Bone*, 76(C):129–140, 2015.

Kamioka, H., Sugawara, Y., Murshid, S.A., Ishihara, Y., Honjo, T., Takano–Yamamoto, T. Fluid shear stress induces less calcium response in a single primary osteocyte than in a single osteoblast: Implication of different focal adhesion formation. *J Bone Min Res*, 21(7):1012–1021, 2006.

Katz, J., Yoon, H., Lipson, S., Maharidge, R., Meunier, A., Christel, P. The effects of remodelling on the elastic properties of bone. *Calcif Tissue Int*, 36:S31–S36, 1984.

Klein–Nulend, J., Semeins, C.M., Nijweide, P.J., Burger, E.H. Pulsatile fluid flow increases nitric oxide (NO) synthesis by osteocytes but not periosteal fibroblasts — Correlations with prostaglandin upregulation. *Biochem Biophys Res Commun*, pages 640–648, 1995a.

Klein–Nulend, J., Semeins, C.M., Nijweide, P.J., Burger, E.H. Sensitivity of osteocytes to biomechanical stress in vitro. *Fed Am Soc Exp Biol*, 9:441–445, 1995b.

Klein–Nulend, J., Van Der Plas, A., Semeins, C.M., Ajubi, N.E., Frangos, J.A., Nijweide, P.J., Burger, E.H. Sensitivity of osteocytes to biomechanical stress in vitro. *FASEB*, 9(5):441–114, 1995c.

Knothe Tate, M., Knothe, U. An ex vivo model to study transport processes and fluid flow in loaded bone. *J Biomech*, 33(2):247–254, 2000.

Kohlhauser, C., Hellmich, C. Ultrasonic contact pulse transmission for elastic wave velocity and stiffness determination: Influence of specimen geometry and porosity. *Eng Struct*, 47:115–133, 2013.

Kreke, M.R., Huckle, W.R., Goldstein, A.S. Fluid flow stimulates expression of osteopontin and bone sialoprotein by bone marrow stromal cells in a temporally dependent manner. *Bone*, 36(6):1047–1055, 2005.

Kronenberg, H.M. Developmental regulation of the growth plate. *Nature*, 423:332–336, 2003.

Kwon, R., Meays, D., Meilan, A., Jones, J., Miramontes, R., Kardos, N., Yeh, J.C., Frangos, J. Skeletal adaptation to intramedullary pressure–induced interstitial fluid flow is enhanced in mice subjected to targeted osteocyte ablation. *PLoS One*, 7(3):e33336, 2012.

Kwon, R.Y., Frangos, J.A. Quantification of lacunar–canalicular interstitial fluid flow through computational modeling of fluorescence recovery after photobleaching. *Cell Mol Bioeng*, 3(3):296–306, 2010.

LeBlanc, A.D., Spector, E.R., Evans, H.J., Sibonga, J.D. Skeletal responses to space flight and the bed rest analog: A review. *J Musculoskelet Neuronal Interact*, 1:33–47, 2007.

Lemaire, T., Naïli, S., Rémond, A. Study of the influence of fibrous pericellular matrix in the cortical interstitial fluid movement with hydroelectrochemical effects. *J Biomech Eng*, 130(1):011001, 2008.

Lerebours, C., Buenzli, P.R., Scheiner, S., Pivonka, P. A multiscale mechanobiological model of bone remodelling predicts site–specific bone loss in the femur during osteoporosis and mechanical disuse. *Biomech Model Mechanobiol*, 15(1):43–67, 2015a.

Lerebours, C., Thomas, C., Clement, J., Buenzli, P., Pivonka, P. The relationship between porosity and specific surface in human cortical bone is subject specific. *Biomech Model Mechanobiol*, 72:109–117, 2015b.

Li, D., Tang, T., Lu, J., Dai, K. Effects of flow shear stress and mass transport on the construction of a large–scale tissue–engineered bone in a perfusion bioreactor. *Tissue Eng Part A*, 15(10):2773–2783, 2009.

Lin, Y., Xu, S. AFM analysis of the lacunar–canalicular network in demineralized compact bone. *J Microsc*, 241(3):291–302, 2011.

Liu, C., Zhao, Y., Cheung, W.Y., Gandhi, R., Wang, L., You, L. Effects of cyclic hydraulic pressure on osteocytes. *Bone*, 46(5):1449–1456, 2010.

Liu, S., Zuo, J., Li, Z., Yang, Y., Liu, T., Xiao, J., Gao, Z. Study of three–dimensional morphology of the proximal femur in developmental adult dysplasia of the hip suggests that the on–shelf modular prosthesis may not be an ideal choice for patients with Crowe type IV hips. *Int Orthop*, 41:1–7, 2017.

Lu, X.L., Huo, B., Chiang, V., Guo, X.E. Osteocytic network is more responsive in calcium signaling than osteoblastic network under fluid flow. *J Bone Min Res*, 27(3):563–574, 2012.

Mack, P.B., Lachance, P.L. Effects of recumbency and space flight on bone density. *Am J Clin Nutr*, 20(11):1194–1205, 1967.

Malachanne, E., Dureisseix, D., Cañadas, P., Jourdan, F. Experimental and numerical identification of cortical bone permeability. *J Biomech*, 41:721–725, 2008.

Mang, H., Hofstetter, G. Festigkeitslehre. Springer, New York, 2004.

Marie, P.J. Osteoblasts and Bone Formation. In Molecular and Cellular Biology of Bone, volume 5 of *Advances in Organ Biology*, pages 445 – 473. Elsevier, 1998.

Markov, M., Kazatchenko, E., Mousatov, A., Pervago, E. Permeability of the fluid–filled inclusions in porous media. *Transp Porous Media*, 84(2):307–317, 2009.

Marotti, G. The original contributions of the scanning electron microscope to the knowledge of bone structure. Kluwer Academic, Boston, 1990.

Martin, R., Burr, D.B., Sharkey, N.A. Skeletal Tissue Mechanics. Springer, New York, 1998.

Miller, S.C., de Saint–Georges, L., Bowman, B.M., Jee, W.S. Bone lining cells: Structure and function. *Scanning Microsc*, 3(3):952–960, 1989.

Mori, T., Tanaka, K. Average stress in matrix and average elastic energy of materials with misfitting inclusions. *Acta Metall*, 21:571–574, 1973.

Morin, C., Hellmich, C. A multiscale poromicromechanical approach to wave propagation and attenuation in bone. *Ultrasonics*, 54(5):1251–1269, 2014.

Nagatomi, J., Arulanandam, B., Metzger, D., Meunier, A., Bizios, R. Effects of cyclic pressure on bone marrow cell cultures. *J Biomech Eng*, 124:308–314, 2002.

Nagatomi, J., Arulanandam, B.P., Metzger, D.W., Meunier, A., Bizios, R. Frequency–and duration–dependent effects of cyclic pressure on select bone cell functions. *Tissue Eng*, 7(6):717–728, 2001.

Nagatomi, J., Arulanandam, B.P., Metzger, D.W., Meunier, A., Bizios, R. Cyclic pressure affects osteoblast functions pertinent to osteogenesis. *Ann Biomed Eng*, 31:917–923, 2003.

Nicolella, D.P., Bonewald, L.F., Moravits, D.E., Lankford, J. Measurement of microstructural strain in cortical bone. *Eur J Morphol*, 42(1–2):23–9, 2005.

Nollert, M.U., Eskin, S.G., Mclntire, L.V. Shear stress increases inositol triphosphate levels in human endothelial cells. *Biochem Biophys Res Commun*, 170(1):281–287, 1990.

Padilla, F., Jenson, F., Bousson, V., Peyrin, F., Laugier, P. Relationships of trabecular bone structure with quantitative ultrasound parameters: In vitro study on human proximal femur using transmission and backscatter measurements. *Bone*, 42(6):1193–1202, 2008.

Palacio–Mancheno, P.E., Larriera, A.I., Doty, S.B., Cardoso, L., Fritton, S.P. 3D assessment of cortical bone porosity and tissue mineral density using high–resolution μCT: Effects of resolution and threshold method. *J Bone Miner Res*, 29(1):142–150, 2014.

Parfitt, A.M. The actions of parathyroid hormone on bone: Relation to bone remodeling and turnover, calcium homeostasis, and metabolic bone disease. *Metabolism*, 25(10):1157–1188, 1976.

Parfitt, A.M., Travers, R., Rauch, F., Glorieux, F.H. Structural and cellular changes during bone growth in healthy children. *Bone*, 27(4):487–494, 2000.

Pienkowski, D., Pollack, S.R. The origin of stress–generated potentials in fluid–saturated bone. *J Orthop Res*, 1:30–41, 1983.

Pilbeam, C.C., Choudhary, S., Blackwell, K., Raisz, L.G. Prostaglandins and Bone Metabolism. In Principles of Bone Biology, pages 1235–1271. Academic Press, 2008.

Pivonka, P., Hellmich, C., Smith, D. Microscopic effects on chloride diffusivity of cement pastes — A scale–transition analysis. *Cem Concr Res*, 34(12):2251–2260, 2004.

Poiseuille, J. Recherches expérimentales sur le mouvement des liquides dans les tubes de très petits diametrès [Experimental research on the movement of liquids in tubes of very small diameters]. *Mem Acad Sci Inst France*, pages 433–544, 1847. In French.

Pollack, G. The Fourth Phase of Water Beyond Solid, Liquid, and Vapor. Ebner and Sons, Seattle, 2013.

Price, C., Zhou, X., Wen, L., Wang, L. Real–time measurement of solute transport within the lacunar–canalicular system of mechanically loaded bone: Direct evidence for load–induced fluid flow. *J Bone Min Res*, 26(2):277–285, 2011.

Raisz, L. Pathogenesis of osteoporosis: Concepts, conflicts, and prospects. *J Clin Invest*, 115(12):3318–3325, 2005.

Renders, G.A.P., Mulder, L., van Ruijven, L.J., van Eijden, T.M.G.J. Porosity of human mandibular condylar bone. *J Anat*, 210(3):239–248, 2007.

Riddle, R.C., Donahue, H.J. From streaming–potentials to shear stress: 25 years of bone cell mechanotransduction. *J Orthop Res*, 27(2):143–149, 2009.

Robling, A., Castillo, A.B., Turner, C. Biomechanical and molecular regulation of bone remodeling. *Annu Rev Biomed Eng*, 8:455–498, 2006.

Roodman, G.D., Windle, J.J. Paget disease of bone. *J Clin Invest*, 115(2):200–208, 2005.

Rouhana, S.W., Johnson, M.W., Chakkalakal, D.R., Harper, R.A., Katz, J.L. Permeability of compact bone. *Joint ASME-ASCE Conf Biomechanics Symp*, ASME Vol–AMD 43:169–172, 1981.

Saffman, P.G. On the boundary condition at the surface of a porous media. *Stud Appl Math*, 50:93–101, 1971.

Sahraoui, M., Kaviany, M. Slip and no-slip velocity boundary conditions at interface of porous, plain media. *Int J Heat Mass Transfer*, 35(4):927–943, 1991.

Scheiner, S., Pivonka, P., Hellmich, C. Poromicromechanics reveals that physiological bone strains induce osteocyte–stimulating lacunar pressure. *Biomech Model Mechanobiol*, 15(1):9–28, 2015.

Schneider, P., Krucker, Tand Meyer, E., Ulmann–Schuler, A., Weber, B., Stampanoni, M., Müller, R. Simultaneous 3D visualization and quantification of murine bone and bone

vasculature using micro–computed tomography and vascular replica. *Micros Res Tech*, 72(9):690–701, 2009.

Schneider, P., Meier, M., Wepf, R., Müller, R. Serial FIB/SEM imaging for quantitative 3D assessment of the osteocyte lacuno–canalicular network. *Bone*, 49(2):304–311, 2011.

Schneider, P., Stauber, M., Voide, R., Stampanoni, M., Donahue, L.R., Müller, R. Ultrastructural properties in cortical bone vary greatly in two inbred strains of mice as assessed by synchrotron light based micro– and nano–CT. *J Bone Miner Res*, 22(10):1557–1570, 2007.

Sharma, D., Ciani, C., Marin, P.A.R., Levy, J.D., Doty, S.B., Fritton, S.P. Alterations in the osteocyte lacunar–canalicular microenvironment due to estrogen deficiency. *Bone*, 51(3):488–497, 2012.

Sinlapabodin, S., Amornsudthiwat, P., Damrongsakkul, S., Kanokpanont, S. An axial distribution of seeding, proliferation, and osteogenic differentiation of MC3T3–E1 cells and rat bone marrow–derived mesenchymal stem cells across a 3D Thai silk fibroin/gelatin/hydroxyapatite scaffold in a perfusion bioreactor. *Mater Sci Eng C*, 58:960–970, 2016.

Smalt, R., Mitchell, F.T., Howard, R.L., Chambers, T.J. Induction of NO and prostaglandin E_2 in osteoblasts by wall–shear stress but not mechanical strain. *Am J Physiol*, 273(4 Pt 1):E751–758, 1997.

Smit, T.H., Huyghe, J.M., Cowin, S.C. Estimation of the poroelastic parameters of cortical bone. *J Biomech*, 35(6):829–835, 2002.

Smith, S., Wastney, M.E., O'Brien, K.O., Morukov, B.V., Larina, I.M., Abrams, S.A., Davis-Street, J.E., Oganov, V., Shackelford, L.C. Bone markers, calcium metabolism, and calcium kinetics during extended–duration space flight on the Mir space station. *J Bone Miner Res*, 20:208–218, 2005.

Stein, M.S., Feik, S.A., Thomas, C.D., Clement, J.G., Wark, J.D. An automated analysis of intracortical porosity in human femoral bone across age. *J Bone Min Res*, 14(4):624–632, 1999.

Suda, K., Udagawa, N., Sato, N., Takami, M., Itoh, K., Woo, J.T., Takahashi, N., Nagai, K. Suppression of osteoprotegerin expression by prostaglandin E_2 is crucially involved

in lipopolysaccharide–induced osteoclast formation. *J Immunol*, 172(4):2504–2510, 2004.

Sugawara, Y., Ando, R., Kamioka, H., Ishihara, Y., Honjo, T., Kawanabe, N., Kurosaka, H., Takano–Yamamoto, T., Yamashiro, T. The three–dimensional morphometry and cell–cell communication of the osteocyte network in chick and mouse embryonic calvaria. *Calcif Tissue Int*, 88(5):25–37, 2011.

Sugawara, Y., Kamioka, H., Honjo, T., Tezuka, K., Takano–Yamamoto, T. Three-dimensional reconstruction of chick calvarial osteocytes and their cell processes using confocal microscopy. *Bone*, 36(5):77–883, 2005.

Sutera, S., Skalak, R. The history of Poiseuille's law. *Annu Rev Fluid Mech*, 25:1–19, 1993.

Tai, K., Pelled, G., Sheyn, D., Bershteyn, A., Han, L., Kallai, I., Zilberman, Y., Ortiz, C., Gazit, D. Nanobiomechanics of repair bone regenerated by genetically modified mesenchymal stem cells. *Tissue Eng Part A*, 14(10):1709–1720, 2008.

Takahashi, N., Akatsu, T., Udagawa, N., Sasaki, T., Yamaguchi, A. Osteoblastic cells are involved in osteoclast formation. *Endocrinology*, 123(5):2600–2, 1988.

Tan, S.D., de Vries, T.J., Kuijpers–Jagtman, A.M., Semeins, C.M., Everts, V., Klein–Nulend, J. Osteocytes subjected to fluid flow inhibit osteoclast formation and bone resorption. *Bone*, 41(5):745–751, 2007.

Thi, M.M., Suadicani, S.O., Schaffler, M.B., Weinbaum, S., Spray, D.C. Mechanosensory responses of osteocytes to physiological forces occur along processes and not cell body and require $\alpha_v\beta_3$ integrin. *PNAS*, 110(52):21012–21017, 2013.

Timoshenko, S.P. History of Strength of Materials. McGraw–Hill, New York, 1953.

Tommasini, S.M., Trinward, A., Acerbo, A.S., De Carlo, F., Miller, L.M., Judex, S. Changes in intracortical microporosities induced by pharmaceutical treatment of osteoporosis as detected by high resolution micro–CT. *Bone*, 50(3):596–604, 2012.

Turner, C.H., Owan, I., Jacob, D.S., McClintock, R., Peakock, M. Effects of nitric oxide synthase inhibitors on bone formation in rats. *Bone*, 21(6):487–490, 1997.

Vatsa, A., Breuls, R.G., Semeins, C.M., Salmon, P.L., Smit, T.H., Klein–Nulend, J. Osteocyte morphology in fibula and calvaria – Is there a role for mechanosensing? *Bone*, 43(3):452–458, 2008.

Vaughan, T.J., Mullen, C.A., Verbruggen, S.W., McNamara, L.M. Bone cell mechanosensation of fluid flow stimulation: A fluid–structure interaction model characterising the role integrin attachments and primary cilia. *Biomech Model Mechanobiol*, 14(4):703–718, 2014.

Wan, M., Shi, X., Feng, X., Cao, X. Transcriptional mechanisms of bone morphogenetic protein–induced osteoprotegrin gene expression. *J Biol Chem*, 276(13):10119–10125, 2001.

Wang, L., Wang, Y., Han, Y., Henderson, S., Majeska, R., Weinbaum, S., Schaffler, M. In situ measurement of solute transport in the bone lacunar–canalicular system. *PNAS*, 102(33):11911–11916, 2005.

Weinbaum, S., Cowin, S.C., Zeng, Y. A model for the excitation of osteocytes by mechanical loading–induced bone fluid shear stresses. *J Biomech*, 27(3):339–360, 1994.

Weiner, S., Wagner, H.D. The material bone: Structure–mechanical function relations. *Annu Rev Mater Sci*, 28:271–298, 1998.

You, J., Yellowley, C.E., Donahue, H.J., Zhang, Y., Chen, Q., Jacobs, C.R. Substrate deformation levels associated with routine physical activity are less stimulatory to bone cells relative to loading–induced oscillatory fluid flow. *J Biomech Eng*, 122:387–393, 2000.

You, L.D., Weinbaum, S., Cowin, S.C., Schaffler, M.B. Ultrastructure of the osteocyte process and its pericellular matrix. *Anat Rec A Discov Mol Cell Evol Biol*, 278(2):505–513, 2004.

Zaoui, A. Continuum micromechanics: Survey. *J Eng Mech*, 128(8):808–816, 2002.

Zhang, D., Weinbaum, S., Cowin, S.C. Estimates of the peak pressures in bone pore water. *J Biomech Eng*, 120(6):697–703, 1998.

Zhou, X., Novotny, J.E., Wang, L. Modeling fluorescence recovery after photobleaching in loaded bone: Potential applications in measuring fluid and solute transport in the osteocytic lacunar–canalicular system. *Ann Biomed Eng*, 36(12):1961–1977, 2008.